BOSTON UNIVERSITY

GRADUATE SCHOOL OF ARTS AND SCIENCES

Dissertation

A NEW PRECISION MEASUREMENT OF THE ANOMALOUS MAGNETIC MOMENT OF THE POSITIVE MUON

by

ALEXEI VITALYEVICH TROFIMOV

Diploma, Moscow State University, 1995

Submitted in partial fulfillment of the

requirements for the degree of

Doctor of Philosophy

2002

Approved by

First Reader ____________________________________

James P. Miller, Ph.D.
Professor of Physics

Second Reader ____________________________________

B. Lee Roberts, Ph.D.
Professor of Physics

Acknowledgments

I wish to dedicate this work to the memory of my mother, Anna Trofimova, M.D., whose professionalism and strive for knowledge have always been a great example and inspiration to me, and whose love, support and encouragement were invaluable.

I am very grateful to everybody in the (g-2) collaboration whose expertise, hard work and extraordinary motivation made this result possible. Special thanks go to my dissertation advisor, James P. Miller, and the second reader, B. Lee Roberts, for their help, leadership and insightful comments on this dissertation. I would also like to acknowledge the other members of the (g-2) team at Boston University, who helped me out in numerous ways: Rob Carey, Matt Hare and Jon Paley. I would like to express my gratitude to the many physicists who provided me with advice and guidance during the experimental runs and collaboration meetings at Brookhaven: Dave Hertzog, Bill Morse, Yuri Orlov, Jörg Pretz, Ofer Rind, Yannis Semertzidis, to name just a few. Thanks and thumbs-up to my fellow "analyzers", who worked their magic on the data from the 1999 run: Huaizhang Deng, Long Duong, Fred Gray, Ivan Logashenko, Ralf Prigl, Gerco Onderwater, and Cenap Özben.

I would like to thank everybody at the Physics Department for making my years at BU very rewarding. I am particularly indebted to the members of my dissertation committee, Profs. Ulrich Heintz, Claudio Rebbi and Sidney Redner.

Thanks are due to all of my instructors at my undergraduate alma mater, Moscow State University, and the Institute for High Energy Physics at Protvino, Russia, where I performed my bachelor's thesis work under the supervision of Sergei P. Denisov and Alexander Kozelov.

My special love goes to my father, Vitaly Trofimov, and my brother, Dmitry.

My love and thanks to all of my friends in Boston and elsewhere, too many to list, who helped sustain me through the graduate school. You know who you are and I very much appreciate your friendship, support and awesome company.

Words cannot express my gratitude to my partner, Rob Garrison, for love, support and exceptional patience.

Last but not least, good luck Mr. Gorsky.

The experiment E821 at Brookhaven was supported in part by the U.S. Department of Energy, the U.S. National Science Foundation, the German Bundesminister für Bildung und Forschung, the Russian Ministry of Science, and the US-Japan Agreement in High Energy Physics.

A NEW PRECISION MEASUREMENT OF THE ANOMALOUS MAGNETIC MOMENT OF THE POSITIVE MUON

(Order No.)

ALEXEI VITALYEVICH TROFIMOV

Boston University Graduate School of Arts and Sciences, 2002
Major Professor: James P. Miller, Professor of Physics

ABSTRACT

This dissertation presents the analysis and results of the measurement of the anomalous magnetic moment of the positive muon (a_μ). The experiment was conducted at the the Alternating Gradient Synchrotron at Brookhaven National Laboratory (BNL). Polarized muons were stored in a uniform magnetic field, and a_μ was determined by measuring the free proton nuclear magnetic resonance frequency (ω_p) in that magnetic field, and the difference between the muon spin precession and cyclotron frequencies (ω_a).

The experiment began taking data in 1997. A detailed analysis of the frequency ω_a, using a multi-parameter fit is presented, based on the data set from the third experimental run (1999). The new experimental result has a precision of 1.35 parts per million (ppm): $a_\mu^{exp}(\mathrm{BNL}, 1999) = 11\,659\,202(16) \times 10^{-10}$. It agrees well with previous measurements. The weighted mean of all measurements to date shows a difference of 2.6 standard deviations from the Standard Model (SM) prediction (a_μ^{SM}):

$$a_\mu^{exp} - a_\mu^{SM} = (43 \pm 16) \times 10^{-10}.$$

This difference may suggest the presence of physics beyond the Standard Model.

Contents

Acknowledgments **iii**

Abstract **iv**

Table of Contents **v**

List of Figures **viii**

List of Tables **xiii**

List of Acronyms **xiv**

1 Introduction **1**
1.1 Definition of g and a 2
1.2 The Theory of $(g-2)$ 2
1.2.1 The Standard Model Prediction for a_e 2
1.2.2 The Standard Model Prediction for a_μ 4
1.2.3 a_μ and "New Physics" 7

2 Muon $(g-2)$ Measurements at CERN **10**
2.1 First CERN Experiment (1958-1961) 11
2.2 Second CERN Experiment (1962-1968) 13
2.3 Third CERN Experiment (1969-1976) 15

3 Experiment E821 at BNL **21**
3.1 Alternating Gradient Synchrotron 21
3.2 Beamlines 21
3.3 Superconducting Inflector 23
3.4 Muon Storage Ring 24
3.4.1 Magnetic Field Measurement 25
3.4.2 Vacuum Chamber 25
3.4.3 Electrostatic Quadrupoles 25
3.5 Muon Kicker 26

3.6 Scintillating Fiber Monitors 27
3.7 Electron Detectors 28
3.7.1 Electromagnetic Calorimeters 28
3.7.2 Front Scintillator Detector (FSD) 29
3.7.3 Position Sensitive Detector (PSD) 29
3.8 Detector Electronics and the Data Acquisition System 29
3.9 Data Production 30

4 First Results from the $(g-2)$ Experiment at BNL **33**
4.1 First Experimental Run, 1997 33
4.2 Second Experimental Run, 1998 35
4.3 Third Experimental Run, 1999 38

5 Analysis of the 1999 Data **40**
5.1 Data Selection for the Analysis of ω_a 40
5.1.1 Cuts on Data Quality 41
5.1.2 Detector Energy Calibration 42
5.1.3 Correction for Energy Scale Changes 43
5.1.4 Data Histograms 48
5.2 Modifications in the Fitting Function 50
5.2.1 Pile-up 51
5.2.2 Coherent Betatron Oscillation 56
5.2.3 Muon Losses 57
5.3 Fitting Procedure 59
5.4 Fit Results 61
5.4.1 Quality of Fit and Statistical Consistency 61
5.4.2 Comparison of the Results of 4 Analyses 70
5.4.3 Corrections to ω_a 70
5.5 Magnetic Field Analysis 72

6 Systematic Uncertainties for the 1999 Analysis **75**
6.1 Errors Due to Pile-up 75
6.1.1 Pile-up Phase 75
6.1.2 Low-energy Pile-up 76
6.2 AGS Background 77
6.3 Errors Due to Changes in the Energy Scale 79
6.4 Randomization and Binning Errors 81
6.5 Errors Due to Fitting Method and Strategy 82
6.5.1 Fit Function Inefficiencies 82
6.5.2 Fixing Fit Parameters 83
6.6 Other Errors 84
6.7 Systematics of the ω_p Measurement 85

7 Conclusions **87**

List of Abbreviations **89**

Bibliography **90**

List of Figures

1.1 The Feynman graphs for (a) $g = 2$, (b) lowest order radiative correction (Schwinger term), and (c) vacuum polarization with an electron-positron loop. 3
1.2 The Feynman graphs of (a) the lowest order hadronic correction (hadronic vacuum polarization), and the hadroproduction processes used in its evaluation: (b) electron-positron annihilation, and (c) hadronic τ-decay. 5
1.3 The Feynman graphs of some higher-order hadronic corrections to a_μ. 6
1.4 The hadronic light-on-light scattering. 7
1.5 The single-loop electroweak contributions to a_μ. 7
1.6 The lowest order supersymmetric contributions to $(g-2)_\mu$. 8

2.1 CERN-I experiment: the general view of the experimental apparatus (shown not to scale). 11
2.2 CERN-I experiment: electron asymmetry plotted vs storage time t, together with the fitting function $A(t) = A_0 \sin(a_\mu \frac{e}{mc} \langle B \rangle t + \theta_0)$ [29]. . 13
2.3 CERN-II experiment: the apparatus. 14
2.4 CERN-II experiment: distribution of decay electrons vs time. A) from 20 to 45 μs, B) from 65 to 90 μs, C) from 105 to 130 μs. The lower curve shows the rotation frequency of the muon as seen at early time [31]. 16
2.5 CERN-III experiment: the apparatus. 17
2.6 CERN-III experiment: (a) electron count rate at early time shows the bunched structure ("fast rotation"); (b) radial distribution of stored muons calculated from the beam debunching rate [12]. 18
2.7 CERN-III experiment: the time spectrum of decay electrons [12]. . . 19

3.1 Scheme of the $(g-2)$ beamlines. 22
3.2 Superconducting inflector. 23
3.3 The cross-section of the main magnet. 24
3.4 A cross-section of the vacuum chamber with electrostatic quadrupole. 26
3.5 A schematic view of the $(g-2)$ storage ring. 27
3.6 Scintillating fiber monitor. 28
3.7 `G2Off` pulse-finding algorithm [50]. 31

4.1 A sample of the 1997 data with 8-parameter fit function overlayed. The χ^2/DOF was 1.028 for 803 degrees of freedom [53]. 34
4.2 1998 run: positron time spectra from all detectors added together ($E >$ 1.8 GeV) [55]. 36
4.3 1998 run: the equilibrium radius distribution calculated using the tracking code (histogram) and obtained from the analysis of the beam debunching (filled circles) [55]. 37
4.4 1998 run: a magnetic field profile averaged over azimuth. The circle encloses the muon storage region of 4.5 cm radius. The contours represent 2 ppm changes in the field [55]. 38

5.1 The number of spills eliminated due to (a) tØ pulse and (b) quadrupole trace quality problems vs the run number. 41
5.2 The positron pulse energy distribution for detector 23 in run 4669, for the time after 100 μs following the injection (the hardware threshold for the pulses was 50 WFD counts). A straight line fit to the linear part of the slope brings the energy end-point value of 175 WFD counts. 42
5.3 (a) The end-point values for detector 1 are shown with fit errors vs run number: a 2% change in the energy calibration was observed beginning with run 4025. The distribution of end-points has a gaussian form for two groups of runs: (b) before and (c) after the recalibration occurred. 44
5.4 Normalized average energy of the positron pulses recorded by detector 1 shown as a function of time after the injection for different energy cuts. Averaging was done over the anomalous precession period and the result was then normalized to the late time (after 200 μs) average. 46
5.5 The distribution of the values $\mathcal{B}(E_1, E_2)$ (See Eqn. 5.4) for different combinations of the energy cuts, with fit to a gaussian function: (a) for the cuts $0.6 \cdot E_{max}$ and $0.7 \cdot E_{max}$, (b) for the cuts $0.6 \cdot E_{max}$ and $0.8 \cdot E_{max}$, and (c) for the cuts $0.6 \cdot E_{max}$ and $0.9 \cdot E_{max}$ 47
5.6 Energy scale change vs time for detector 1: the results obtained using 3 different combinations of energy cuts are in good agreement. 47
5.7 Relative energy scale change shown as a function of time after the injection for detectors (a) 1, (b) 4, (c) 5, (d) 8, (e) 12 and (f) 24. The data for each detector is overlayed with fit to the function given by Eqn. 5.6. 49
5.8 Time distribution of decay positrons (number of decays per cyclotron period) for the energy cut 2 GeV. The muon lifetime in the laboratory is close to 64.4 μs due to time dilation. The events from the time range 32-600 μs after the injection were used in the analysis. 50
5.9 Pile-up construction. 52
5.10 Time spectrum of constructed pile-up, overlayed with fit function given by Eqn. 5.10. 52

5.11 Constructed pile-up: (a) energy distribution of the "positive" and "negative" pile-up events; (b) net change in the number of registered pulses due to pile-up vs pulse energy; (c) energy distributions of all pulses and constructed pile-up pulses compared. 53
5.12 (a) Average energy for detector 24 vs time, corrected for ESC and normalized to the late time average, with fit to the function given by Eqns. 5.13, 5.14 overlayed; fit results for the parameters of pile-up enhancement due to fast rotation: (b) a_p and (c) τ_p for different detectors are in good agreement. 55
5.13 a) Coherent betatron oscillations were observed in the residuals of the 5-parameter fit; b) Fourier analysis of the residuals of the 5-parameter fit shows a large peak corresponding to coherent betatron oscillation frequency; two smaller peaks on each side come from the beating of the CBO and $(g-2)$ frequencies. 56
5.14 Number of FSD three-fold coincidences as a function of time [66]. . . 58
5.15 The ratio of the positron decay spectrum to the late-time fit (100-600 μs), shows a significant excess of positron counts at early times after the injection (before 60 μs). 59
5.16 a) The fitted frequency $\omega_a/2\pi$ vs start time of the fit, from fit to the sum of the data from 22 detectors. The shaded area represents a one standard deviation statistical error band. The broken line shows the size of expected one-σ statistical fluctuations with respect to the result at 32 μs (given by Eqn. 5.24). b) Results of the fit to the spectra from individual detectors. The fit region was 32-600 μs, detectors 2 and 20 were not used in the analysis due to hardware problems. 61
5.17 Fit results for the selection of positrons with $E > 2$ GeV: (a) χ^2 per degree of freedom vs fit start time (acceptable one-standard-deviation bands are shown as broken lines). Fit parameters are shown vs function of fit start time: (b) phase of the anomalous precession, ϕ; (c) decay asymmetry, A; (d) dilated muon lifetime, $\tau_0\gamma$; (e) pile-up fraction, n_p; and (f) pile-up asymmetry, A_p. Shaded areas represent one standard deviation statistical error bands. The broken line shows the size of expected one-σ statistical fluctuations with respect to the result at 32 μs (given by Eqn. 5.24, where applicable: since the parameters τ, n_p and A_p are correlated to the muon loss parameter a_μ, which is fixed for the fit start times after 50 μs, Eqn. 5.24 can only be applied to compare the results for the fit start times before 50 μs). 62

5.18 Fit parameters are shown vs fit start time for the selection of positrons with $E > 2$ GeV. Betatron oscillation parameters: (a) frequency, f_b (fixed after 80 μs), (b) amplitude, A_B; (c) phase, ϕ_B; (d) decay time; τ_B (fixed after 50 μs); and muon loss parameters: (e) amplitude, $a_{\mu L}$ (fixed after 50 μs) and (f) decay time, $\tau_{\mu L}$ (fixed after 70 μs). The broken line shows the size of expected one-σ statistical fluctuations with respect to the result at 32 μs (given by Eqn. 5.24, where applicable). 63
5.19 Results for the data from 22 detectors fit separately from 32 to 600 μs. Fit parameters vs detector number: (a) χ^2 per degree of freedom; (b) decay asymmetry, A; (c) dilated muon lifetime, $\tau_0\gamma$; (d) phase of the anomalous precession, ϕ; (e) pile-up fraction, n_p, and (f) asymmetry, A_p. The corresponding results for the sum of the data are shown for comparison as broken lines. 64
5.20 Results for the data from 22 detectors fit separately from 32 to 600 μs. Betatron oscillation parameters vs detector number: (a) frequency, f_b; (b) amplitude, A_B; (c) phase, ϕ_B; (d) decay time, τ_B. The corresponding results for the sum of the data are shown for comparison as broken lines. 65
5.21 Additional fit parameters were weakly correlated with ω_a and served to eliminate the phase pulling and improve the fit χ^2: (a) fitted values of ω_a are compared for the 5- and 13-parameter functions; statistical error bands are shown for the 13-parameter fit result. (b) Fast Fourier transform of the data and fit residuals of the 5- and 13-parameter functions. 66
5.22 Consistency checks: (a) the values of ω_a from fit to 12 subsets of the data taken during different periods of the 1999; (b) the results from fit to data with different energy cuts (with the statistical error bands shown for the cut $E > 2$ GeV). 69
5.23 The distribution of $\mathcal{D}_{\omega_a}$, given by Eqn. 5.25, has the gaussian form with the RMS of 1. 70
5.24 The magnetic field measured with the trolley center probe vs azimuth for one of the trolley measurements. The dip at 350° is due to the inflector fringe field [80]. 72
5.25 A 2-dimensional multipole expansion of the field averaged over azimuth from one of the trolley measurements. One ppm contours are shown with respect to a central average field $B_0 = 1.451\ 266$ T. The circle indicates the muon beam storage region [1]. 73
5.26 The B field averaged over 10 minutes vs time in days. The data-taking took place between days 15 and 40 [80]. 73

6.1 Zero-crossings of the decay positron data: the data are shown as empty circles, overlayed with fit to an exponential function; zero-crossings are shown as filled circles. 76
6.2 Change in the fitted value of R caused by changing the difference between the g-2 and pile-up phases (fixed parameter $\Delta\phi_p$), for the data selection with the energy cut of 2 GeV, fit from 32 and 600 μs. The values of R are shown with statistical errors from fit. 77
6.3 Flashlet peaks in the fast Fourier transform spectrum of the 13-parameter fit residuals (data from detector 4) are seen at (a) the AGS frequency, $f_{AGS} \simeq 371$ kHz; and (b) $f = 6 \cdot f_{AGS} \simeq 2228$ kHz. 78
6.4 Results of a flashlet simulation ("worst case", flashlets arriving with the AGS frequency of $f = 371$ kHz): (a) flashlet spectrum generated with the AGS frequency (126 ppm contamination level); (b) shift in the fitted value of R due to flashlet contamination as a function of fit start time. 79
6.5 Results of fit to the data from detector 1 are compared: (a) fit χ^2 per degree of freedom vs fit start time, shown before (solid line) and after (dots) the ESC correction was applied; (b) the fit parameter R, (c) decay asymmetry, (d) dilated muon lifetime vs fit start time, before (filled circles) and after (diamonds) the correction, shaded area shows fit errors for the ESC-corrected result. 80
6.6 Phase pulling on the fit parameter R observed in the results of fit to data when (a) the correction for muon losses, or (b) the CBO correction are *not* included in the fitting function at all. Phase pulling due to muon losses is minimized for fits starting at the zero-crossings of the data, shown as filled circles. 82
6.7 Phase pulling on R: (a) due to fixing the parameters τ_B, f_B, $a_{\mu L}$ and $\tau_{\mu L}$ (top: ΔR vs fit start time, bottom: distribution of ΔR); and (b) due to fixing the parameters of the fast rotation correction to pile-up. Crosses denote the zero-crossings of the data. 84

7.1 Five measurements of the muon anomalous magnetic moment shown in comparison with the one-standard-deviation region allowed by the standard theory (shaded area). 88

List of Tables

1.1 Standard Model prediction for a_μ. 8

4.1 Systematic errors for the 1997 a_{μ^+} measurement [53]. 35

5.1 χ^2 per degree of freedom from fit to the sum of data from 22 detectors, for different fit start times and forms of the fitting function. In the fitting function expression: $n(t)$ is the 5-parameter function, $p(t)$ is the pile-up function, $b(t)$ is the correction for betatron oscillations, and $l(t)$ is the muon loss correction, which are described respectively by Eqns. 5.9, 5.10, 5.16 and 5.17. Underlined are the statistically acceptable values of χ^2/DOF (see Eqn. 5.23). 67

5.2 The results of four ω_a analyses. $R = (1 - \omega_a/2\pi f_0) \cdot 10^6$, where $f_0 =$ 229.1 kHz. The errors on R are statistical. The UI result is a weighted mean of results of fit to data from individual detectors, with different fit start times [73]. 71

6.1 Systematic errors for the ω_a analysis [1]. 85

6.2 Systematic errors for the ω_p analysis [1]. 86

List of Acronyms

ADC .... Analog-to-Digital Converter
AGS .... Alternating Gradient Synchrotron
BINP .... Budker Institute for Nuclear Physics
BNL .... Brookhaven National Laboratory
BU .... Boston University
CAMAC .... Computer Automated Measurement and Control
CBO .... Coherent Betatron Oscillation
CERN .... European Organization for Nuclear Research
CPT .... Charge, Parity and Time
DLT .... Digital Linear Tape
DOF .... Degree of Freedom
ESC .... Energy Scale Change
FSD .... Front Sensitive Detector
GeV .... Giga-electron-Volt
IEEE .... Institute of Electrical and Electronics Engineers
LED .... Light-Emitting Diod
MeV .... Mega-electron-Volt
MTDC .... Multi-Hit Time-to-Digital Converter
NMR .... Nuclear Magnetic Resonance
PAW .... Physics Analysis Workstation
PMT .... Photomultiplier Tube
ppb .... parts per billion
ppm .... parts per million
PSD .... Position Sensitive Detector
RMS .... Root Mean Square
QED .... Quantum Electrodynamics
SCSI .... Small Computer System Interface
SM .... Standard Model
SUSY .... Supersymmetry
SWIC .... Segmented Wire Ion Chamber
TDC .... Time-to-Digital Converter
Tp .... Tera-proton

UI .... University of Illinois
UM .... University of Minnesota
UNIX .... Uniplexed Information and Computing System
VME .... Versa Module Europa
WFD .... Wave-Form Digitizer
WWW .... World Wide Web

Chapter 1

Introduction

The anomalous magnetic moment of the muon, a_μ, is of central importance in elementary particle physics. It is one of the few fundamental quantities that can be measured with high precision, and, at the same time, calculated from first principles.

The goal of the experiment 821 (E821) at Brookhaven National Laboratory (BNL), is to measure a_μ with a relative precision of 0.35 parts per million (ppm). This will provide a stringent test of the Standard Model of particle physics, as well as put constraints on new speculative theories. In this way, a precise measurement of the muon magnetic anomaly is complementary to the direct search for new particles at high-energy colliders.

The experiment at Brookhaven started taking data in 1997. This dissertation presents the analysis of the data, taken during the third experimental run, in 1999, focusing on the analysis of the muon spin precession frequency. Based on this data set, a precision of 1.35 ppm in a_μ was achieved, with the uncertainty being predominantly statistical [1].

The techniques developed for the analysis of the 1999 data, and various systematic studies conducted in the process, prove extremely useful in the ongoing work on the data sets collected during the subsequent runs of E821, in 2000 and 2001.

In the introduction, the theory of the anomalous magnetic moment of the muon and the motivation for the experiment are discussed.

The principle of the measurement, and the overview of past experiments conducted at the European Organization for Nuclear Research (CERN) laboratory between 1958 and 1976, are given in Chapter 2.

The experimental apparatus, used in the ongoing experiment at BNL is described in Chapter 3.

Chapter 4 contains a brief history of the first three E821 experimental runs at Brookhaven.

Chapter 5 is dedicated to the discussion of the analysis of the data taken during the 1999 experimental run.

Systematic errors for this analysis are discussed in Chapter 6.

The final chapter summarizes the results and conclusions.

1.1 Definition of g and a

For a charged particle, the gyromagnetic ratio, g, relates the dipole magnetic moment, $\vec{\mu}$, to the spin angular momentum, $\vec{S}$,

$$\vec{\mu} = g\frac{e}{2mc}\vec{S}. \tag{1.1}$$

Dirac's theory predicts a value of $g = 2$ for a point-like particle.

The discovery that, for the electron, $g \neq 2$ [2, 3, 4], and the calculation by Schwinger [5] predicting that (to first order) the radiative correction to g_e was α/π, were important early steps in the development of Quantum Electrodynamics (QED).

The anomalous magnetic moment describes the relative deviation of the muon gyromagnetic ratio from the value 2:

$$a \equiv \frac{g-2}{2} \tag{1.2}$$

For the obvious reason, the anomalous magnetic moment of the lepton is often referred to as the "$(g-2)$ value".

1.2 The Theory of $(g-2)$

In the Standard Model (SM), the anomalous magnetic moment of leptons arises from quantum fluctuations. The theoretical expression for the magnetic anomaly of the lepton may be written as:

$$a_l^{SM} = a_l^{QED} + a_l^{Had} + a_l^{Weak}, \tag{1.3}$$

where the dominant term, a_l^{QED}, accounts for the purely quantum electrodynamic contribution to a_l^{SM} (involving only the leptons and photons), a_l^{Had} comes from predominantly hadronic (i.e. involving strong interaction) processes, and a_l^{Weak} describes the effect of predominantly electroweak interactions [6].

The size of each contribution can be calculated with high precision, using standard theory prescriptions and experimental data.

1.2.1 The Standard Model Prediction for a_e

Since the electron, being much less massive than the muon, cannot readily create a virtual muon-antimuon pair, the muons (and heavier particles, in general) have little effect on a_e [7]. Therefore, the electron anomalous magnetic moment is dominated by QED of electrons and photons. The Feynman diagrams of the leading contributions are shown in Figure 1.1.

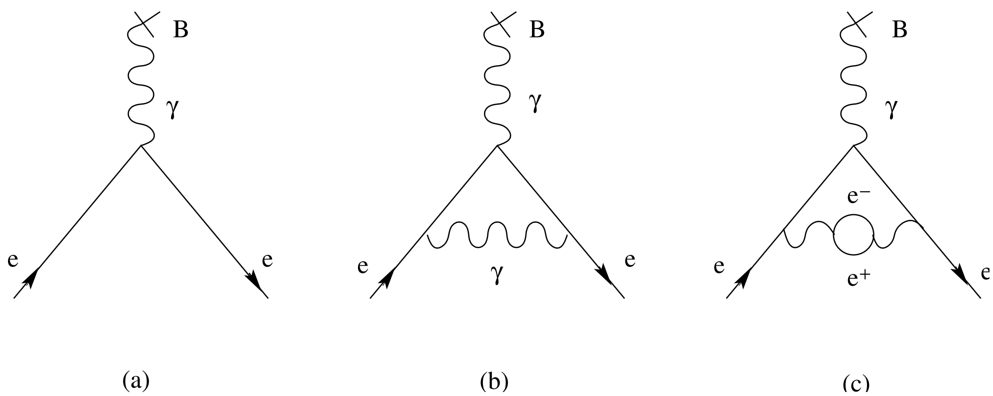

Figure 1.1: The Feynman graphs for (a) $g = 2$, (b) lowest order radiative correction (Schwinger term), and (c) vacuum polarization with an electron-positron loop.

The QED contribution to the electron magnetic anomaly, a_e^{QED}, can be written as an expansion of powers of the fine structure constant, α:

$$a_e^{QED} = C_1(\frac{\alpha}{\pi}) + C_2(\frac{\alpha}{\pi})^2 + C_3(\frac{\alpha}{\pi})^3 + C_4(\frac{\alpha}{\pi})^4 + \ldots, \tag{1.4}$$

where the coefficients $C_1 = 0.5$, $C_2 = -0.328\ 478\ 444$, $C_3 = 1.181\ 234\ 017$ are known analytically, and $C_4 = -1.5098(384)$ is partially calculated numerically by using perturbation theory [6, 8]. The contribution from loops with muons and tauons, entering in the coefficients C_2, C_3 and C_4, accounts for less than 3 parts per billion of the total value of a_e^{QED}.

The small hadronic and electroweak contributions are respectively [6]:

$$a_e^{Had} = 1.631(19) \times 10^{-12}, \tag{1.5}$$
$$a_e^{Weak} = 0.030(1) \times 10^{-12}. \tag{1.6}$$

And the total Standard Model prediction for the electron magnetic anomaly is [9]:

$$a_e^{SM} = a_e^{QED} + a_e^{Had} + a_e^{Weak} = 1\ 159\ 652\ 153.5(24.0) \times 10^{-12}, \tag{1.7}$$

where the error is dominated by the uncertainty in the value of $\alpha = e^2/\hbar c$, determined from a measurement of the Quantum Hall effect [10].

The anomalous magnetic moment value was measured by Dehmelt and collaborators [11] for both the electron and the positron to 3.7 parts per billion:

$$a_{e^-}^{exp} = 1\ 159\ 652\ 188.4(4.3) \times 10^{-12}, \tag{1.8}$$
$$a_{e^+}^{exp} = 1\ 159\ 652\ 187.9(4.3) \times 10^{-12}. \tag{1.9}$$

This is one of the most precise measurements in physics. The impressive agreement between the theory and the experiment (at the level of $1.5{\cdot}\sigma$) represents a triumph for QED. This result also verifies CPT-invariance at the 2×10^{-12} level, which is the most accurate demonstration of *charged* particle-antiparticle symmetry to date[1] [11].

The best current value of α [10] was obtained by equating the theoretical prediction for a_e and the average of the experimental measurements given by Eqns. 1.8 and 1.9:

$$\alpha^{-1} = 137.035\ 999\ 58(52)\ (3.2\ \text{ppm}) \tag{1.10}$$

1.2.2 The Standard Model Prediction for a_μ

Since the relative contribution of heavier particles to the muon's anomalous moment scales as $(m_\mu/m_e)^2 \simeq 43,000$ with respect to the electron's, the diagrams with quark loops, and to a lesser extent, weak bosons, contribute measurably to a_μ. This makes the precise measurement of a_μ a powerful test of the theoretical understanding of the hadronic and weak contributions.

Because of the presence of virtual electron loops, higher order QED contributions to a_μ are enhanced in comparison with a_e. To match the present experimental precision goals it is necessary to consider 5 terms of the expansion in α:

$$a_\mu^{QED} = \sum_{n=1}^{5} C_n^{(\mu)} (\frac{\alpha}{\pi})^n, \tag{1.11}$$

with $C_1^{(\mu)} = 0.5$, $C_2^{(\mu)} = 0.765\ 857\ 376(27)$, $C_3^{(\mu)} = 24.050\ 508\ 98(44)$, $C_4^{(\mu)} = 126.07(41)$ and $C_5^{(\mu)} = 930(170)$ [6]. The coefficients in this expansion are different from those for a_e, due to increased contributions from virtual electrons, muons and tauons. With the relative error of 25 parts per billion, a_μ^{QED} is the best theoretically understood part of the muon anomaly.

The contribution from the hadronic loops, which was first observed in the muon $(g-2)$ experiment at CERN [12], may be written as

$$a_\mu^{Had} = a_\mu^{Had(2)} + a_\mu^{Had(3)} + a_\mu^{Had(\gamma\gamma)} + \ldots, \tag{1.12}$$

where $a_\mu^{Had(2)}$ and $a_\mu^{Had(3)}$ arise from hadronic vacuum polarization and are of the order $(\alpha/\pi)^2$ and $(\alpha/\pi)^3$ respectively; and $a_\mu^{Had(\gamma\gamma)}$ comes from hadronic light-on-light scattering [6].

The bulk of hadronic contribution comes from $a_\mu^{Had(2)}$, representing the vacuum polarization insertion in the Schwinger diagram (Figure 1.2(a)). This correction cannot be calculated from first principles of QED, but can be determined using dispersion

[1] This limit is exceeded only by high-energy comparison of a different nature on the *neutral* $K^0{\cdot}\overline{K^0}$ system

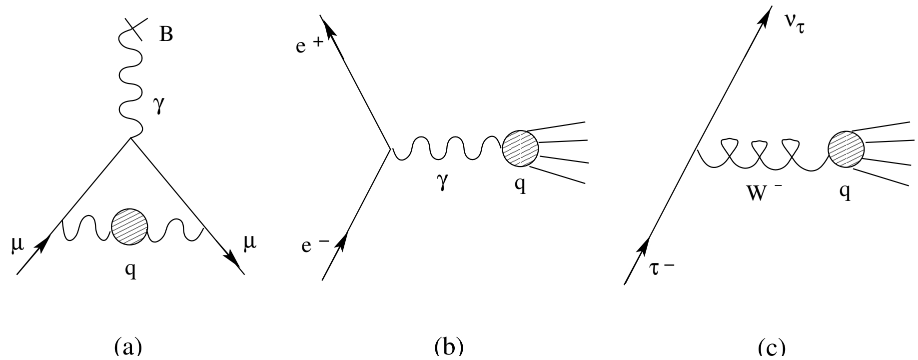

Figure 1.2: The Feynman graphs of (a) the lowest order hadronic correction (hadronic vacuum polarization), and the hadroproduction processes used in its evaluation: (b) electron-positron annihilation, and (c) hadronic τ-decay.

relations, together with experimental data on $e^+e^- \to hadrons$ and hadronic τ-decays (Figure 1.2(b,c)).

The leading order hadronic vacuum polarization contribution to a_μ can be calculated via the dispersion integral

$$a_\mu^{Had(2)} = \frac{1}{4\pi^3} \int_{4m_\pi^2}^{\infty} ds\ \sigma_{Had}(s)\ K(s), \tag{1.13}$$

where $\sigma_{Had}(s)$ is the total $e^+e^- \to hadrons$ cross-section as a function of the center of mass energy-squared (s), and $K(s)$ is the QED kernel function given by:

$$K(s) = x^2\left(1 - \frac{x^2}{2}\right) + (1+x)^2\left(1 + \frac{1}{x^2}\right) \times \left(\ln(1+x) - x + \frac{x^2}{2}\right) + \frac{(1+x)}{(1-x)}x^2 \ln x, \tag{1.14}$$

with $x = (1-\beta_\mu)/(1+\beta_\mu)$ and $\beta_\mu = (1-4m_\mu^2/s)^{1/2}$ [13]. The function $K(s)$ decreases monotonically with increasing s.

The weak W current in $\tau \to \nu_\tau + hadrons$ can be related to the electromagnetic current in $e^+e^- \to hadrons$ through the conserved vector current (CVC) hypothesis, assuming isospin invariance and the absence of second class currents. The τ-decays with an even number of pions (even G-parity) in the final state provide additional information relevant in the evaluation of $a_\mu^{Had(2)}$ [13], since these decays go exclusively through the vector currents if there are no second class currents [14].

The leading order vacuum polarization correction is currently the source of the biggest uncertainty in the Standard Model prediction of a_μ. This error arises from

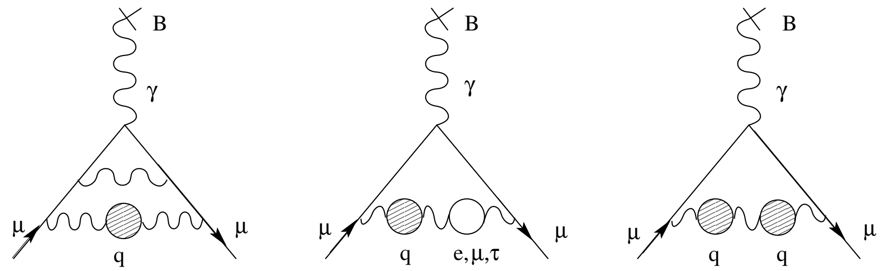

Figure 1.3: The Feynman graphs of some higher-order hadronic corrections to a_μ.

the precision with which the cross-sections of the hadroproduction processes, $e^+e^- \rightarrow hadrons$ and $\tau \rightarrow \nu_\tau + hadrons$, are known from experiment.

The most accurate calculation, which included the information obtained from the analysis of the data from both the production of hadrons in the e^+e^- collisions and the tauon decay, was done by Davier and Höcker [15, 16]:

$$a_\mu^{Had(2)} = 6924(62) \times 10^{-11}. \tag{1.15}$$

The current 0.53 ppm error is expected to decrease significantly, once the new experimental data [17] are included in the calculation.

In a more conservative approach, with the e^+e^- data alone used to evaluate the leading order vacuum polarization correction, Jegerlehner obtained [18]:

$$a_\mu^{Had(2)} = 6974.0(104.5) \times 10^{-11}, \tag{1.16}$$

which agrees with the result given by Eqn. 1.15 within errors.

The diagrams for some higher-order hadronic contributions to a_μ, involving vacuum polarization, are shown in Figure 1.3. The total third-order contribution is [19]:

$$a_\mu^{Had(3)} = -100(6) \times 10^{-11}. \tag{1.17}$$

The part of the hadronic contribution, coming from light-on-light scattering (see Figure 1.4), cannot be calculated either from dispersion relations or using QED. A number of calculations have been performed using chiral perturbation theory, simple quark model and vector dominance model, and the uncertainty in the value of this part has been reduced to 21 parts per billion[2]:

$$a_\mu^{Had(\gamma\gamma)} = -85(25) \times 10^{-11}. \tag{1.18}$$

[2]The value given by Eqn. 1.18 is cited from Ref. [9]. Recent calculations [20, 21] found the sign of the contribution to a_μ from hadronic light-on-light scattering to be positive rather than negative.

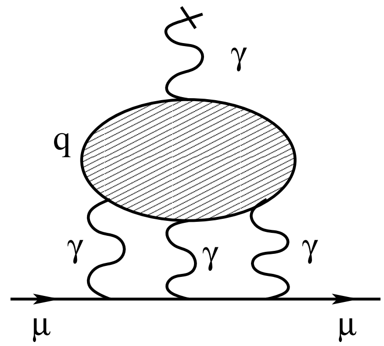

Figure 1.4: The hadronic light-on-light scattering.

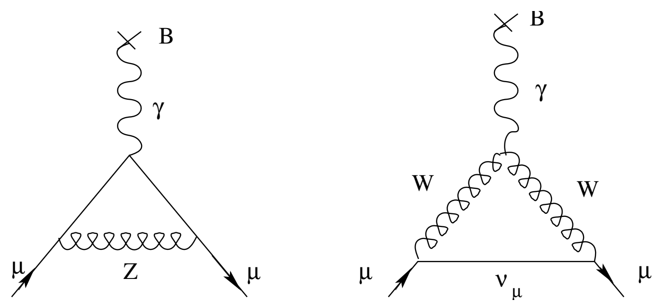

Figure 1.5: The single-loop electroweak contributions to a_μ.

Adding Eqns. 1.15, 1.17 and 1.18 gives the total hadronic contribution:

$$a_\mu^{Had} = 6739(67) \times 10^{-11}. \tag{1.19}$$

The weak interaction contribution, arising from diagrams with W- and Z-bosons, has been calculated up to two loops. The single-loop Feynman diagrams are shown in Figure 1.5. The Higgs boson produces a negligible contribution to a_μ for any reasonable estimated value of its mass [18, 22].

The current theoretical prediction of the total value of a_μ and the sizes of each contribution are given in Table 1.1.

1.2.3 a_μ and "New Physics"

If there are new particles which couple to the leptons, directly or via photons, they too will contribute to the anomalous moment. Therefore, "new physics" beyond the Standard Model could manifest itself in a disagreement between the experimentally measured value and the standard theoretical prediction. Such effects are generally proportional to $(m_l/\Lambda)^2$, where m_l is the lepton mass, and Λ is the mass scale of "new

Table 1.1: Standard Model prediction for a_μ.

Contribution	Value, $\times 10^{-10}$	Relative size and error, ppm	Refs.
a_μ^{QED}	11 658 470.56(0.29)	999 940.90 $\pm$ 0.025	[9]
a_μ^{Had}	673.9(6.7)	57.80 $\pm$ 0.57	[9, 16, 19]
a_μ^{Weak}	15.1(0.4)	1.30 $\pm$ 0.03	[9]
Total a_μ^{SM}	11 659 159.6(6.7)	1 000 000.00 $\pm$ 0.57	[9]

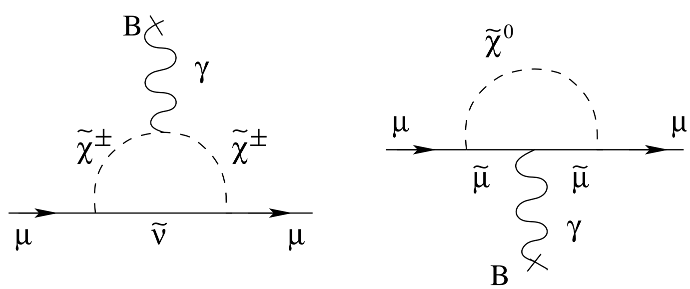

Figure 1.6: The lowest order supersymmetric contributions to $(g-2)_\mu$.

physics". Since the mass of the muon is approximately 207 times greater than that of the electron, the a_μ measurement, even though lacking the spectacular precision achieved for a_e, would be much more sensitive to such contributions, and could be used to constrain or indirectly confirm new theories.

A number of speculative theories have been proposed in order to achieve a more comprehensive theory for particle physics than the present Standard Model.

Supersymmetry (SUSY) implies the existence of partners for all known fundamental particles. The leading supersymmetric contributions to a_μ stem from processes involving the super-partners of leptons and gauge bosons: smuon-neutralino and sneutrino-chargino loops (Figure 1.6). The effect is given approximately by:

$$|\delta a_\mu^{SUSY}| \approx \frac{\alpha}{8\pi \sin^2\theta_W} \frac{m_\mu^2}{\tilde{m}^2} \tan\beta \cdot \left(1 - \frac{4\alpha}{\pi} \ln \frac{\tilde{m}}{m_\mu}\right), \tag{1.20}$$

where θ_W is the weak (Weinberg) mixing angle, $\tilde{m}$ is a typical SUSY loop mass, and the parameter $\tan\beta$ describes the mixing of ground states of the Higgs-doublet in SUSY [18]. For the scenarios with a large $\tan\beta \simeq 40$, the Brookhaven experiment could probe $\tilde{m}$ at the 750 GeV level (for $\delta a_\mu^{SUSY} = \pm 10 \times 10^{-10}$) [9].

Just as the proton substructure produces a g-value which is not equal to two, the muon substructure would also contribute to the anomalous magnetic moment. A $(g-2)$ measurement for the muon at the level of 0.35 ppm would restrict the substructure scale at around 4-5 TeV [7].

In the models where the muon mass is generated by quantum loops, similar loop effects will also produce additional contributions to a_μ, given by

$$\delta a_\mu = C\frac{m_\mu^2}{\Lambda^2}, \qquad C \sim \mathcal{O}(1), \tag{1.21}$$

where Λ is the mass scale of the mechanism responsible for generating m_μ [23].

Some other potential "new physics" contributions to a_μ are discussed in Ref. [18].

Chapter 2

Muon $(g-2)$ Measurements at CERN

In the late 1940s, it was realized that the quantum fluctuations in the electromagnetic field could induce an extra magnetic moment [5, 24], so that $g \neq 2$ for the electron. Experimental confirmations of this were found in the studies of the fine structure of atomic hydrogen [2], Lamb shift [25], and in the magnetic moments of neutral atoms [4].

Crane and collaborators [26] showed that the electrons could be polarized and analyzed by Mott scattering by a heavy element. By introducing a magnetic field between polarizer and analyzer they were able to measure g for the electron.

It was then realized that if the spin $(\vec{s})$ and the momentum vector $(\vec{p})$ are both perpendicular to the magnetic field $\vec{B}$, the change of the beam polarization, $(\vec{s} \cdot \vec{p})$, with time would be a sensitive measure of the magnetic anomaly.

For a charged spin-$\frac{1}{2}$ particle moving in a uniform constant magnetic field, the spin precession frequency, is generally given as a sum of Larmor and Thomas terms:

$$\omega_s = g\frac{e}{2mc}B + (1-\gamma) \cdot \frac{e}{\gamma mc}B, \tag{2.1}$$

and the cyclotron frequency is:

$$\omega_c = \frac{e}{\gamma mc}B. \tag{2.2}$$

Thus the frequency of the relative precession of spin with respect to the momentum vector turns out to be proportional to the anomalous moment and independent of the particle momentum:

$$\omega_a = \omega_s - \omega_c = \frac{g-2}{2} \cdot \frac{e}{mc}B = a_\mu \frac{e}{mc}B. \tag{2.3}$$

In the 1950s, a series of measurements of the *electron* anomaly were performed employing this idea, with the results precise up to the 1000-ppm level, in agreement

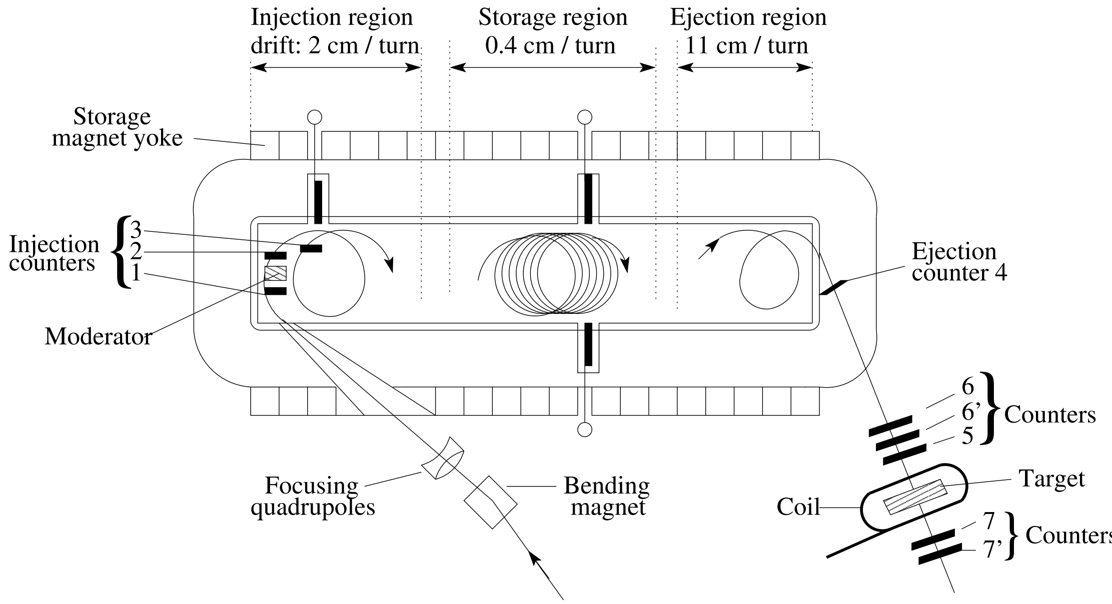

Figure 2.1: CERN-I experiment: the general view of the experimental apparatus (shown not to scale).

with theory [27]. It was then pointed out that a measurement of the muon magnetic anomaly would test QED at higher momentum transfers (at "shorter distances") than a similar measurement of a_e, due to the enhanced sensitivity of a_μ to interactions with heavier particles.

In 1957, parity nonconservation was observed in the weak decays $\pi^+ \to \mu^+\nu_\mu$ and $\mu^+ \to e^+\nu_e\overline{\nu}_\mu$ [28]. It was established that the muons born in pion decays were strongly polarized. Moreover, in its decay the muon shows its polarization direction through the anisotropic emission of the decay electron. Therefore, polarization of the muon beam may be determined from the angular distribution of the decay electrons.

The work on a new measurement started at CERN in 1958.

2.1 First CERN Experiment (1958-1961)

The main objectives of the first CERN experiment (CERN-I) were to further test the validity of QED at shorter distances, and to explore the possibility of the existence of unknown interactions, which were, at the time, believed to cause the mass difference between the electron and the muon [29].

The general view of the experimental apparatus is given in Figure 2.1. Longitudinally polarized muons, of 150 MeV/c momentum, formed by forward decays in flight of pions from the CERN Synchro-cyclotron, were injected into a 6 m long storage magnet possessing a magnetic field (B=1.6 T) of high uniformity. After slowing down in the beryllium moderator, the muons described close to 1000 quasi-circular orbits, slowly displaced due to the longitudinal gradient of the magnetic field, before reaching the end of the magnet and being ejected. The magnetic field was carefully shaped in such a way that the positron drift was significantly slower in the storage region (0.4 cm per turn), than in the injection and ejection regions (2 and 11 cm/turn respectively). Injected muons were indicated by the counter signature 1·2·3 (i.e. hits were registered in the injection counters 1, 2 and 3, as shown in Figure 2.1), and ejected muons by the signature 4·6·6'·5·$\overline{7}$.

The difference between the final and the initial polarization angles was proportional to the time the muons spent in the magnetic field:

$$\theta_s - \theta_0 = a_\mu \frac{e}{mc} \langle B \rangle t \tag{2.4}$$

where $\langle B \rangle$ is the magnetic field averaged over the trajectory, and t is the time of flight of muons between the injection counter 2 and the ejection counter 4.

The final polarization state was measured by bringing the muons to rest in a field-free insulating target of the polarization analyzer and observing their decay. The flipping coil produced a pulsed vertical magnetic field of such intensity and duration that the muon spin rotated in the horizontal direction by $\pm 90^\circ$ before the muon decayed. The comparison in the same electron counter of the decay electron intensity at $+90^\circ$ and -90° flipping yielded the value of the transverse component of the spin polarization. To increase the efficiency of electron detection, two sets of counters were used, forward 7·7 and backward 6·6', with the results for each set being evaluated separately.

From the number of decay electron counts in a particular set of counters for $+90^\circ$ or -90° flipping of the muon spin, n_+ and n_- respectively, the asymmetry was computed as:

$$A \equiv \frac{n_+ - n_-}{n_+ + n_-} = A_0 \sin \theta_s(t), \tag{2.5}$$

where θ_s is the spin direction with respect to the normal to the analyzer.

A total of 936 thousand events were recorded. The dependence of the decay asymmetry on the storage time is shown in Figure 2.2. The short time scale of the experiment, coupled with the finite accuracy to which the spin direction could be observed, was a major factor in the experimental error.

The result of the experiment was a measurement of a_μ with a 0.4% precision, in good agreement with the theoretical prediction at that time:

$$a_\mu\,(\mathrm{CERN-I}) = (1162 \pm 5) \times 10^{-6}, \tag{2.6}$$

$$a_\mu\,(\mathrm{QED}, 1957) = 1165 \times 10^{-6}. \tag{2.7}$$

This established that the properties of the muon correspond exactly to those of a

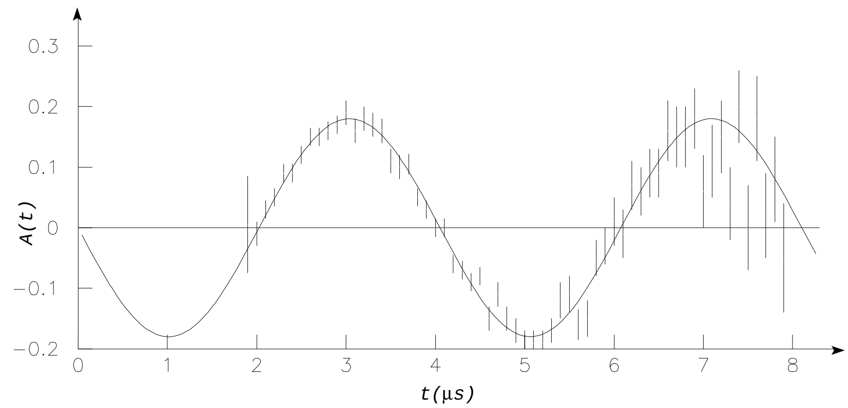

Figure 2.2: CERN-I experiment: electron asymmetry plotted vs storage time t, together with the fitting function $A(t) = A_0 \sin(a_\mu \frac{e}{mc} \langle B \rangle t + \theta_0)$ [29].

heavy electron. Apart from their masses and their association in weak interaction with two distinct kinds of neutrinos, the two particles appeared to be identical. The theory of quantum electrodynamics was tested for momentum transfers of up to ~ 1 GeV.

2.2 Second CERN Experiment (1962-1968)

Whereas the time scale of the first experiment was limited to a few microseconds by the natural decay of the muon population ($\tau_0 = 2.2\mu$s), and therefore only two anomalous precession cycles, of $\sim 4\mu$s, could be recorded, the second CERN experiment [30, 31] employed relativistic muons ($\gamma \simeq 12.3$), with the lifetime increased due to the time dilation to $\tau = \gamma\tau_0 \simeq 27\mu$s, which allowed for observation of some 50 precession cycles.

The CERN-II experiment used a weak-focusing storage ring magnet, 5 m in diameter (see Figure 2.3), providing $B = 1.7$ T. A beam of 10 GeV protons from the CERN Proton Synchrotron interacted with a target inside the storage ring, producing pions of ≈ 1.3 GeV/c momentum which would start orbiting around the ring. About 20% of the pions decayed in one turn, and the muons with slightly lower momentum, ejected at small forward angles, remained stored in the ring. The number of muons produced per pion (trapping efficiency) was $5 \cdot 10^{-3}$, for 1.3 GeV/c pions. The muons injected in this process were forward polarized on average. Undecayed pions, higher momentum muons, and stable particles from the target would eventually hit the target assembly and be lost. A lead block and concrete shielding placed inside the ring prevented these particles from being scattered onto the electron counters.

Four nuclear magnetic resonance (NMR) probes were moved pneumatically into

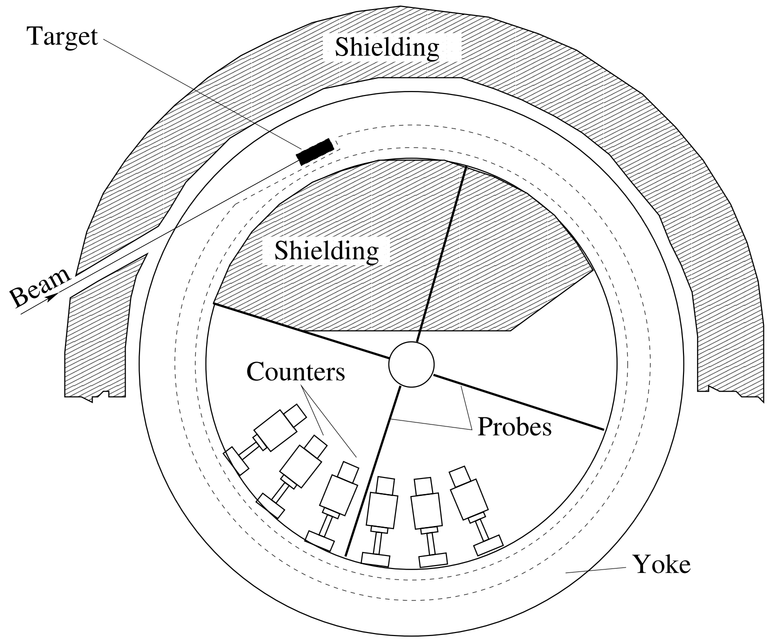

Figure 2.3: CERN-II experiment: the apparatus.

the center of the storage magnet aperture every 100 cycles of the beam injection, to measure the magnetic field inside the storage region.

The polarization direction of the muons as a function of time was followed by recording electrons emitted by muon decay in flight. The detection electronics was biased to accept only the highest energy electrons ($E > 780$ MeV), coming from forward decay in the muon rest frame, and producing a large pulse in lead-scintillator sandwich shower detectors. As a result, the counting rate, $N(t)$, was modulated by the muon precession due to the anomalous moment at frequency ω_a :

$$N(t) = N_0 e^{-t/\tau}(1 - A\cos[\omega_a t + \phi]), \tag{2.8}$$

$$\omega_a = a_\mu \frac{e}{m_0 c}\langle B\rangle. \tag{2.9}$$

In Equation 2.8, τ is the dilated muon lifetime, A is the decay asymmetry, and ϕ is the phase of the anomalous precession. The average magnetic field for the ensemble of the muons, $\langle B\rangle$, was measured in terms of the corresponding mean proton NMR precession frequency in water. The distribution of the detected decay electrons as a function of time is shown in the top part of Figure 2.4.

One of the main factors limiting the precision of the measurement was the use of the radial magnetic gradient for vertical focusing. This implied a field variation of 0.4% over the 8 cm radial aperture of the storage region. Therefore, it was important to determine the mean radius and the detailed radial distribution of the ensemble of muons which contributed to the electron counts. This had been obtained by measurements related to the muon rotation frequency. At the injection, the pulse was only 5-10 ns long, and given the rotation period of 52.5 ns, the muons were initially bunched, and the counting rate in the decay electron counters was modulated during the first few microseconds (as shown in the lower part of Figure 2.4). Analysis of the stored muon beam debunching yielded the mean radius with a precision of $\pm$ 3 mm. The average magnetic field weighted by the muon distribution was determined to a precision of 160 ppm.

To obtain ω_a, a maximum likelihood fit to the data was performed with the function

$$N(t) = N_0 e^{-t/\tau}(1 - A\cos[\omega_a t + \phi])(1 + A_L e^{-t/\tau_L}) + Bg, \tag{2.10}$$

similar to Eqn. 2.8, with the parameters A_L and τ_L added to account for the muon losses, and Bg to include a constant background.

The final result of the second CERN experiment had an accuracy of 270 ppm:

$$a_\mu\,(\mathrm{CERN-II}) = (116\ 616 \pm 31) \times 10^{-8}, \tag{2.11}$$

which initially disagreed with the theoretical prediction by 1.7 standard deviations. This disagreement stimulated the theorists to calculate the contribution of QED light-on-light scattering to the third order in α [32], thus removing the discrepancy

$$a_\mu^{exp} - a_\mu^{theory}\,(1972) = (28 \pm 31) \times 10^{-8} = (240 \pm 270)\ \mathrm{ppm}. \tag{2.12}$$

The second CERN measurement further established the muon-electron universality. The relativistic time dilation was verified to within 1.1% accuracy (for $\gamma = 12.3$).

2.3 Third CERN Experiment (1969-1976)

For the third experiment at CERN [12], an improved storage ring was built, consisting of 40 C-shaped dipole magnets, fit together exactly to provide a uniform field of 1.47 T (see Figure 2.5). The vertical focusing was provided by electric quadrupoles, which were mounted inside the vacuum chamber of the magnet and covered 72% of its circumference.

In the presence of the combined magnetic field $\vec{B}$ and electric field $\vec{E}$ (both perpendicular to $\vec{\beta}$), the angular frequency, ω_a, of the spin relative to the momentum, is given by:

$$\vec{\omega_a} = \vec{\omega_s} - \vec{\omega_c} = -\frac{e}{mc}[a_\mu \vec{B} - (a_\mu - \frac{1}{\gamma^2 - 1})\vec{\beta} \times \vec{E}], \tag{2.13}$$

where $\vec{\beta} = \vec{v}/c$, $\gamma = 1/\sqrt{1-\beta^2}$, and assuming that $E/c << B$ and $\vec{\beta} \cdot \vec{B} \simeq 0$. The dependence of ω_a on the electric field was eliminated by storing muons with the

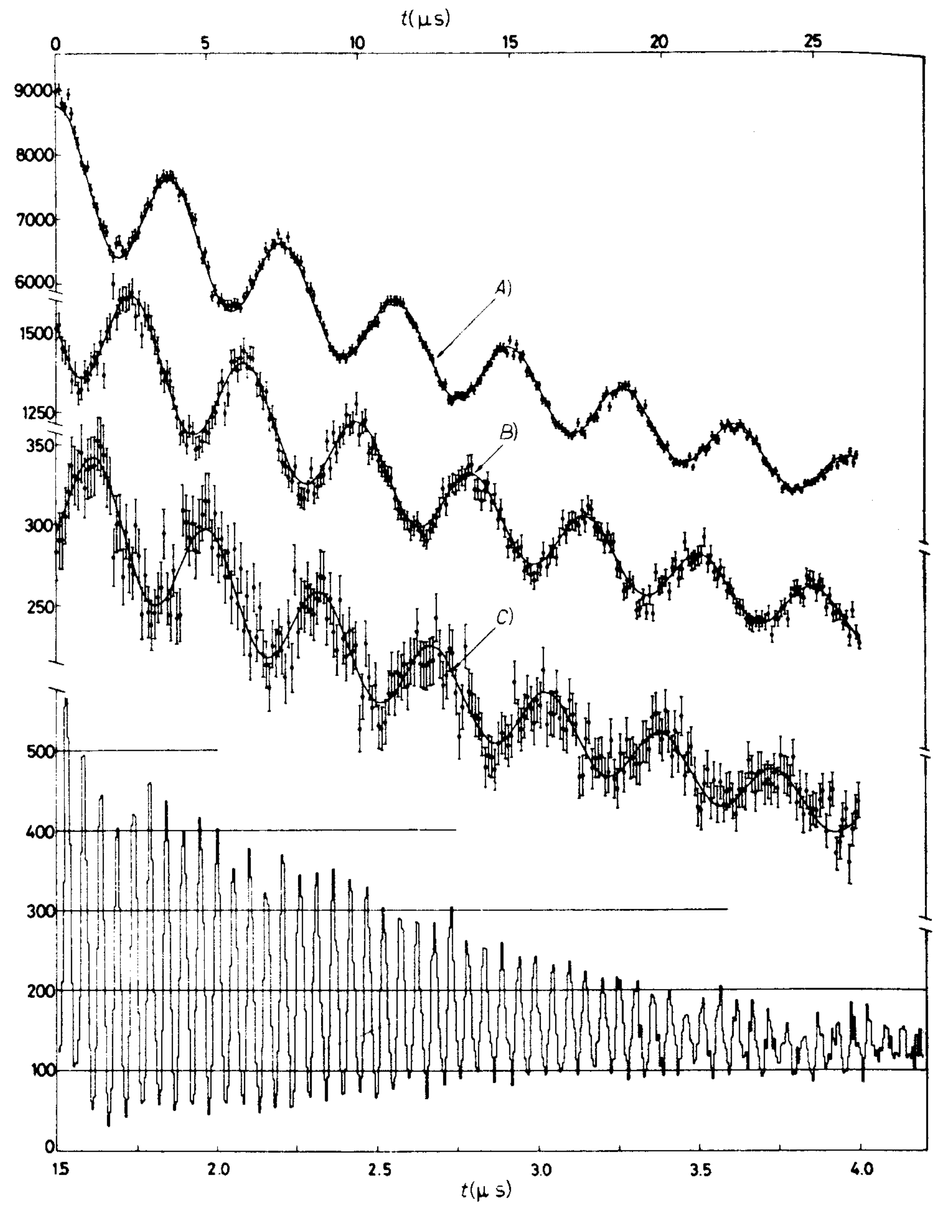

Figure 2.4: CERN-II experiment: distribution of decay electrons vs time. A) from 20 to 45 μs, B) from 65 to 90 μs, C) from 105 to 130 μs. The lower curve shows the rotation frequency of the muon as seen at early time [31].

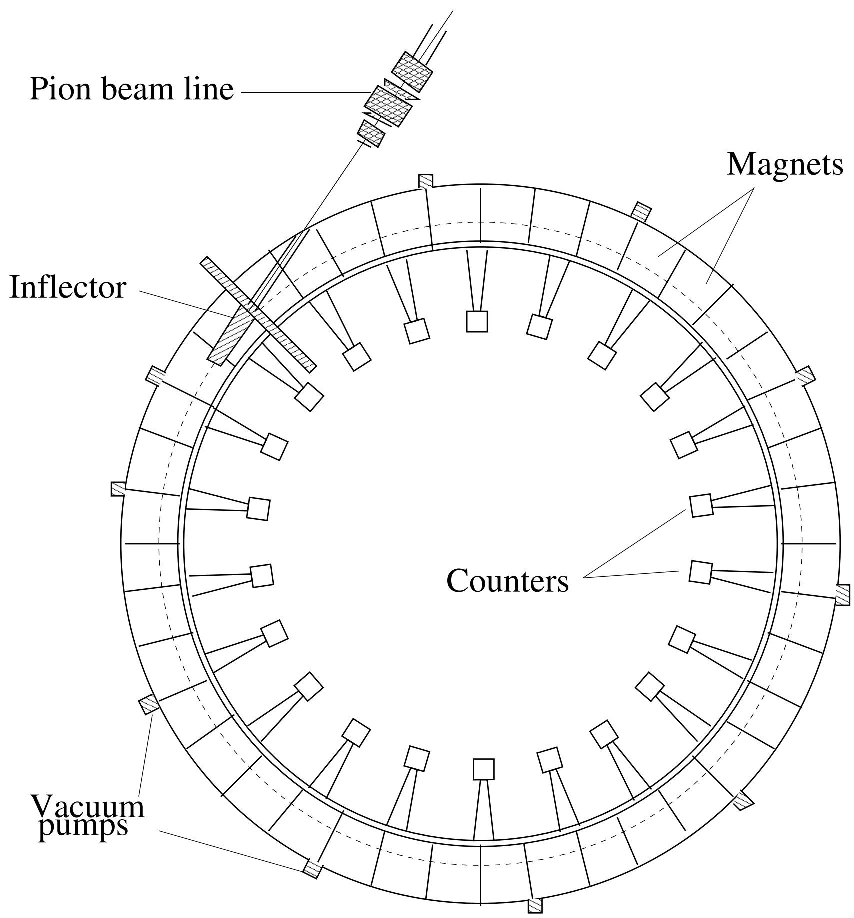

Figure 2.5: CERN-III experiment: the apparatus.

"magic" γ:

$$\gamma = \sqrt{1 + \frac{1}{a_\mu}} = 29.30, \tag{2.14}$$

corresponding to a muon momentum $p_\mu = 3.094$ GeV/c. The increased relativistic factor γ brought the added advantage of the further dilated muon lifetime: now 64 μs vs 27 μs in the second CERN experiment.

The protons from the CERN Proton Synchrotron were guided to an external copper target. The beamline elements were tuned to collect the secondary products over a wide solid angle and select the pions of the $(3.11 \pm .02)$ GeV/c momentum (slightly higher than the "magic" value), resulting in a ten-fold increase in the intensity over the previously used internal target. The almost parallel beam was injected by means of a pulsed inflector into the storage region, which was held under vacuum. The stored muons (with the "magic" momentum) then came from almost forward

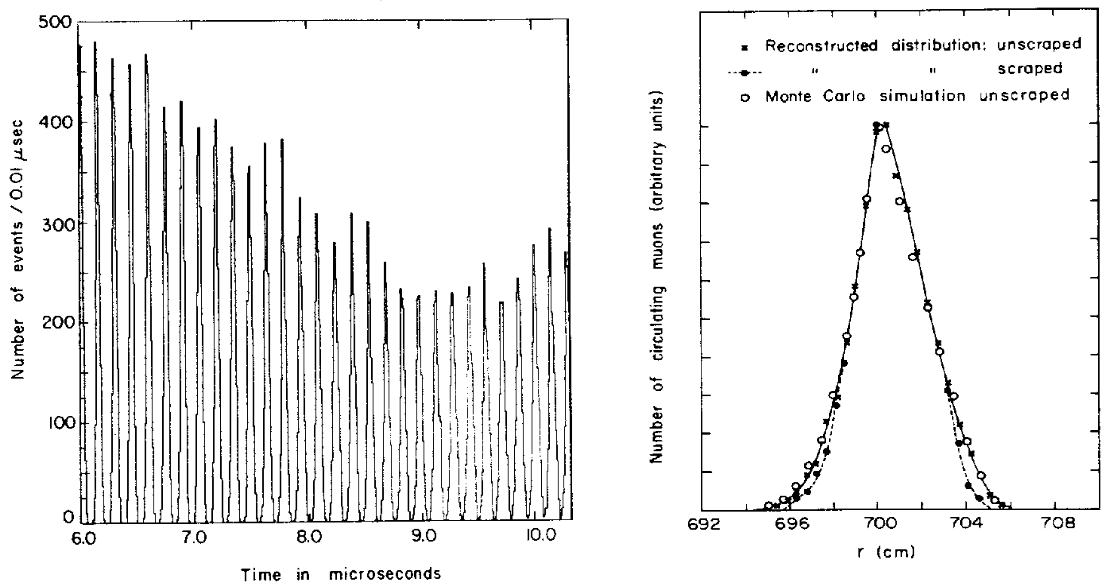

(a) (b)

Figure 2.6: CERN-III experiment: (a) electron count rate at early time shows the bunched structure ("fast rotation"); (b) radial distribution of stored muons calculated from the beam debunching rate [12].

decays and had a polarization of approximately 95% (another improvement over the CERN-II experiment in which the muon polarization was only 26%).

The reduction in the background generated by the injected beam allowed for the use of more lead-scintillator calorimeter detectors, now 22 of them, spaced uniformly all around the inside of the ring, improving the decay electron count rate. The calorimeter signal was enhanced in photomultiplier tubes (PMTs), and then sampled by fast electronics.

Between groups of data-taking runs, the vacuum chambers were removed from the storage and the magnetic field was mapped using a system of 8 NMR probes mounted on a measuring machine driven around the ring. During the data-taking, the field was continuously monitored in 37 out of 40 magnets with small NMR probes, which could be inserted into the storage region without breaking the vacuum. As in the previous experiment, the muon radial distribution was obtained from the analysis of rotation frequency (see Figure 2.6).

The statistical error in determination of the anomalous precession frequency, ω_a, is inversely proportional to the asymmetry (A) of the modulation in the decay elec-

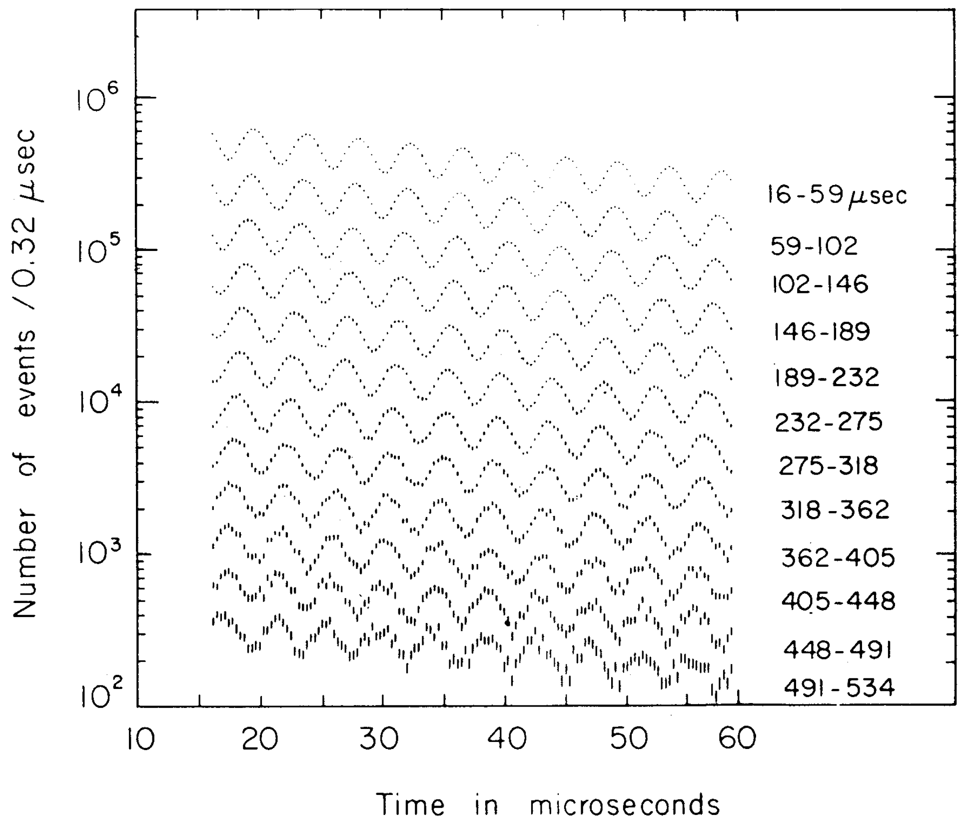

Figure 2.7: CERN-III experiment: the time spectrum of decay electrons [12].

tron time spectrum multiplied by the square root of the number of decay electrons detected (N) [12]:

$$\Delta\omega_a = \frac{\sqrt{2}}{2\pi\tau A\sqrt{N}}. \tag{2.15}$$

Both A and N depend on the calorimeter energy threshold: the number of detected electrons decreases, as the threshold is raised, whereas the decay asymmetry increases. Thus, in the ideal case, to minimize the statistical error, the value of the energy threshold should be chosen to maximize the value of $A\sqrt{N}$, which in the case of CERN-III experiment would be 1500 MeV. In the reality, however, other factors such as finite resolution of the detectors, electron energy losses in the vacuum chamber walls, the change in the system gain between the test and experimental environments had to be taken into account. The optimal threshold for the electron energy selection was found to be around 700 MeV.

In total, approximately 62 million high-energy decay electrons and 72 million positrons were detected. A sample of the electron decay data from CERN-III experiment is shown in Figure 2.7.

The maximum likelihood fit to the data was performed with the function:

$$N(t) = N_0 \cdot \Big(e^{-t/\tau}(1 - A\cos[\omega_a t + \phi]) \cdot (1 + A_L e^{-t/\tau_L}) + Bg\Big), \tag{2.16}$$

where the parameters A_L, τ_L and Bg have same meaning as in Eqn. 2.10. Systematic corrections to the value of ω_a were applied to account for the time shifting effect ("time-slewing") due to the high counting rates experienced by the counters and fast electronics shortly after injection. Such time-slewing could be observed and measured directly in the experiment using light-emitting diodes.

The anomalous precession frequency (ω_a) and the Larmor precession frequency for muons in the magnetic field $\langle B\rangle$ can be written as

$$\omega_a = a_\mu \frac{e}{m_\mu c}\langle B\rangle, \tag{2.17}$$

$$\omega_\mu = \lambda\omega_p = g\frac{e}{2m_\mu c}\langle B\rangle = (1 + a_\mu)\frac{e}{m_\mu c}\langle B\rangle, \tag{2.18}$$

where ω_p is the free proton NMR precession frequency in the same magnetic field seen by the muons, and the ratio of muon to proton magnetic moments $\lambda = \mu_\mu/\mu_p$. Therefore, the anomalous magnetic moment could be determined as:

$$a_\mu = \frac{\omega_a/\omega_p}{\lambda - \omega_a/\omega_p}. \tag{2.19}$$

The result of the CERN-III measurement was

$$a_{\mu^+} = 1\ 165\ 911(11) \times 10^{-9} \quad (10\ \text{ppm}) \tag{2.20}$$

$$a_{\mu^-} = 1\ 165\ 937(12) \times 10^{-9} \quad (10\ \text{ppm}) \tag{2.21}$$

which, assuming CPT-invariance, combined to the average for μ^+ and μ^-:

$$a_\mu\ (\mathrm{CERN-III}) = 1\ 165\ 924(8.5) \times 10^{-9} \quad (7\ \text{ppm}), \tag{2.22}$$

in agreement with the theoretical prediction at the time:

$$a_\mu^{exp} - a_\mu^{theory}\ (1978) = (6.7 \pm 8.4) \times 10^{-9} = (5.7 \pm 7.2)\ \text{ppm}. \tag{2.23}$$

This agreement confirmed the presence of the hadronic contribution to the muon anomaly.

Chapter 3

Experiment E821 at BNL

Experiment E821 at Brookhaven Alternating Gradient Synchrotron (AGS) is designed to measure a_μ to 0.35 ppm. The general method is similar to that of the third CERN experiment, as described in Section 2.3, with a number of improvements. These include: (1) the use of the AGS proton beam with the intensity a factor of 200 greater than the CERN proton beam; (2) a superferric magnet storage ring of high stability and homogeneity, and an improved NMR-based magnetic field mapping system; (3) the use of μ injection into the storage ring; (4) an improved electron spectrometer system with higher energy resolution; (5) the use of fast modern electronics; (6) the use of the significantly increased power of modern computers for data acquisition and analysis.

3.1 Alternating Gradient Synchrotron

The Alternating Gradient Synchrotron [33] began operating in 1960. The 200 MeV linear accelerator produces protons, which are injected into the AGS booster and accelerated to 1.6 GeV. The protons are then transferred to the AGS ring where they are accelerated to higher energies. For the muon $(g-2)$ experiment, the AGS is capable of producing a fast-extracted proton beam of about 7×10^{12} protons per bunch at 24 GeV/c. Depending on the mode of operation, 6 to 12 proton bunches can be extracted per AGS cycle of about 2.6 seconds. During the experimental run in 1999, all of the data subsequently used in the analysis were taken during the 6-bunch extraction mode, with the beam intensity of 20-40 Tera-protons (Tp) per AGS cycle.

3.2 Beamlines

The schematic drawing of the $(g-2)$ beamlines is given in Figure 3.1.

Each AGS bunch was extracted by a pulsed kicker magnet into the U-V beamline at intervals of 33 ms. After the initial extraction the beam was carried to the dipole magnets VD3, VD4 where the protons were deflected approximately 3° to the V-line

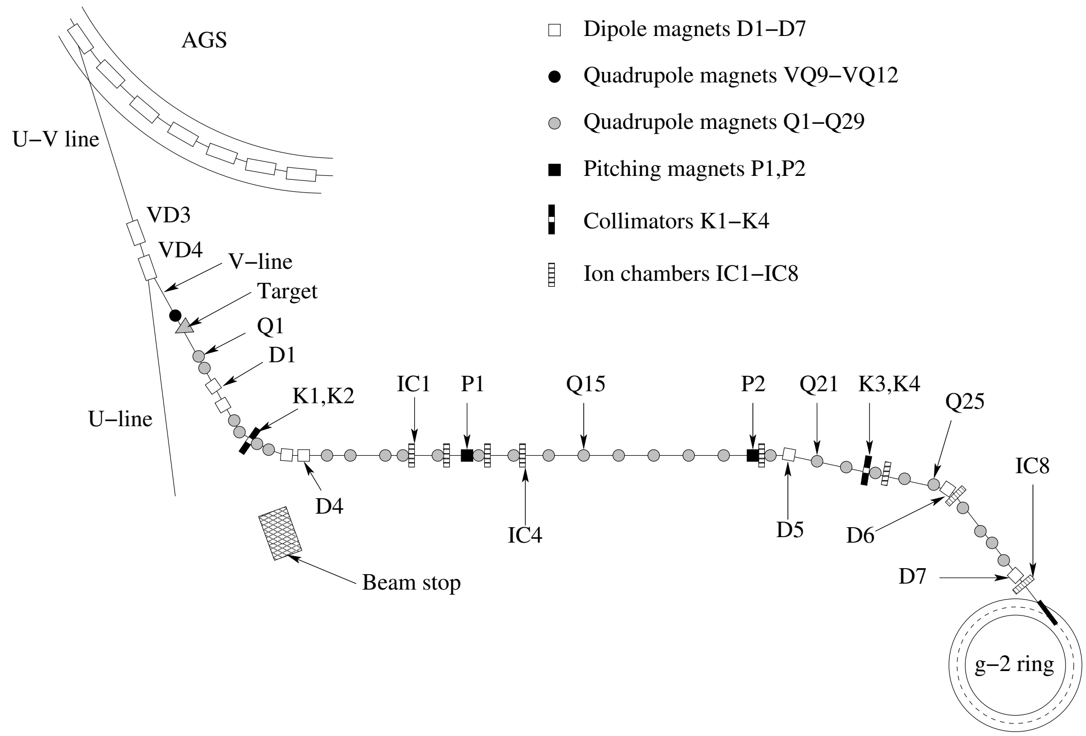

Figure 3.1: Scheme of the $(g-2)$ beamlines.

target section. The beam was then focused on the V-target by quadrupole magnets VQ9-VQ12 [34].

The nickel target was designed to withstand high beam intensities of up to 60 Tp. The target was steadily rotated about its axis (parallel to the beam direction), to distribute heating from the beam bunches in a cycle, and cooled with water, to reduce the average heating [35].

Beyond the target, the protons were absorbed in the beam stop. The pions born in the collision of the beam with the target were collected by quadrupoles Q1 and Q2 and sent through dipoles D1 and D2 and collimator K1-K2, to ensure selection of pions with a central momentum of 3.11 GeV/c ($\sim$0.5% higher than the "magic" momentum), with momentum width of 0.5% [36]. Following the initial momentum selection, the pions were steered down the 116 m secondary beamline to the storage ring, through focusing and defocusing quadrupoles, pitching magnets, dipoles etc. The final momentum selection was done by the collimator slits K3-K4, onto which the beam was imaged by dipoles D5 and D6, and the quadrupoles Q21-Q25.

Given the pion decay length of 174 m (for $p = 3.11$ GeV/c), approximately 40% of the pions decay in the 89-meter section of the beamline between the slits K1-K2 and K3-K4. Thus, the long secondary beamline allows for the injection of either the

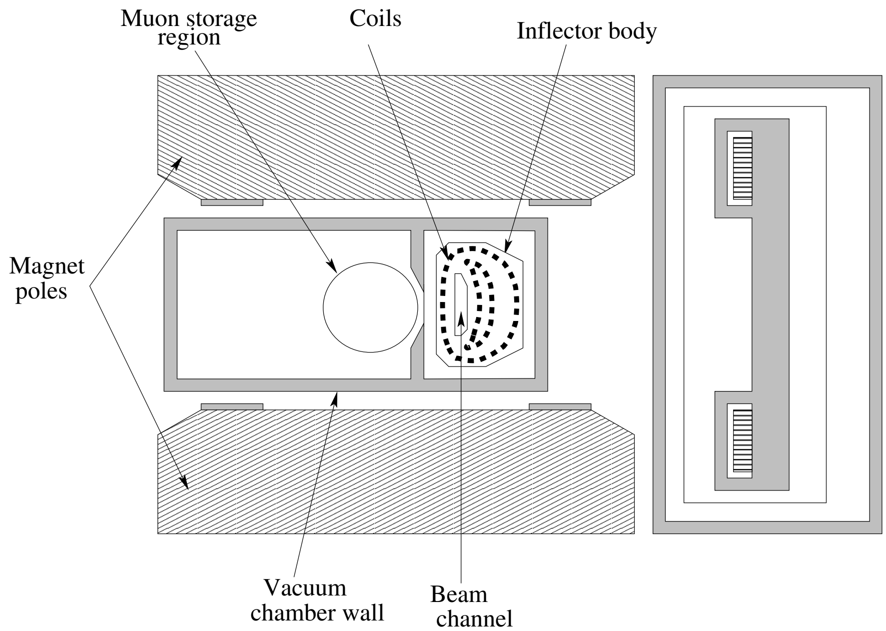

Figure 3.2: Superconducting inflector.

pions or muons from the $\pi \to \mu\nu_\mu$ decay, selected by their momenta at slits K3-K4. With pion injection, 3.11 GeV/c pions are brought to the ring. For muon injection, the decay muons are selected of the “magic” momentum: 3.094 GeV/c.

Ten segmented wire ion chambers (SWICs) were used to monitor the position of the beam inside the transport beamline. The beam could be “tuned” by manipulating the dipole and quadrupole voltage settings, to minimize the pion and muon losses inside the beamline.

A Čerenkov counter (“TØ counter”) was placed at the end of the beamline to measure the time of the bunch injection into the storage ring.

Under unstable conditions, the AGS may extract the beam into the U-V beamline out of time, i.e. after the initial extraction and during the data taking period. This produced background in the decay positron detectors (so-called “flashlets”). A pulsed sweeper magnet was installed in the beamline before the 2000 experimental run. The sweeper shuts down the beamline for a period of about 1 ms following the initial beam extraction, preventing the particles extracted out of time from being injected into the storage ring.

3.3 Superconducting Inflector

The particles were injected into the storage ring through a 1.7-meter-long superconducting inflector [37], with an aperture of 18(w) $\times$ 57(h) mm^2, which created a

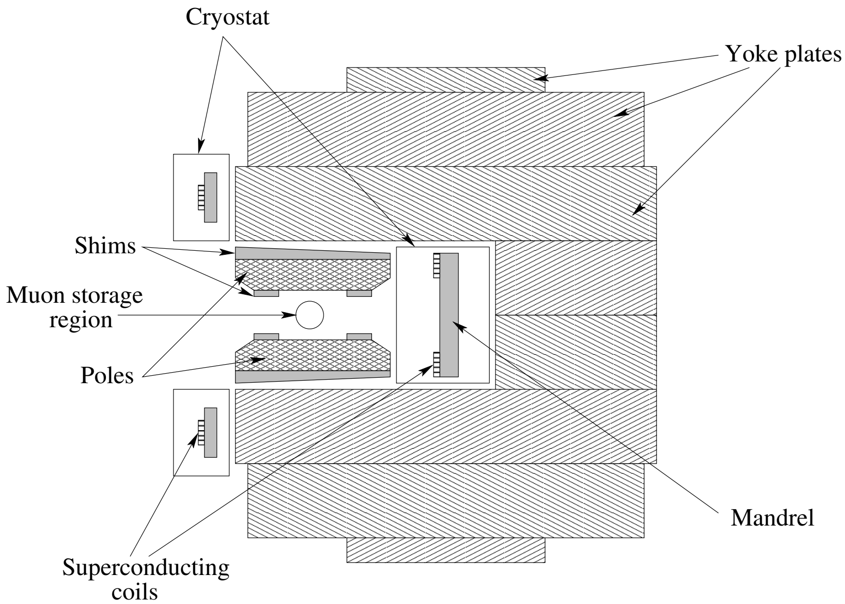

Figure 3.3: The cross-section of the main magnet.

magnetic dipole field, canceling the field from the storage ring. The cross section of the inflector is shown in Figure 3.2. A passive superconducting sheet was used to cancel the inflector fringe field. The imperfect cancellation of this fringe field was a source of one of the biggest systematic uncertainties in the magnetic field measurement in the first three E821 runs. For the 2000 run, a new inflector with an improved shielding was installed.

It was important that the beam enter the storage region as close as possible, and almost tangential to the equilibrium orbit of the ring. The injection point of the $(g-2)$ storage ring was about 77 mm outside the equilibrium orbit, and further manipulation of the beam with a magnetic kicker was required to ensure storage with μ-injection.

3.4 Muon Storage Ring

The muon storage ring [38] provided a highly homogeneous dipole magnetic field of 1.45 Tesla over the storage region, which constrained the 3.094 GeV/c muons to move in a circle with a central orbit radius of 7.112 m. The main $(g-2)$ superferric magnet is C-shaped and has a diameter of 14.2 m. The magnet is excited by three superconducting coils. The cross-section of the magnet is shown in Fig. 3.3.

In order to achieve a highly uniform magnetic field, extensive shimming work was performed, including adjustments to the yoke plates and end shims of the poles, and insertion of iron wedges in the air gaps between the poles and yoke [34].

3.4.1 Magnetic Field Measurement

The value of the magnetic field was obtained from NMR measurements. A pulsed NMR probe was developed and tested for this purpose [39]. The magnetic field was monitored continuously by some 380 such probes placed above and below the storage region. At regular time intervals, typically twice a week, the field throughout the storage region was mapped using 17 NMR probes mounted on a trolley. The probes in the trolley were calibrated against a standard probe [40], which was constructed to measure the NMR frequency of protons in a spherical sample of pure water. The trolley measured the magnetic field in the muon storage region up to a radius of 3.5 cm. The field beyond this radius was obtained by extrapolating the measured moments.

3.4.2 Vacuum Chamber

The storage region itself was 9 cm in diameter (see Figure 3.4), and was maintained at a vacuum of $10^{-7} - 10^{-6}$ Torr. The vacuum chamber consisted of twelve sections. The chamber sections had a scalloped shape on the inside radius to accommodate the twenty-four electron detectors while minimizing the showering in the chamber walls (as shown in Figure 3.5).

The support frame inside each chamber section provided rails for the NMR trolley. Some thirty fixed NMR probes per section were embedded in the top and bottom walls of the vacuum chamber.

3.4.3 Electrostatic Quadrupoles

The storage ring is a weak focusing spectrometer with an average field index

$$n = -\frac{\rho}{\beta B}\frac{\partial E_r}{\partial r}, \tag{3.1}$$

where $\rho = 7.112$ m is the radius of the central orbit, $\beta = v_\mu/c \simeq 1$, and $B = 1.45$ T is the magnetic field at the central orbit. Given a uniform quadrupole field throughout the storage ring, the betatron frequencies are proportional to the cyclotron frequency, f_c, and depend on the field index, n [41]:

$$f_r = f_c\sqrt{1-n} \qquad \text{(radial)}, \tag{3.2}$$

$$f_z = f_c\sqrt{n} \qquad \text{(vertical)}. \tag{3.3}$$

Four pulsed electrostatic quadrupoles, which covered about 39° in each quadrant of the storage ring were mounted on the support frame of the vacuum chamber (Fig-

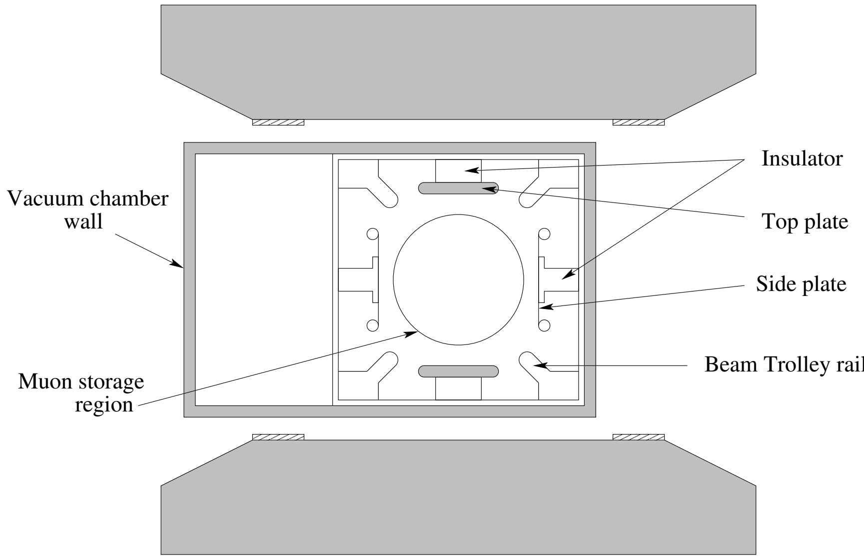

Figure 3.4: A cross-section of the vacuum chamber with electrostatic quadrupole.

ure 3.4). The quadrupoles provided weak focusing (in 1999: $n = 0.135$) to prevent the muons from exiting the ring vertically. The quadrupole plates were pulsed for about 800 μs following each beam injection.

The quadrupoles were also used to "scrape" the muon beam. During "scraping", the quadrupole plates were powered asymmetrically, which moved the stored beam slightly off center so that the muons on the edges of the momentum distribution would hit the copper collimators and be removed. This was done for about 15 μs following the beam injection to make the muon distribution narrower, which reduced the probability of muon losses during the data taking period [35].

3.5 Muon Kicker

Following the pion beam injection, many particles collide with the walls of the vacuum chamber, inflector etc., creating a high background, or "flash", in the detectors. The advantage of the muon injection into the storage ring is that it reduces the initial flash about 50-fold, while producing at least a factor of 5 more stored muons per spill than can be achieved with pion injection. Direct muon injection was accomplished by giving the muon beam a 10-milliradian kick at a quarter of the betatron wavelength from the inflector. This was achieved with a peak current of 4100 A and a half-period of 400 ns. Three pulse-forming networks powered three identical 1.7 m long one-loop kicker sections consisting of 95 mm high parallel plates on either side of the beam. The current pulse was formed by an under-damped LCR circuit. The kicker plate geometry and composition were chosen to minimize eddy currents. Since the muons

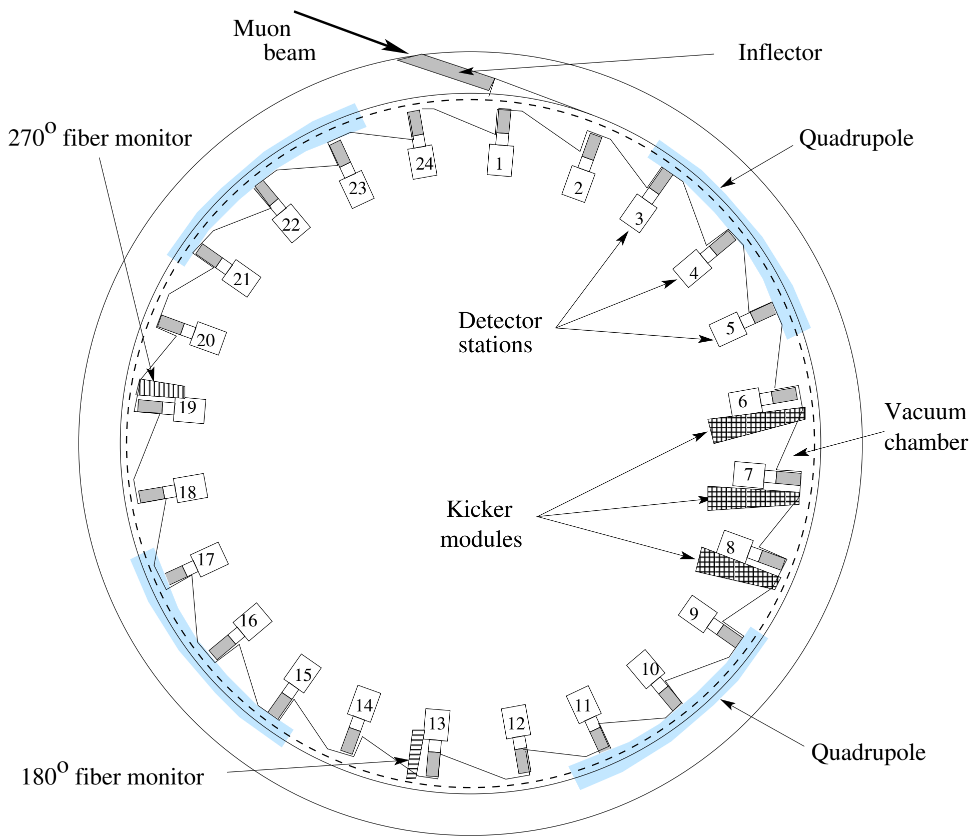

Figure 3.5: A schematic view of the $(g-2)$ storage ring.

circulate in about 149.2 ns, they were kicked several times before the kicker pulse died out [42]. The muon kicker became operable in time for the second E821 experimental run in 1998.

3.6 Scintillating Fiber Monitors

The profile of the stored muon distribution was monitored by the scintillating fiber detectors, which could be pneumatically inserted into the storage region. Two detectors, both consisting of sets of vertical and horizontal fibers, were located at 180° and 270° with respect to the beam injection point (as shown in Figure 3.5). Each set consisted of 7 scintillating fibers, 0.5 mm in diameter, separated by 10 mm. For calibration purposes, the fiber harps could be rotated by 90° to expose all fibers to the same portion of the beam (Figure 3.6). The fiber detector measurement was destructive, i.e. some of the muons striking the fibers would multiple-scatter and be lost [35]. Therefore, the fiber monitors were inserted into the storage only during the

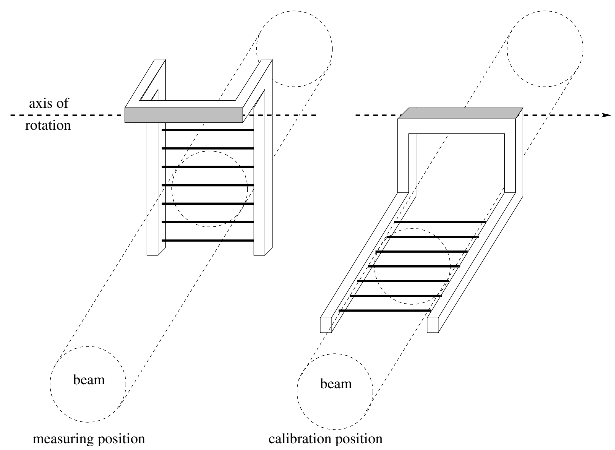

Figure 3.6: Scintillating fiber monitor.

runs dedicated to the studies of the beam dynamics.

3.7 Electron Detectors

The detector system for $(g-2)$ experiment consisted of 24 detector stations distributed around the inside of the storage ring at 15° intervals (see Figure 3.5). The task of the stations was to provide a high-quality determination of the time of arrival and the energy of decay positrons. Each station contained an electron calorimeter. In addition to this, some stations were equipped with either position sensitive detector or front scintillator detector, or both.

3.7.1 Electromagnetic Calorimeters

The calorimeters, made of 1 mm scintillator fibers embedded in lead, measured the energy and arrival time of the positrons. Each Pb/SciFi module was 22.5(width) $\times$ 14(height) $\times$ 15(depth) cm^3, had a radiation length of about 1 cm, and consisted of four separate parts (quadrants). The energy resolution of the calorimeters was better than $\sigma/E = 8.5\%$ for 2 GeV/c electrons [43].

The output light from each of the calorimeter quadrants was conducted to photomultiplier tubes (PMTs) via light-guides. A special PMT base [44] was designed to turn off the photomultipliers during the flash accompanying the beam injection. The bases could be turned back on stably in about 1 μs. The gate-on times for different detectors were chosen according to the amount of flash they experienced. During the 1999 experimental run, detectors 2 through 7, situated downstream from the injection point, were gated on at least after 24 μs following the injection, whereas detectors

16-24 could be gated on after about 4 μs. The rest of the detectors (1, 8-15) were gated on after 14 μs.

It was necessary to maintain the balance of the output signals from different calorimeter quadrants. The absolute energy calibration of the calorimeters was performed at the BNL test beam, and the relative calibration was preserved with the use of two systems, based on light-emitting diodes (LED) and a Nitrogen laser-illuminated fiber optic system respectively. These calibration systems were also used to monitor short-term time and gain stability of the response of the calorimeters. The PMT gain shifts due to slow gate-on effect during the 1999 run were less than 1%, and the early-to-late timing shifts over the first 200 μs were less than 20 ps.

3.7.2 Front Scintillator Detector (FSD)

The front scintillator detector system consisted of 5 radially oriented scintillator slabs, 9 mm thick, measuring 22×2.8 cm^2, placed on the positron entrance face of the calorimeter. Light from the scintillator was guided through light-guides to a PMT. The FSDs were used in studies of the lost muon distribution, vertical distribution of decay positrons, and for timing purposes.

For the 1999 run, FSDs were installed on detector stations 9, 16 through 19, and 21 through 23.

3.7.3 Position Sensitive Detector (PSD)

Position sensitive detectors were used to measure the vertical and horizontal coordinates of the entrance point of the electron into the calorimeter. The PSD is a scintillator tile-fiber hodoscope consisting of one vertical and one horizontal plane, with 20 and 32 elements respectively. The PSD tiles were placed in front of the FSD slabs. Each element was 7×8 mm^2 cross-sectional strip of plastic scintillator, either 22.5 cm (horizontal) or 13 cm (vertical) long [45].

PSD could be used for detecting minimum ionizing particles, such as electrons, muons and protons. In 1999, stations 17 through 21 had working PSD detectors.

3.8 Detector Electronics and the Data Acquisition System

Analog signals from the calorimeter PMTs provided both energy and time information.

Wave-form digitizer (WFD) digitized and stored analog input data at a rate of 200 MHz. The WFD is a digital oscilloscope, sampling the calorimeter voltage output throughout the data taking period. By using two WFD channels, operating 180 degrees out of phase, to sample the same trace, the sampling rate of 400 MHz (2.5 ns between the samples) was achieved. To align two sets of samples ("WFD phases"), a marker pulse was input to the WFD at the beginning of each data spill. The digitizers worked in zero-suppressed mode: the data were saved only if the input voltage exceeded an adjustable threshold ("hardware threshold"), in which case a set of (typically 8) WFD samples was written to memory.

For each calorimeter, the signals from 4 PMTs and their sum were also sent to CAMAC analog-to-digital (ADC) and time-to-digital converter (TDC) modules for calibration purposes.

The sum was also sent to a multi-hit TDC (MTDC), which provided additional timing information. The MTDC registered the time of the leading and trailing edges of the input logic pulses with 1.25 ns accuracy. The pulses input into the MTDC were "derandomized". A derandomizer module, specially designed for that purpose, unambiguously associated an asynchronous logic pulse with synchronous clock cycles by shifting its leading edge to the center of the proper clock pulse [34]. This minimized the errors in assigning times to pulses which fell near the clock time boundaries, thus ensuring that the MTDC timing information was independent of rate.

The data acquisition system was composed of 6 front-end VME crates, linked to an event-builder VME. The data were read out by the front-end crates after each AGS spill, and stored in local memory buffers. CAMAC data were read out by the event-builder after every AGS spill. After the last spill in each AGS cycle, the event-builder collected the data from the front-end buffers and concatenated the event to be written to a SCSI-mounted DLT tape drive.

About 55 μs before each spill, a signal was sent from the AGS that the beam was on its way, the "AGS pre-pulse". This triggered the WFD and MTDC modules to begin digitizing their input. After 1600 μs a stop signal was sent. This signal stopped the digitization and also triggered the front-ends to start their read-out sequence [47].

3.9 Data Production

The data were decoded and processed off-line using data production programs. In the production, the calorimeter WFD data were scanned for the positron pulses, which were then subjected to "reconstruction", i.e. fit to a predefined function, the average pulse shape, to obtain refined time and energy information. The calorimeter pulse information was subsequently saved in a database for every AGS spill, along with the data from other detectors, and further relevant information.

Two production algorithms were used to process the data collected during the 1999 run: (1) Fortran based `G2Off`, using standard CERN analysis and database packages, `PAW` [51] and `ADAMO` [52]; (2) C++ based `G2Too`, using `ROOT` (an object-oriented analysis package developed at CERN). Both programs used essentially the same pulse reconstruction algorithm, but completely differed in the implementation.

A schematic of the `G2Off` pulse reconstruction algorithm [48, 49, 50] is given in Figure 3.7. The reconstruction is done for a "WFD island": a continuous group

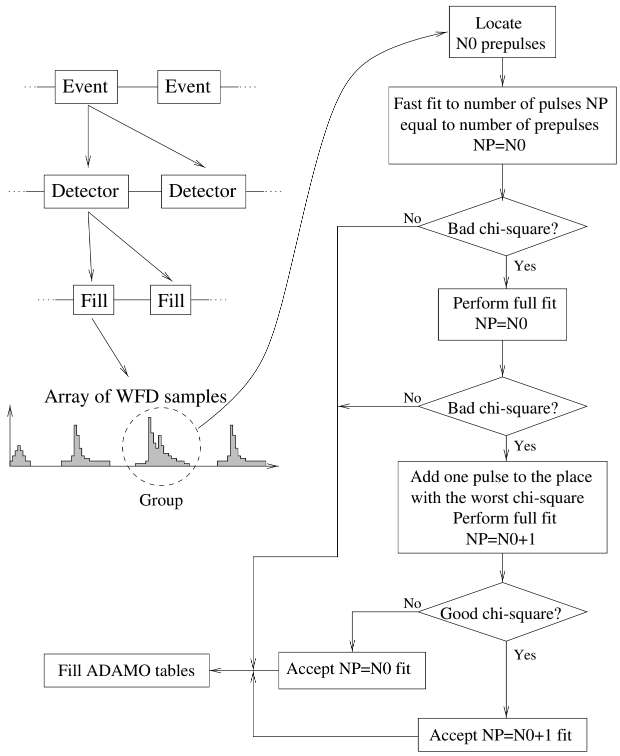

Figure 3.7: `G2Off` pulse-finding algorithm [50].

of WFD samples. At the first step the algorithm is looking for distinct peaks, or "pre-pulses", which exceed the programmable ("software") threshold. By definition, a pre-pulse starts with a jump in amplitude of at least 15 WFD counts sample-to-sample, and ends with an amplitude drop of at least 10 counts. If the time difference between two consecutive pre-pulses is greater than 60 ns, the island is split into two, with pulse-finding proceeding separately for these sub-islands. At the second step, a fast fit to the average pulse shape[1] is performed for all pre-pulses found on the island, while the pulse pedestal (WFD background) is assumed constant throughout the island.

If two or more positrons arrive at a detector within a short time, they may produce

[1]The average pulse shapes are constructed at the pre-production stage separately for each calorimeter and both WFD phases, using the WFD wave-forms [49].

overlapping pulses in the WFD data, so-called “pile-up”. The time separation of the pile-up pulses determines whether they can be resolved using the pulse-finding algorithm. The χ^2 of the preliminary fit is evaluated for the necessity of adding “hidden” pile-up pulses. If χ^2 is unacceptable, another fit is performed with an additional pulse, to account for the difference between the expected and the real WFD spectra. This technique is effective in resolving pile-up pulses separated by more than about 2.9 ns (the pulse-finding algorithm resolution time) [50].

Performance of the pulse-finding algorithm with respect to reconstruction of single, as well as pile-up pulses was studied in a simulation [50]. The minimum pulse resolution time was found to be within $(2.90 \pm .05)$ ns for all detectors (various average pulse shapes), independent of the time after injection, or pulse amplitude (for amplitudes over 50 WFD counts, or $\sim$ 1 GeV). Depending on the pulse amplitude, the precision of the pulse time reconstruction was found to vary from 100 ps for low-energy pulses to 20 ps for the pulses corresponding to positrons with $E > 2$ GeV. The average value of this time shift does not change early-to-late, therefore it does not affect the measurement of the $(g-2)$ frequency. (The overall early-to-late timing shift due to PMT instabilities was estimated from studies using the laser calibration system, and found to be smaller than 20 ps over the first 200 μs after the injection.)

The parameters of the pulses determined from fit are stored in the `ADAMO` tables, which are later converted into `PAW`-readable database files, called ntuples.

Chapter 4

First Results from the $(g-2)$ Experiment at BNL

4.1 First Experimental Run, 1997

The first dedicated $(g-2)$ run with pion injection took place from April through July 1997 [53].

The beam was delivered by the AGS in 8 bunches per cycle. The pions were selected with momentum 0.5% higher than the "magic" value. Using the threshold Čerenkov counter, situated at the end of the beam line, before the inflector, it was found that approximately 60% of the beam was π^+. About 25 ppm of the π^+ produced decay muons which were captured into stable orbits in the ring. The polarization of these stored muons was 97%. About 1,000 muons were stored per proton bunch.

The flash following injection induced background in the detectors. The intensity of the flash varied around the ring, and it was necessary to assign the time the calorimeters were gated on individually for each detector. The gate-on time varied between 12 and 120 μs. Data were accumulated for 8.8 muon lifetimes following injection.

In the off-line analysis, it was found that, in addition to positron pulses, the data contained narrow pulses ($<$ 8 ns total width), which were associated with γ-rays from neutron capture producing background near the photomultiplier tubes. This background could be distinguished from positron pulses on the basis of pulse shape and was reduced off-line to a negligible level.

A problem with misadjustment of the WFD minimum digitizing time, discovered off-line after the run was over, resulted in missing or under-sampling of input pulses that were over the set voltage threshold. This would happen if the pulses were not above the threshold for long enough time to trigger digitization. The effect of this inefficiency was not uniform throughout the data taking period, since the changing pedestal in the WFDs changed the effective thresholds for digitization, resulting in an increase of the average energy of fully digitized pulses during the spill. This caused

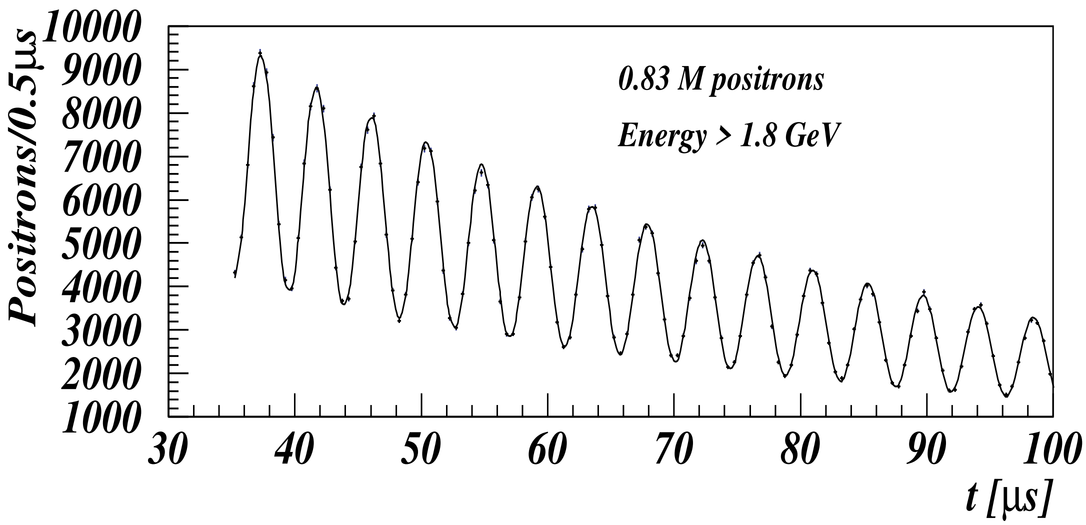

Figure 4.1: A sample of the 1997 data with 8-parameter fit function overlayed. The χ^2/DOF was 1.028 for 803 degrees of freedom [53].

the observed average decay asymmetry to increase with time as well, as higher energy decay positrons have higher asymmetry.

The decay positron data were fit by minimizing χ^2 to an 8-parameter function:

$$f(t) = N_0 \frac{e^{-(t/\gamma\tau_0)}}{(t-t_0)^\alpha}[1 + (A_1 t + A_2)\cdot\cos(\omega_a t + \phi)] + B, \tag{4.1}$$

where the observed decay asymmetry, $A = A_1 t + A_2$, increases with the time; B is a constant background term, and the parameters $t_0 = 5\mu$s (after injection) and α describe the time-dependent change in the effective energy threshold.

In total, 11.8 million positrons were obtained with energy greater than 1.8 GeV. Time histograms were filled for each detector, and different gate-on times. This made for 39 independent sets of data, analyzed separately, with the results in good agreement ($\chi^2 = 46$ for 39 degrees of freedom).

As in the CERN-III experiment, the value of the magnetic field was measured in terms of the free proton NMR frequency in water, ω_p. Including the corrections for muon vertical betatron motion (pitch correction) and the effects of electric dipole focusing field, the frequency ratio was found to be

$$\mathcal{R} = \omega_a/\omega_p = 3.707\ 220(47)(11) \times 10^{-3}, \tag{4.2}$$

where the first error is statistical, and the second is systematic. The sources of systematic errors are listed in Table 4.1.

Table 4.1: Systematic errors for the 1997 a_{μ^+} measurement [53].

Systematic effect	Error [ppm]
Magnetic field B	1.0
Muon distribution and $\langle B \rangle$	0.9
WFD time-dependent inefficiency	1.5
Muon losses	0.2
Timing shifts	0.1
Radial E field, pitch correction	0.05
Fitting start time	2.0
Binning effects	0.2
Total systematic error	2.9

The value of a_{μ^+} was obtained as

$$a_{\mu^+}(\mathrm{BNL}, 1997) = \frac{\mathcal{R}}{\lambda - \mathcal{R}} = 1\ 165\ 925(15) \times 10^{-9} \quad (13\ \mathrm{ppm}), \tag{4.3}$$

where $\lambda = \mu_\mu/\mu_p = 3.183\ 345\ 47(47)$ [54], and the errors are added in quadrature. This result agreed well with the mean of the CERN measurements for a_{μ^+} and a_{μ^-}, and the standard theory prediction.

4.2 Second Experimental Run, 1998

The second $(g-2)$ experimental run took place in the Summer of 1998 [55]. Important improvements were implemented since the first run. These included better stability and homogeneity of the storage ring magnetic field, improved stability of the positron detector system, and extended capacity of the data acquisition system. The muon kicker, commissioned in August 1997, allowed for the direct injection of muons into the storage ring.

For the second run, the AGS produced 6 bunches per cycle, separated by 33 ms. The muons with "magic" momentum were selected at a momentum slit, where the higher energy pions were directed into a beam dump. A measurement with a Čerenkov counter found that the beam consisted of equal parts of positrons, muons and pions. About 10,000 muons were stored in the ring per proton bunch. The number of detected positrons per hour was increased by an order of magnitude over the pion injection. At the same time, the injection related background (flash) was reduced by a factor of 50, since most pions were removed from the beam before entering the storage ring [55]. With the reduced flash, it was possible to begin counting decay positrons as early as 5 μs after injection in the region of the ring 270° around from

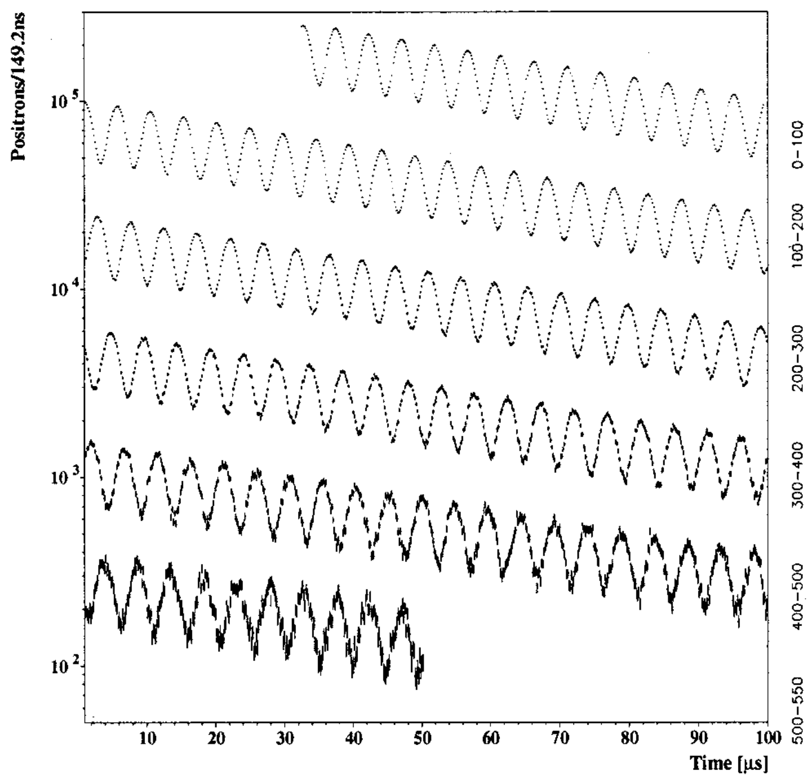

Figure 4.2: 1998 run: positron time spectra from all detectors added together ($E > 1.8$ GeV) [55].

the injection point, and 35 μs in the injection region. The data collection proceeded for 600 μs after injection.

The data collected by 21 detectors, 84 million decay positrons with $E > 1.8$ GeV in total, were used in the analysis of the anomalous precession frequency (Figure 4.2). The data sets from each detector were fitted separately to a 5-parameter function

$$f(t) = N_0 e^{-(t/\gamma\tau_0)}[1 + A\cos(\omega_a t + \phi)], \tag{4.4}$$

and the resulting values for ω_a were in good agreement (χ^2=17.2 for 20 degrees of freedom).

The data from the detectors, which were gated on early, were used in the fast rotation frequency (beam debunching) analysis, which allowed to obtain the equilibrium radius distribution of the stored muons (see Figure 4.3). The magnetic field seen by the muon distribution was calculated by tracking a sample of muons in software through the field map measured by NMR, and by averaging the field values.

Since the 1997 run, a substantial reduction in the overall systematic errors had been achieved. The field homogeneity had been improved by additional shimming. Additional thermal insulation of the magnet, and NMR feedback control to the main

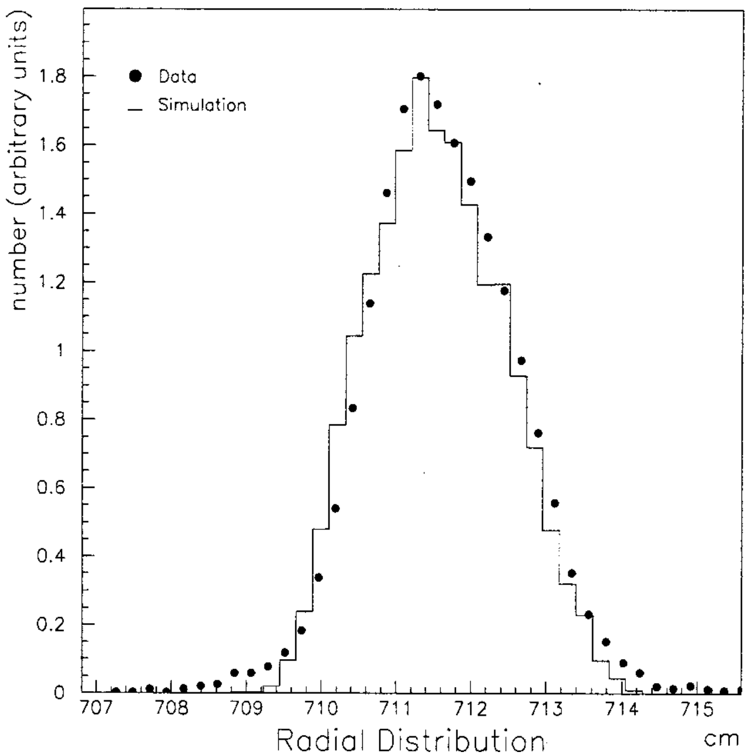

Figure 4.3: 1998 run: the equilibrium radius distribution calculated using the tracking code (histogram) and obtained from the analysis of the beam debunching (filled circles) [55].

magnet power supply improved the field stability. The field, averaged over the azimuth, was uniform to within ±4 ppm. The overall uncertainty in the $\langle B \rangle$ was 0.5 ppm. The errors associated with the determination of a_μ arose principally from pile-up (conservatively estimated at 0.6 ppm) and the AGS "flashlets" (0.5 ppm). Smaller errors came from the fitting procedure, timing shifts, detector gain changes, betatron oscillation, and from muon losses. Altogether, the systematic errors on ω_a and ω_p added in quadratures amounted to less than 1 ppm. The statistical error was close to 5 ppm.

The value of a_μ was found to be

$$a_\mu(\mathrm{BNL}, 1998) = 11\ 659\ 191(59) \times 10^{-10} \quad (5\ \mathrm{ppm}), \tag{4.5}$$

in good agreement with the 1997 result, the average of the CERN measurements, and the theoretical prediction.

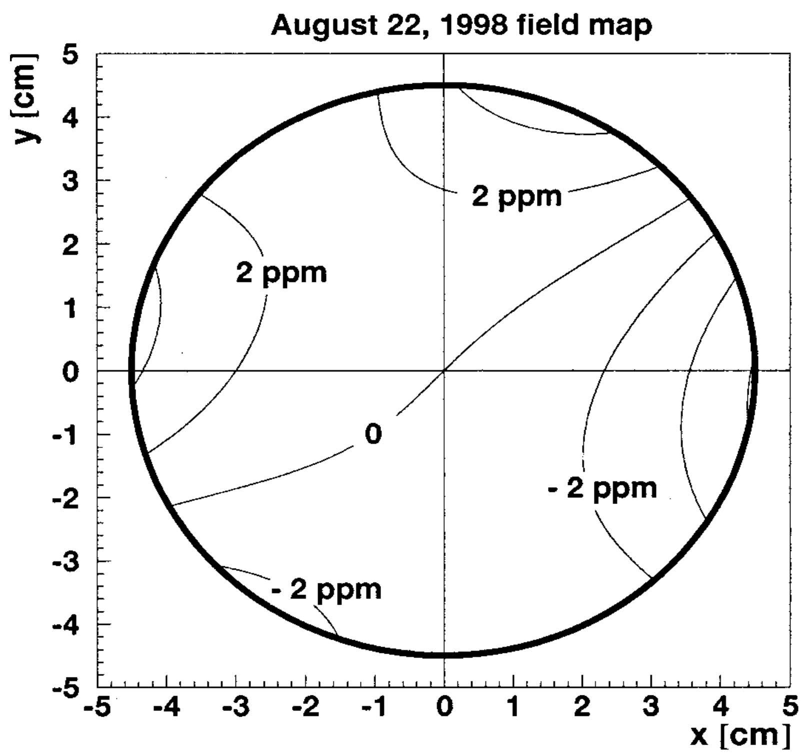

Figure 4.4: 1998 run: a magnetic field profile averaged over azimuth. The circle encloses the muon storage region of 4.5 cm radius. The contours represent 2 ppm changes in the field [55].

4.3 Third Experimental Run, 1999

The preparation for the third experimental run of the Brookhaven $(g-2)$ experiment began in December 1998, and the muon beam was first stored in the ring on New Year's eve of 1999. Most experimental aspects were the same as in the second run. As in 1998, muon injection into the ring was used. Compared to the previous run, better care was taken in tuning the AGS injection system, which minimized background from the out-of-time proton extraction ("flashlets"). For the first time, scintillating fiber monitors were used to measure the stored beam profile in a set of dedicated runs.

For most of the 1999 run, the proton beam from AGS was delivered to the target in six bunches, separated by 33 ms, per cycle of 2.5 seconds. The average proton beam intensity of 40 Tera-protons per cycle resulted in approximately 5×10^4 stored muons per cycle. This allowed a dramatic increase in the amount of the data collected: close to 2.9 billion decay positrons with energies greater than 1 GeV, almost 20 times as many as in two preceding runs combined.

The data were taken in separate runs, typically 30 minutes long, numbered between 3000 and 5720. The quality of data was monitored using a quick on-line analyzer program, which created a range of diagnostic histograms in the real time. Approximately every 8 hours of data taking, a dedicated laser run was taken, to monitor the calorimeter energy calibration and time stability.

The required adjustments to the beam line tune, calorimeter calibration, quadrupole scraping voltage etc. were completed by the beginning of the third week of running. For the data runs numbered after 3800, the running conditions were reasonably stable.

From January to early March 1999, there were 19 magnetic field measurements with the NMR trolley.

For the last two weeks of running in March 1999, the AGS switched into the 12-bunch mode. The data taken during this time (as well as in the first half of January) were not used in the analysis.

The analysis of the data taken during the third run, and the result of the measurement will be discussed in the following chapters.

Chapter 5

Analysis of the 1999 Data

As was mentioned in the previous chapter, the BNL experiment measures the ratio of the anomalous spin precession frequency, ω_a, and the free NMR frequency of protons in water, ω_p (which is a measure of the magnetic field seen by the muons). Consequently, there are two parts in the determination of a_μ.

Two independent analyses of the magnetic field data, and 4 analyses of the anomalous precession frequency were undertaken. This chapter contains a description of the analysis of ω_a done by the author, using the 1999 data set. An overview of the magnetic field analysis will be given as well.

5.1 Data Selection for the Analysis of ω_a

The data used in this analysis were produced with the `G2Off` pulse-reconstruction algorithm, as described in Section 3.9, and stored in the form of the standard `PAW` data structure, ntuples [51]. Separate ntuples were created for every data run and each detector. In the ntuples, the data were organized by the AGS spills, corresponding to a single-time beam injection into the $(g-2)$ storage ring. For each spill, the calorimeter pulse times, amplitudes and other fit parameters; as well as data from other detectors (FSD, quadrupole monitors, tØ counter etc.) and miscellaneous spill-relevant information were readily available.

Preliminary data run selection for the analysis of the anomalous precession frequency, ω_a, was done with the requirement of proper calorimeter energy calibration, and early-to-late time stability of the positron energy and decay time spectra. In addition to this, all runs known to have high AGS background ("flashlet") level, as well as the runs used for laser, LED, quadrupole or fiber harp studies were eliminated. In total, 806 data runs, numbered between 3813 and 5093, met the selection criteria. The data from calorimeter detectors 2 and 20 were not used, due to problems with read-out electronics and calibration respectively.

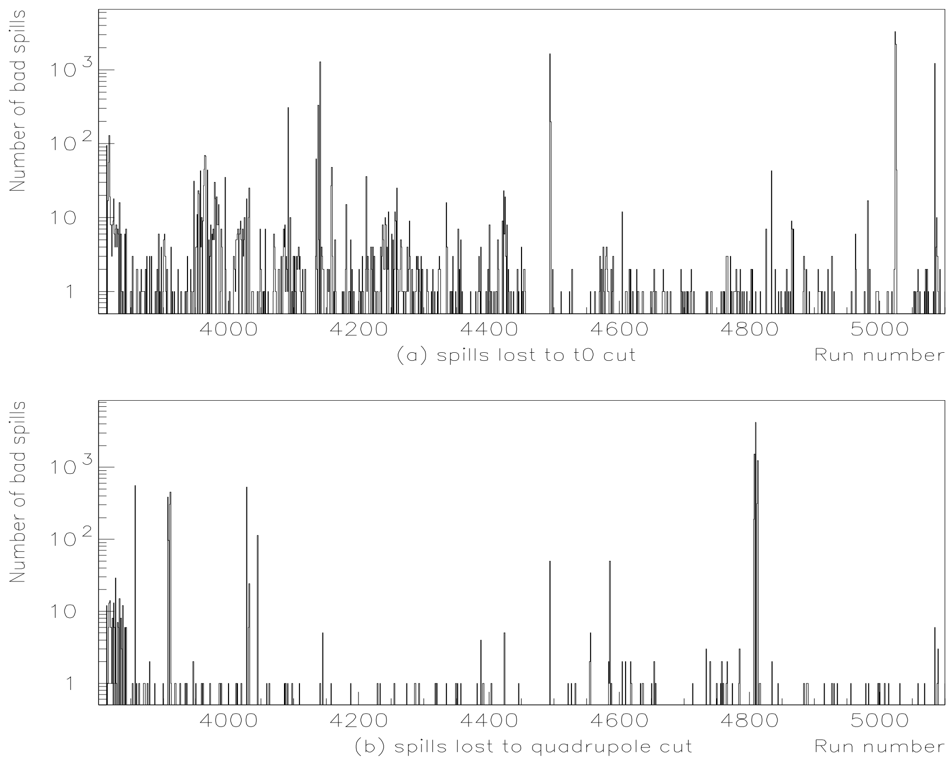

Figure 5.1: The number of spills eliminated due to (a) tØ pulse and (b) quadrupole trace quality problems vs the run number.

5.1.1 Cuts on Data Quality

Within the selected range of runs, every spill was evaluated in terms of the data quality. The data taken in a spill would be discarded if an electric quadrupole WFD trace for that spill was not read out due to hardware malfunctions, or there was an indication of a spontaneous electric discharge (quadrupole spark) such as a trace length shorter than 780 μs, or a significant (more than 10 WFD counts) difference in the quadrupole voltage readings taken at the beginning, in the middle, and at the end of the trace.

A mis-injection of the AGS proton bunch into the $(g-2)$ beamline in any of the 6 spills in the same cycle was known to inflict high background levels in the data taken throughout the entire cycle. An indication of mis-injection would be the absence, or a low amplitude, of the signal read out from the tØ counter which measured the time of the muon beam arrival at the inflector (injection time). A cut was introduced to eliminate such 6-spill cycles from the data selection.

Losses due to these cuts were: 1.6% of the total number of spills for the tØ quality

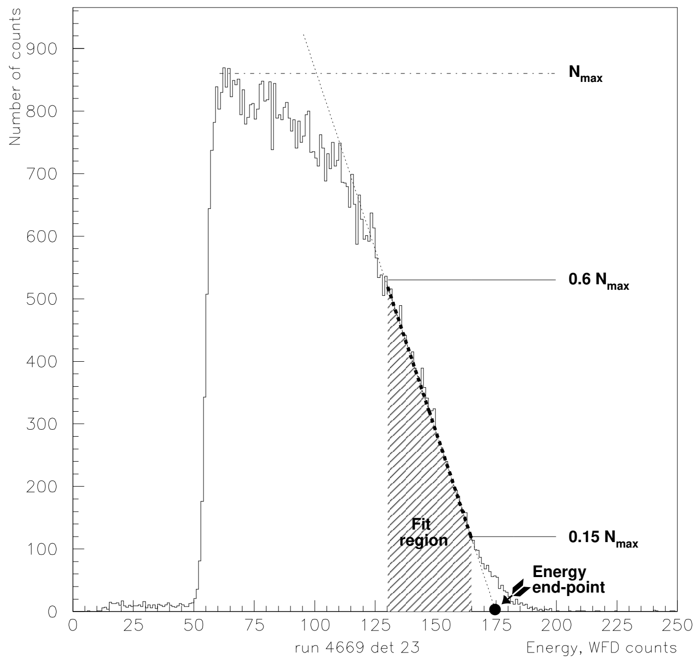

Figure 5.2: The positron pulse energy distribution for detector 23 in run 4669, for the time after 100 μs following the injection (the hardware threshold for the pulses was 50 WFD counts). A straight line fit to the linear part of the slope brings the energy end-point value of 175 WFD counts.

cut, and 0.4% for the quadrupole cut. A large fraction of spill losses was due to t∅ or quadrupole read-out problems in a small number of runs (see Figure 5.1). Overall, the data from approximately 2.7 million spills were selected for the analysis.

5.1.2 Detector Energy Calibration

The amplitude of a peak in the WFD data is proportional to the amount of energy deposited by a decay positron in a calorimeter. A typical distribution of WFD pulse amplitude values is shown in Figure 5.2. Due to the presence of pile-up pulses, the maximal pulse amplitude in the distribution is higher than the maximal decay positron energy of 3.1 GeV (close to the average muon energy).

For detector energy calibration, the same method was used as in the BNL 1998 analysis [56]. As was established with Monte-Carlo simulation, a good approximation of the maximal positron energy can be obtained by fitting the nearly linear part of the slope of the amplitude distribution to a straight line. The fit region is typically the section of the slope corresponding to the fall in the number density between about 60% and 15% of the distribution maximum. The crossing of the fit line with the x-axis is called the end-point of the energy distribution, and is assumed to correspond to the positron energy of 3.1 GeV. An example of determination of an end-point is given in Figure 5.2.

The end-points of the energy distribution were determined individually for every detector in each of the selected runs. The boundaries of the fit region were slightly adjusted for each detector due to differences in the shape of the energy spectrum. The energy spectra for end-point fitting were taken at late time (after 100 μs following the injection) in order to minimize the effects of pile-up and calorimeter PMT instabilities, mostly confined to the early times. The end-point values for each detector were then averaged over groups of runs, during which the calibration remained stable, as illustrated for detector 1 in Figure 5.3.

In the analysis, only the data from decay positrons with energies greater than the threshold energy of 2 GeV (64.5% of the end-point energy) were used. Throughout this dissertation, the expression “cut N GeV” is synonymous with “a selection of positrons with $E > N$ GeV”.

5.1.3 Correction for Energy Scale Changes

The detector energy scale changes (ESC) within a spill are caused by instabilities in the calorimeter photomultiplier tubes. As was mentioned in Section 3.7.1, the photomultipliers are turned off during the flash accompanying the beam injection. Due to slow turn-on of some tubes, the PMT gain turns out to depend on the time of the positron's arrival at the calorimeter, relative to the gating time. Such variation in the energy scale, if not corrected for, adversely affects the uniformity of the data selection, and, eventually, the consistency of the analysis results. It was estimated that linear ESC of 0.2% over a time period of 200 μs, would result in a systematic error of 0.1 ppm in ω_a [57]. Therefore it was important to maintain the stability of the effective energy threshold for the pulse selection.

Time-dependent ESC translate into the time-dependent variation in the average value of the energies of selected positrons. The average energy of the selection is also affected by the rate of pile-up, since the reconstructed energies of pile-up pulses are on average higher than those of the pure positron pulses. A method was developed by the author, allowing one to separate these two contributions to the energy average, using the time-dependence of the average positron energy for selections with different energy cuts.

For each of the 22 detectors, pulse energy spectra were constructed for different slices of time after the injection, with each slice covering one anomalous precession period ($T_a = 2\pi/\omega_a \simeq 4.365$ μs). Since the energy calibration changed from run to run for some detectors, pulse amplitudes were normalized to the end-point values in every run. The average energy of selected positrons was then calculated for each time

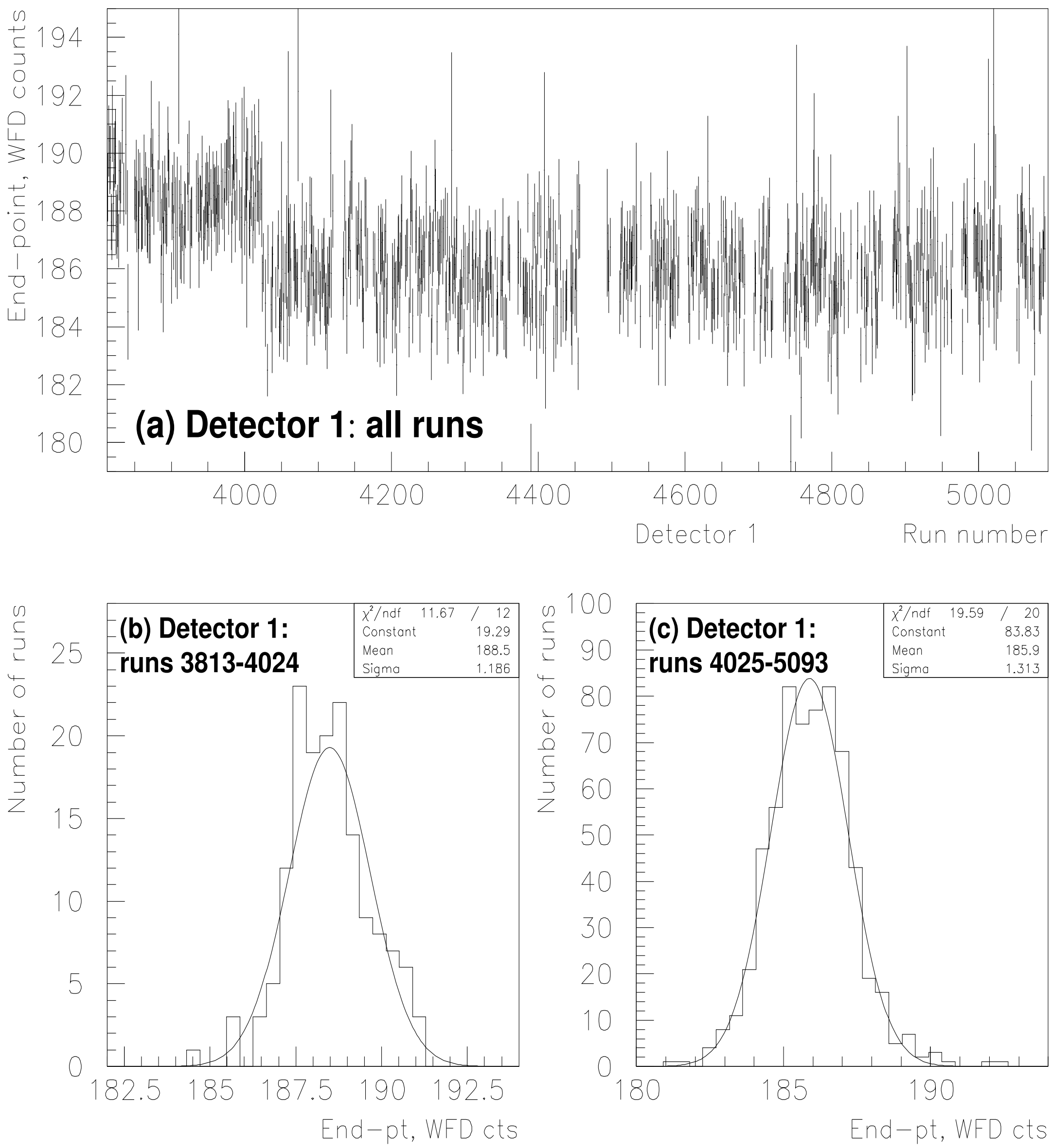

Figure 5.3: (a) The end-point values for detector 1 are shown with fit errors vs run number: a 2% change in the energy calibration was observed beginning with run 4025. The distribution of end-points has a gaussian form for two groups of runs: (b) before and (c) after the recalibration occurred.

slice, for the energy cuts of 60, 70, 80, 90 and 100% of the maximal positron energy ($E_{max} = 3.1$ GeV).

The effect of ESC is independent of the pulse energy: the scale change results merely in "stretching" or "contracting" of the distribution shape along the energy axis. Therefore, if no energy cut is applied, i.e. all pulses are taken into account, the relative variation in the average energy is the same as the change in the energy scale. If the average energy is calculated for pulses above a certain threshold, such variation will be smaller, since the number of selected pulses, i.e. the sample over which the energy is averaged, will be affected by the ESC as well. For example, if the PMT gain increases, not only the pulses originally above the threshold, but also the ones originally just below the threshold will be selected. Since the "extra" pulses have lower energies than the rest of the selection, the average energy of the distribution will not increase as much as it would if only the "original" pulses were selected[1].

The estimate of the sensitivity of the average energy to the ESC was obtained in a simulation, by applying artificial "gain" to the real data pulses, while holding the threshold energy unchanged. It was found that for the $0.6{\cdot}E_{max}$ cut, the change in the average energy of the positron selection reflected only approximately 48.7% of the energy scale change. This number decreased for higher energy cuts: 42.2% for the $0.7{\cdot}E_{max}$ cut, 34.6% for $0.8{\cdot}E_{max}$, 24.5% for $0.9{\cdot}E_{max}$, and only 2% for $E_{cut} = E_{max}$. Thus, the effect of the ESC on the average energy decreases as the threshold energy increases.

On the other hand, the relative fraction of pile-up pulses in the data, and therefore the strength of the variation of the average energy due to pile-up would be greater for higher thresholds. Thus, for the data selections with different energy thresholds, the relative size of the ESC and pile-up contributions to the variation in the average energy will vary as well.

This is illustrated in Figure 5.4 for detector 1: for the cuts 0.6 and $0.8{\cdot}E_{max}$, the variation in the average energy is dominated by the characteristic bell-shaped ESC due to slow PMT turn-on, whereas for the cut $0.9{\cdot}E_{max}$, the change in the average energy is mainly affected by the exponentially decreasing contribution from pile-up pulses.

Assume a simple model of the change in the average energy with the time:

$$\mathcal{E}(t) \simeq [\mathcal{E}_{LT} + \mathcal{E}_p \cdot n_{p0} \cdot f_p(t)] \cdot [1 + a \cdot f_{ESC}(t)] \tag{5.1}$$

where the "late time" average, $\mathcal{E}_{LT}$, is determined from the data taken after 200 μs following the injection (at which time the effect of pile-up and ESC is minimal), $\mathcal{E}_p$ is the average energy of the pile-up pulses, n_{p0} is the fraction of pile-up pulses in the data sample at $t = 0$, $f_p(t)$ describes the decrease with time in the relative number of pile-up pulses with respect to the total number of pulses in the data, a is the sensitivity of the average energy to the ESC (determined from simulation as

[1] That is, if the energy threshold were adjusted to reflect the ESC.

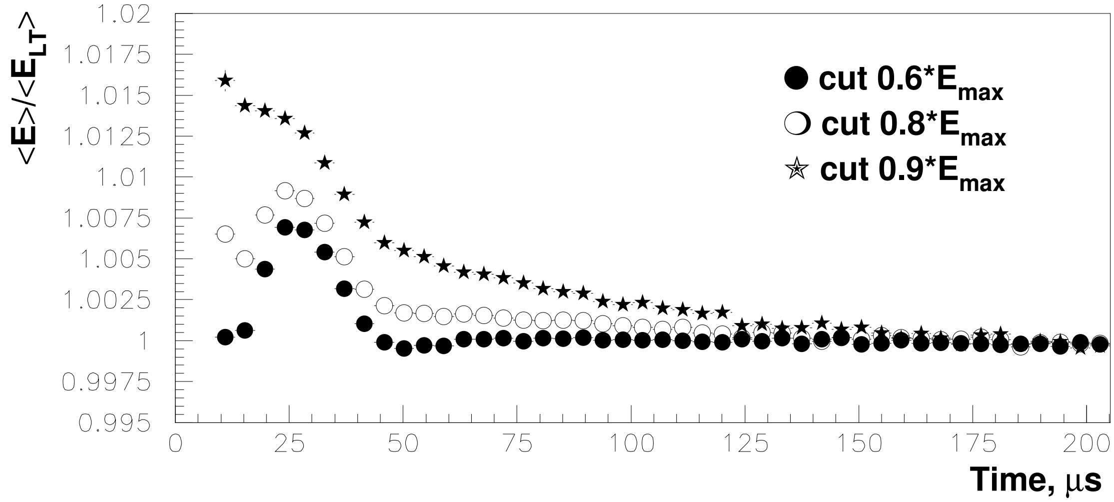

Figure 5.4: Normalized average energy of the positron pulses recorded by detector 1 shown as a function of time after the injection for different energy cuts. Averaging was done over the anomalous precession period and the result was then normalized to the late time (after 200 μs) average.

described above), and $f_{ESC}(t)$ is a function describing the ESC.

The parameter $\mathcal{A}_p(E_{cut}) = n_{p0}(E_{cut}) \cdot \frac{\mathcal{E}_p(E_{cut})}{\mathcal{E}_{LT}(E_{cut})}$ describes the normalized pile-up contribution to the average energy at $t = 0$. $\mathcal{A}_p$ is independent of the time, but obviously varies for different cuts. For two different energy cuts, E_1 and E_2, the equation 5.1 can be rewritten as:

$$\mathcal{E}_{norm}(E_1, t) = \frac{\mathcal{E}(t, E_1)}{\mathcal{E}_{LT}} = [1 + \mathcal{A}_p(E_1) \cdot f_p(t)] \cdot [1 + a(E_1) \cdot f_{ESC}(t)], \tag{5.2}$$

$$\mathcal{E}_{norm}(E_2, t) = \frac{\mathcal{E}(t, E_2)}{\mathcal{E}_{LT}} = [1 + \mathcal{A}_p(E_2) \cdot f_p(t)] \cdot [1 + a(E_2) \cdot f_{ESC}(t)]. \tag{5.3}$$

From studies using the laser calibration system, it was found that the energy scale changes are negligible after 50 μs in most detectors. This permits one to neglect the term $(1 + a \cdot f_{ESC})$ when describing the variation in the average energy at late times. With the assumption that the pile-up time behaviour is cut-independent, the relative strength of the pile-up contributions to the average energy for selections with different cuts:

$$\mathcal{B}(E_1, E_2) = \frac{\mathcal{A}_p(E_1)}{\mathcal{A}_p(E_2)} \simeq \frac{\mathcal{E}_{norm}(E_1) - 1}{\mathcal{E}_{norm}(E_2) - 1}, \tag{5.4}$$

can be obtained from the average energy data, taken after 50 μs following the injec-

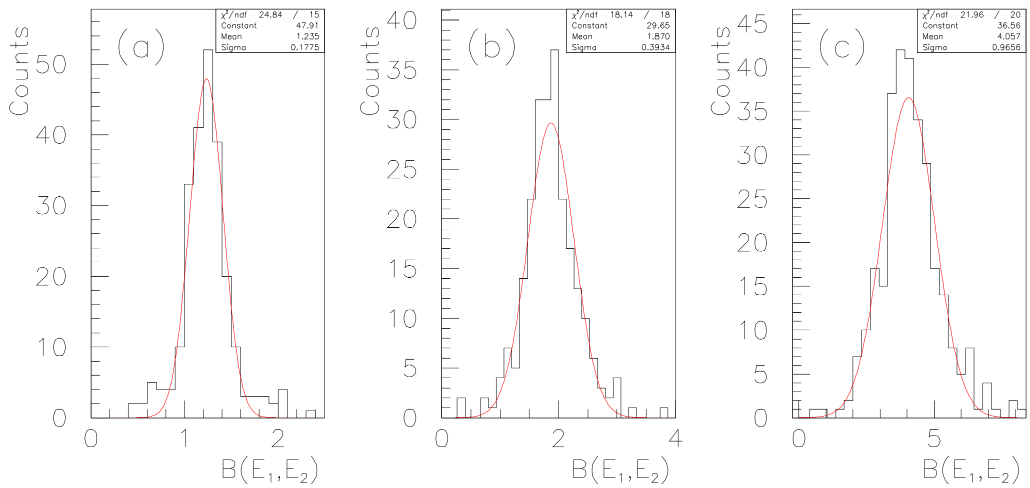

Figure 5.5: The distribution of the values $\mathcal{B}(E_1, E_2)$ (See Eqn. 5.4) for different combinations of the energy cuts, with fit to a gaussian function: (a) for the cuts $0.6 \cdot E_{max}$ and $0.7 \cdot E_{max}$, (b) for the cuts $0.6 \cdot E_{max}$ and $0.8 \cdot E_{max}$, and (c) for the cuts $0.6 \cdot E_{max}$ and $0.9 \cdot E_{max}$

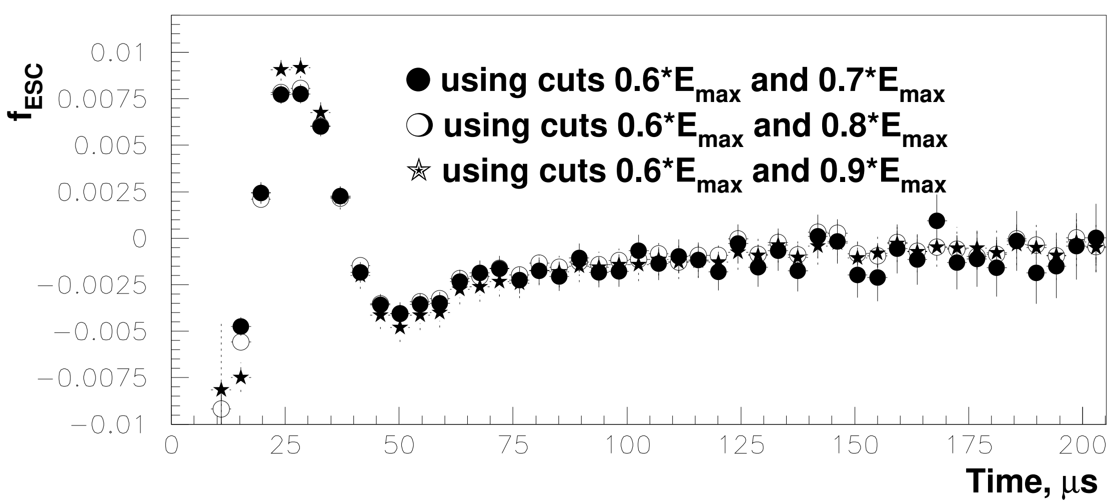

Figure 5.6: Energy scale change vs time for detector 1: the results obtained using 3 different combinations of energy cuts are in good agreement.

tion, for different combinations of the energy cuts (see Figure 5.5).

If $\mathcal{B}(E_1, E_2)$ is known, A_p can be eliminated from a pair of Equations 5.2, 5.3, describing the results for two different cuts. Neglecting the small term $\mathcal{A}_p \cdot f_p \cdot a \cdot f_{ESC}$, one obtains a function describing the energy scale change:

$$f_{ESC}(t) \simeq \frac{\mathcal{E}_{norm}(E_2, t) \cdot \mathcal{B}(E_1, E_2) - \mathcal{E}_{norm}(E_1, t) - [\mathcal{B}(E_1, E_2) - 1]}{a(E_2) \cdot \mathcal{B}(E_1, E_2) - a(E_1)} \tag{5.5}$$

Equation 5.5 was used to determine ESC for different detectors and different combinations of cuts. The results obtained using different combinations of cuts for the same detector agreed within errors (Figure 5.6).

For most detectors, the evolution of the energy scale changes with the time could be described as an exponentially decreasing function, except in the case of detectors 1 and 4, which required an additional gaussian-like term (namely $c_2 \neq 0$):

$$f_{ESC}(t) = c_1 \cdot e^{-\frac{t}{\tau}} + c_2 \cdot e^{-\frac{1}{2}(\frac{t-t_0}{\sigma})^2} \tag{5.6}$$

Only 6 detectors were found to experience changes in the energy scale of the order of 0.1% or higher at 30 μs, as shown in Figure 5.7. In the selection of data from these detectors, a time-variable threshold was used of the form:

$$E(t) = (1 + f_{ESC}(t)) \cdot E_{th}, \tag{5.7}$$

where E_{th} is the nominal energy threshold, and $f_{ESC}(t)$ is given by Eqn. 5.6.

After f_{ESC} is determined, the pile-up contribution to the average energy can be obtained from Equation 5.2 as:

$$\mathcal{P}(E, t) = \frac{\mathcal{E}_{norm}(E)}{1 + a(E) \cdot f_{ESC}(t)} = 1 + \mathcal{A}_p(E) \cdot f_p(t). \tag{5.8}$$

This can be used to study the time-dependence of the pile-up intensity.

5.1.4 Data Histograms

The histograms of the decay time data were created using `PAW`. Each histogram had 5000 bins, with a bin width of 149.185 ns, close to the cyclotron period, to minimize the effects of beam bunching. For the same purpose, the injection time for each spill was randomized within the cyclotron period[2] (using the pseudo-random number generator `RANMAR` [58]).

To compensate for differences in the cable lengths and other constant timing offsets between different detectors, detector phases were aligned within ± 2 ns (at 50 μs after

[2]Simulations showed that this procedure minimized the systematic error due to the beam bunching.

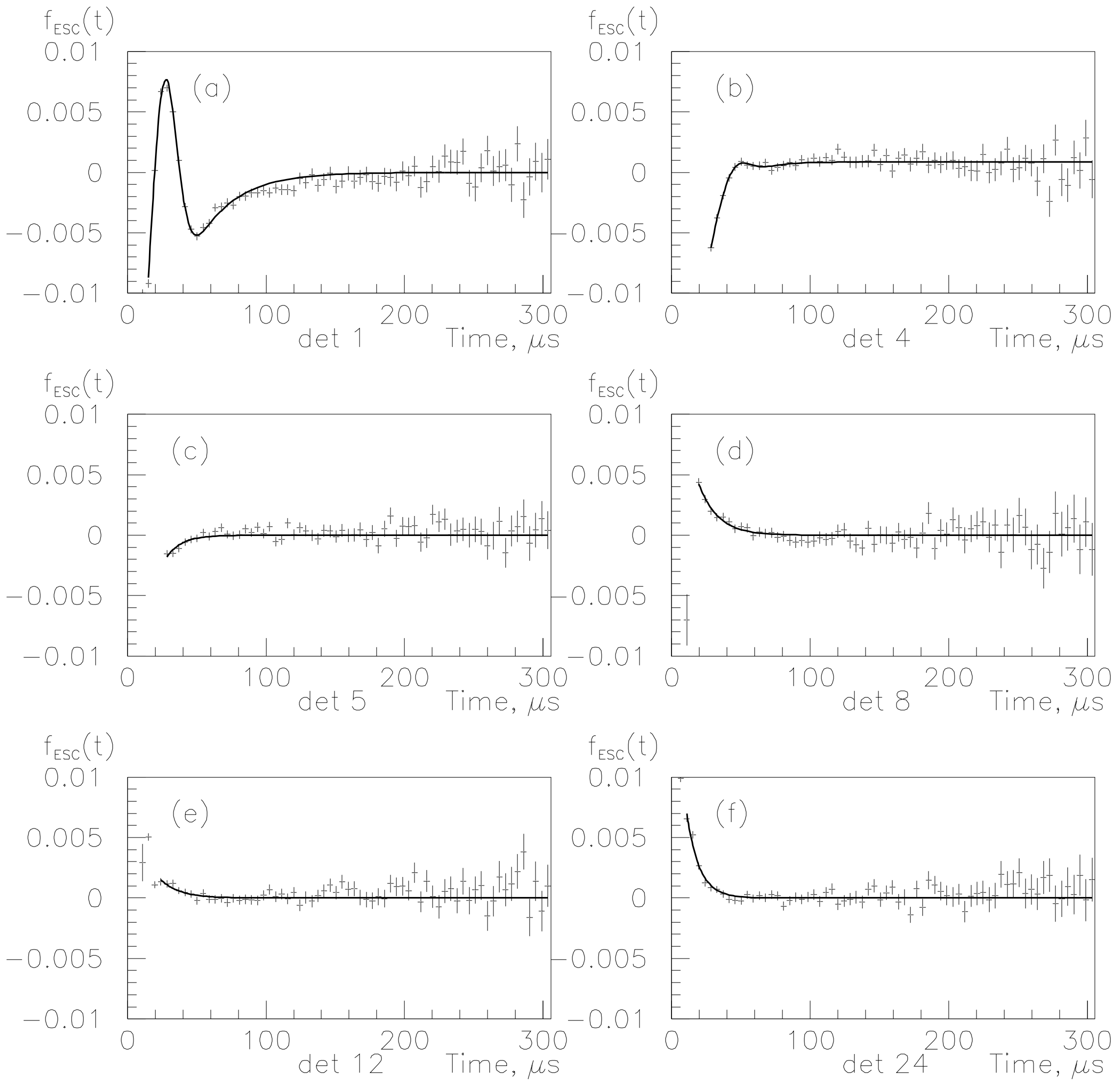

Figure 5.7: Relative energy scale change shown as a function of time after the injection for detectors (a) 1, (b) 4, (c) 5, (d) 8, (e) 12 and (f) 24. The data for each detector is overlayed with fit to the function given by Eqn. 5.6.

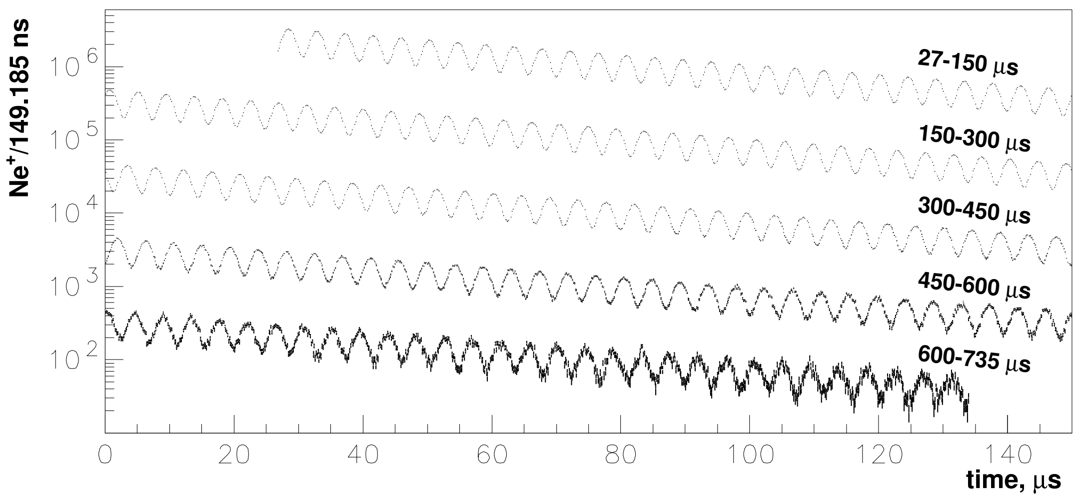

Figure 5.8: Time distribution of decay positrons (number of decays per cyclotron period) for the energy cut 2 GeV. The muon lifetime in the laboratory is close to 64.4 μs due to time dilation. The events from the time range 32-600 μs after the injection were used in the analysis.

the injection) after these phases were determined from a preliminary fit. In other words, each detector was assigned a different time offset with respect to the injection time. These offsets were calculated with respect to detector 16, and varied between -3.4 ns (det. 21) and 17.7 ns (det. 5).

A total of 949 million events ($E > 2$ GeV), recorded by 22 detectors between 32 and 600 μs after the injection, were used in the analysis. The time spectrum of decay positrons for the energy cut 2 GeV is shown in Fig. 5.8.

5.2 Modifications in the Fitting Function

The function describing the number of decay positrons vs time is:

$$n(E,t) = N_0(E) \cdot e^{-t/\gamma\tau_0} \cdot [1 + A(E) \cdot \cos(\omega_a t + \phi(E))], \tag{5.9}$$

where the normalization constant (N_0), decay asymmetry (A), and the phase (ϕ) depend on the energy threshold (E) used in the selection of positrons; and $\gamma\tau_0$ is the dilated muon lifetime. Throughout this chapter, the function described by Eqn. 5.9 will be referred to as the "5-parameter function".

While the decay positron data collected during the 1998 run could be adequately described by the 5-parameter function, the 15-fold increase in statistics, combined with a higher data taking rate in 1999, required more careful consideration of pile-up, betatron oscillation, and muon losses.

5.2.1 Pile-up

Generally, two calorimeter pulses can be resolved if their time separation is greater than about 2.9 ns (see Section 3.9). Overlap of the pulses within the resolution time (pile-up) causes distortion in the reconstructed time and energy spectra.

If two original positron pulses fall within the resolution time, they are reconstructed as a single pile-up pulse. Therefore, two (original) events are always lost in pile-up and one (reconstructed) is gained. The term "negative" pile-up will be used for the lost events, and "positive" pile-up for the gained ones. The amplitude of the reconstructed pile-up pulse is approximately equal to the sum of the amplitudes of the two original pulses, therefore pile-up results in an excess number of the registered high-energy positrons, whereas the losses occur in the lower part of the energy spectrum (see Figure 5.11).

Since both the phase and asymmetry of decay positrons depend on the energy, the phase and asymmetry of pile-up pulses differ from those of the rest of the distribution [59]. The probability to have a pile-up event, i.e. two pulses falling within the resolution time window, is proportional to the instantaneous decay rate (given by Equation 5.9) squared and to the minimum resolution time of the reconstruction algorithm. Due to this, the number of pile-up pulses dies out with the decay time (τ) approximately equal to a half of the dilated muon lifetime: $\tau = \gamma\tau_0/2$. As was confirmed by simulation and other studies, the probability of the pulse pile-up is also enhanced at early time due to beam bunching [60, 61]. In the 1999 data, pile-up pulses accounted for about 1% of all decay positron events.

The net change in the number of registered positron counts is the difference between the number of "positive" and "negative" pile-up events. The additive pile-up correction to the 5-parameter function can be described by a function of the form:

$$p(t) = N_0 e^{-t/\tau} \cdot [n_p + A_p \cdot \cos(\omega_a t + \phi + \Delta\phi_p)] \cdot [1 + a_p e^{-\frac{1}{2}(t/\tau_p)^2}], \tag{5.10}$$

where N_0, ϕ and ω_a are same as in Eqn. 5.9, $\tau = \gamma\tau_0/2$ is the lifetime of pile-up, n_p is a normalization constant related to the fraction of pile-up pulses in the data, and A_p is the pile-up asymmetry; a_p and τ_p are respectively the amplitude and the characteristic decay time of the pile-up enhancement at early times due to the bunched structure of the beam. We will refer to the difference between the phase of pile-up distribution and the $(g-2)$ phase as the "pile-up phase", $\Delta\phi_p$.

A new technique was developed, allowing one to construct pile-up pulses using well-resolved pairs of pulses from the data. This technique is illustrated in Figure 5.9: a candidate pair consisted of a "trigger" pulse, S_1, and a "shadow" pulse, S_2, registered within a time window of the width, $\Delta = 2.9$ ns, equal to the minimal resolution time of the reconstruction algorithm. The time window was offset from the

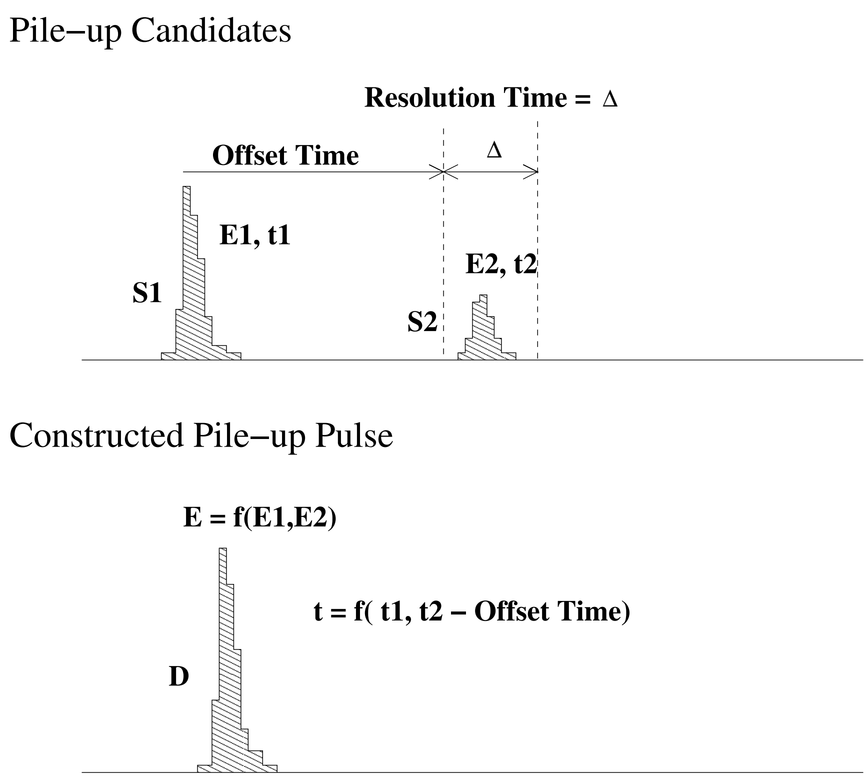

Figure 5.9: Pile-up construction.

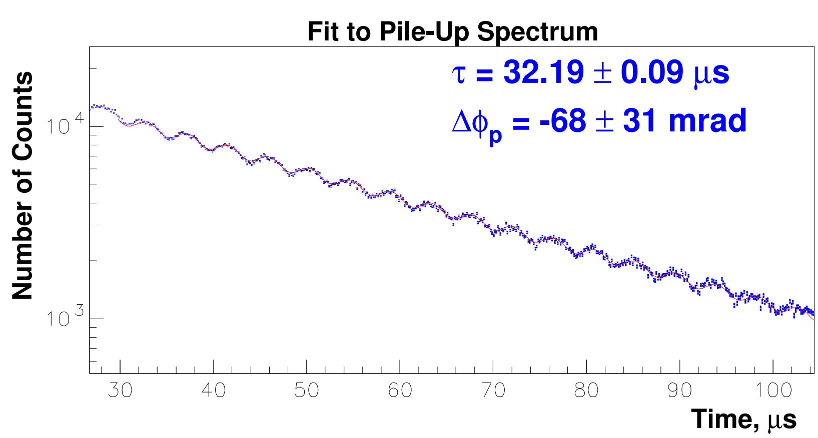

Figure 5.10: Time spectrum of constructed pile-up, overlayed with fit function given by Eqn. 5.10.

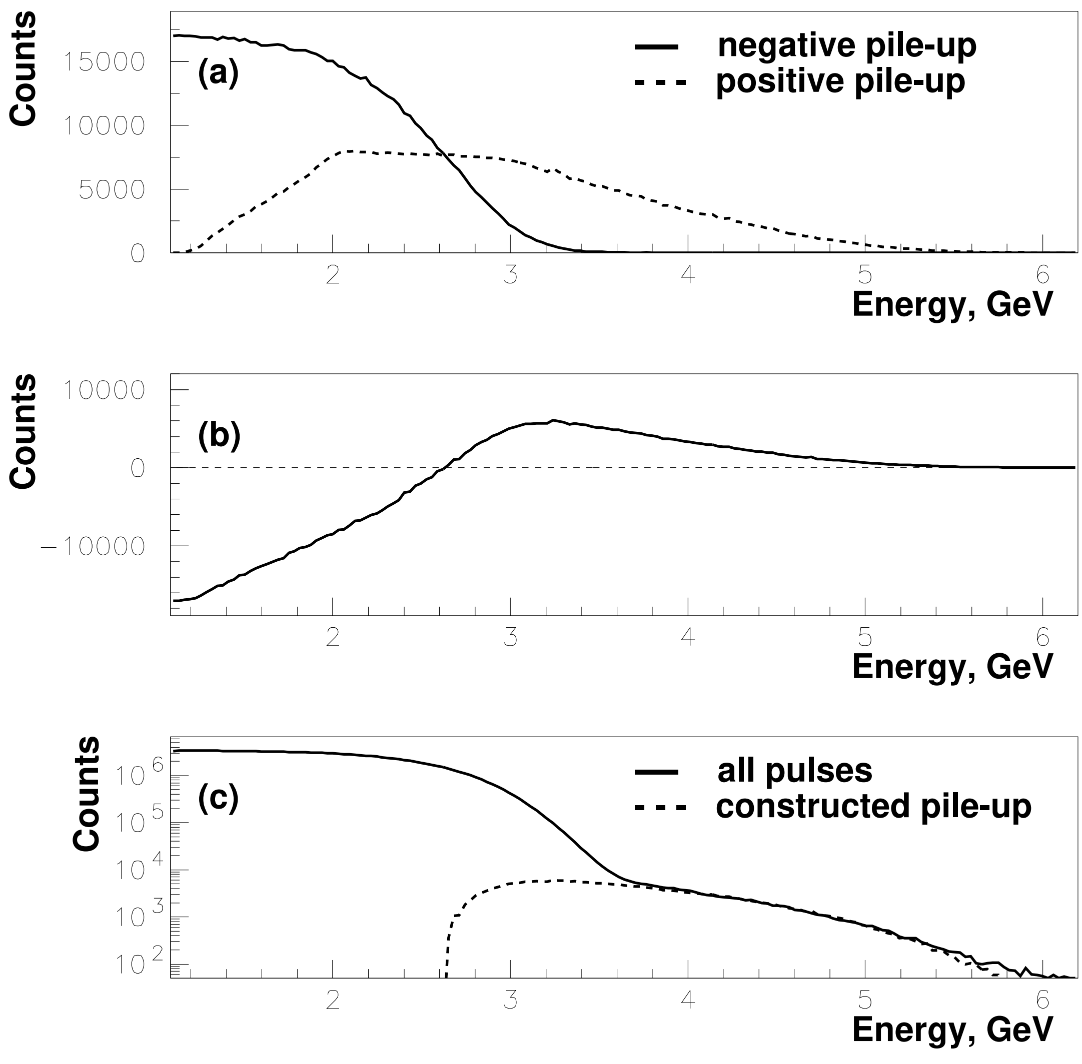

Figure 5.11: Constructed pile-up: (a) energy distribution of the "positive" and "negative" pile-up events; (b) net change in the number of registered pulses due to pile-up vs pulse energy; (c) energy distributions of all pulses and constructed pile-up pulses compared.

trigger pulse by $t_{offset} = 10$ ns. The time and energy of a "positive" pile-up pulse, D, were then constructed as if the pulses S_1 and S_2 overlapped within the resolution time:

$$E(D) = f_\Sigma \cdot [E(S_1) + E(S_2)], \tag{5.11}$$

$$t(D) = \frac{t(S_1) \cdot E(S_1) + [t(S_2) - t_{offset}] \cdot E(S_2)}{E(S_1) + E(S_2)}, \tag{5.12}$$

where the energy summation factor, $f_\Sigma = 0.96$, was estimated from the studies of the pulse reconstruction algorithm. Since the offset time was chosen much smaller than the period of the spin precession ($\sim 4.36\mu$s), the error resulting from shifting the time of the pulse S_2 by t_{offset} in Eqn. 5.12 is negligible. The procedure is described in detail in Ref. [62].

The time spectrum obtained in such manner can be fit to the function given by Eqn. 5.10 to get a good estimate of the pile-up parameters (see Figure 5.10); or it can be subtracted from the data set altogether, to give an approximation of a "pile-up-free" sample.

Since the hardware (WFD) energy threshold was set at close to 1 GeV for all detectors, no "trigger" pulses of $E(S_1) < 1$ GeV were present in the data, i.e. no information was available from pairs of pulses, if both of them were below the threshold. This resulted in the undercounting of the "positive" pile-up pulses with energies $E(D) < 2$ GeV (see Eqn. 5.11)[3]. In other words, a *complete* "positive" pile-up spectrum could be constructed only for the pulse energies of higher than twice the hardware threshold, or $E > 2$ GeV. Therefore, the pulses were selected for the ω_a analysis with the energy threshold of 2 GeV as well.

The statistical error for the ω_a measurement, given by Eqn. 2.15, is minimized for the positron selection with the 1.8 GeV energy cut[4]. The choice of the 2 GeV cut resulted in a loss of about 1% in the statistical power, which was more than compensated for by the reduction in the systematic error due to the uncertainty in the pile-up phase. For the cut 2 GeV, the pile-up phase was determined from a fit to constructed pile-up: $\Delta\phi_p = -68 \pm 31$ mrad.

The enhancement of pile-up due to fast rotation was studied using the average positron energy data. After the time-dependence of the energy scale changes is determined, as described in Section 5.1.3, the pile-up contribution to the change in the average energy, can be obtained as (Eqn. 5.8):

$$\mathcal{P}(t) = 1 + \mathcal{A}_p \cdot f_p(t). \tag{5.13}$$

[3]Obviously, the pulses with $E(D) < 2$ GeV could be constructed from pairs with $E(S_1) > 1$ GeV and $E(S_2) < 1$ GeV, but not from pairs with both $E(S_1) < 1$ GeV and $E(S_2) < 1$ GeV.

[4]If all events are weighted equally. Studies showed that further reduction in the statistical error may be achieved if the events are weighted according to the positron asymmetries (which depend on the positron energies) [63].

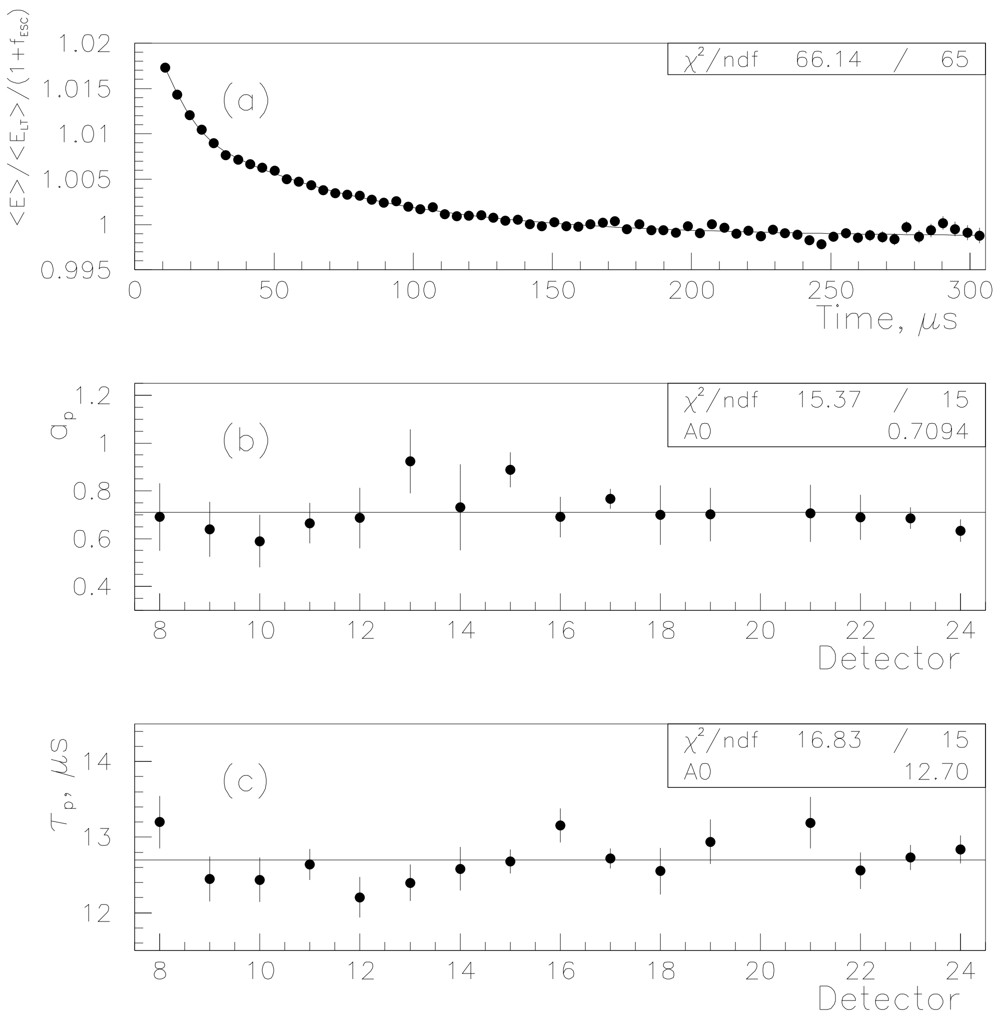

Figure 5.12: (a) Average energy for detector 24 vs time, corrected for ESC and normalized to the late time average, with fit to the function given by Eqns. 5.13, 5.14 overlayed; fit results for the parameters of pile-up enhancement due to fast rotation: (b) a_p and (c) τ_p for different detectors are in good agreement.

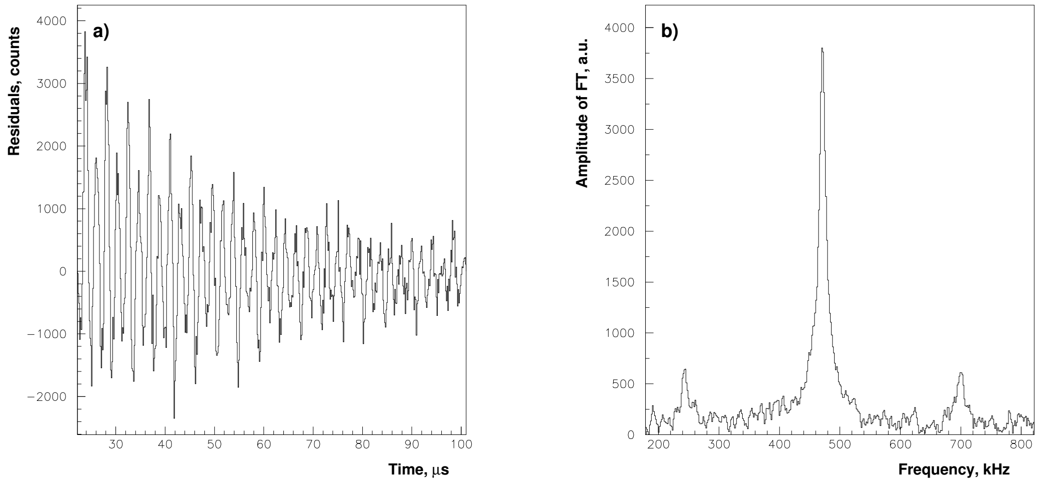

Figure 5.13: a) Coherent betatron oscillations were observed in the residuals of the 5-parameter fit; b) Fourier analysis of the residuals of the 5-parameter fit shows a large peak corresponding to coherent betatron oscillation frequency; two smaller peaks on each side come from the beating of the CBO and $(g-2)$ frequencies.

The function $f_p(t)$ describes the change in the fraction of pile-up pulses in the data:

$$f_p(t) = \frac{p(t)}{n(t)} \approx n_p \cdot e^{-t/\gamma\tau_0} \cdot [1 + a_p e^{-\frac{1}{2}(t/\tau_p)^2}], \tag{5.14}$$

where $p(t)$ is the pile-up function (Eqn. 5.10), $n(t)$ is the 5-parameter function (Eqn. 5.9). Since the average energy is calculated over the anomalous precession period, $T_a = 2\pi/\omega_a$, neglecting the terms including $\cos(\omega_a t + \phi)$ is justified.

The average energy data from detectors 8-24, corrected for ESC, was fit to the function given by Equation 5.13. Detectors 8-24 were chosen because they gated on relatively early, which allowed for better fitting to the short-lived fast rotation correction to the pile-up intensity. The parameters of the pile-up enhancement were found to be: $a_p = 0.71 \pm 0.04$ and $\tau_p = 12.7 \pm 0.3$ μs (see Figure 5.12).

5.2.2 Coherent Betatron Oscillation

Since the aperture of the inflector is smaller than that of the storage ring, the stored muon phase space is not filled out uniformly. This, combined with a non-ideal kick, causes betatron oscillation of the average position of the stored muon distribution as a whole. This effect was observed in the data from scintillator fiber detectors.

As the radial acceptances of the calorimeter detectors are not flat, such coherent betatron oscillation (CBO) affects the time distribution of decay positrons detected by the calorimeters. The most pronounced effect on the data due to CBO was the modulation of the recorded positron time spectra, caused by the change in the average radial position of the beam. Since in a detector's frame of reference, the motion of the beam bunch is a superposition of the cyclotron and the betatron motions, the frequency of the modulation in the data is equal to the difference between the cyclotron and radial betatron oscillation frequencies.

For the cyclotron frequency, $f_c \simeq 6.7$ MHz, and the radial betatron frequency, given by Eqn. 3.2 ($f_r = \sqrt{1-n} \cdot f_c$), with the weak focusing field index, $n \simeq 0.135$, the modulation frequency was:

$$f_B = \omega_B/2\pi = f_c - f_r = f_c\big(1 - \sqrt{1-n}\,\big) \simeq 470.5\,\mathrm{kHz}. \tag{5.15}$$

As illustrated in Figure 5.13, this frequency could be easily seen in the results of a Fourier analysis (using fast Fourier transform algorithm [64]) of the residuals of the fit to the 5-parameter function given by Eqn. 5.9. The amplitude of this effect died out with time as a gaussian packet [65], with a characteristic decay time about 10 times longer than that of the fast rotation.

Based on the results of the studies of the CBO packet, the following form of the multiplicative correction to the decay rate was used:

$$b(t) = 1 + A_B \cdot \cos(2\pi f_B t + \phi_B) \cdot e^{-(t/\tau_B)^2}. \tag{5.16}$$

In Eqn. 5.16, A_B, f_B, ϕ_B and τ_B refer to the amplitude, frequency, phase and characteristic decay time of CBO.

The amplitude and the phase of CBO differed for detectors around the ring (see Figure 5.20). Detectors 7, 8 and 9, situated next to the kicker modules were more significantly affected, since the decay positrons were more likely to lose energy to showering in the kicker plates when the beam moved closer to the inner edge of the storage region.

The phases of CBO observed by the detectors varied over a range of 2π radians around the ring. As a result, the rate modulation in the data due to CBO is reduced by a factor of 3, if the data from all detectors are added together.

No correction for the vertical betatron oscillation was included in the fitting function, but its systematic effect on the observed positron time spectrum was taken into account.

5.2.3 Muon Losses

The loss of muons other than by decay causes the decay rate to decrease with time. This results in an excess of the registered decay positrons at early times. The muon losses can be minimized using controlled scraping (see Section 3.4.3).

The time-dependence of muon losses was studied using coincident signals in two

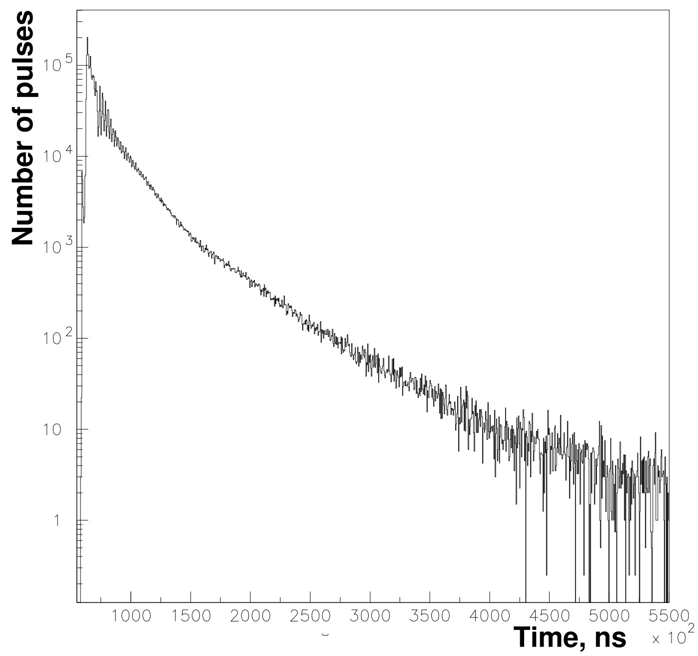

Figure 5.14: Number of FSD three-fold coincidences as a function of time [66].

or three adjacent front scintillator detectors situated in front of the calorimeters. Special cuts on the pulse time separation were designed to eliminate the accidental coincidences. The use of three-fold coincidences further minimizes the number of accidentals [66]. This method, however, does not allow one to distinguish between the data from lost muons and protons, since the two produce similar pulses in the FSD. A sample time distribution of the lost particles from the FSD data is shown in Figure 5.14.

An approximation of the time spectrum of muon losses can be extracted directly from the decay positron data by performing a fit to data beyond 100 μs after the injection, at which point these losses are at a very low level, and then extrapolating the fitted function back to earlier times[5]. The ratio of the decay spectrum to the value of the "late-time" fit function shows a significant excess of counts at early times (see Figure 5.15).

Two forms of multiplicative correction to the decay rate were used:

$$l(t) = 1 + a_{\mu L} \cdot e^{-\frac{1}{2}(t/\tau_{\mu L})^2}, \tag{5.17}$$

$$l(t) = 1 + a_{\mu L} \cdot e^{-t/\tau_{\mu L}}, \tag{5.18}$$

[5]This technique was used in the analysis of the CERN-III data [12].

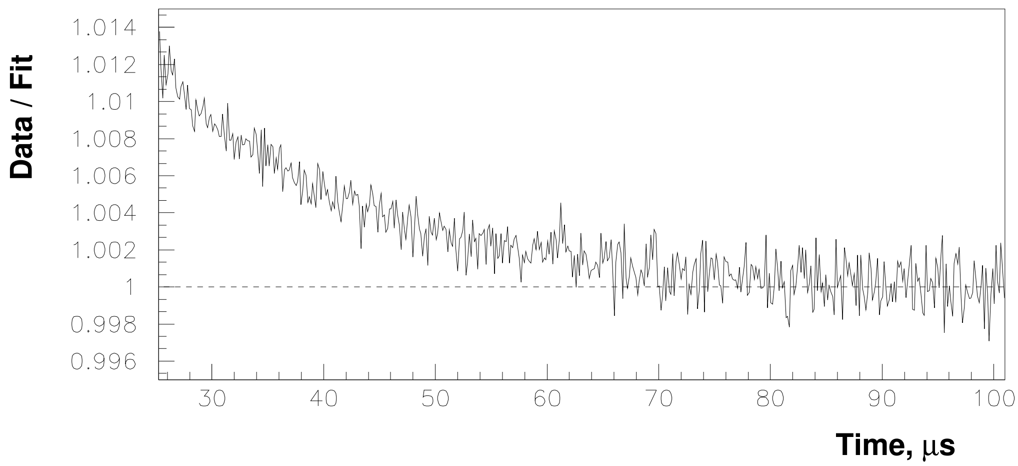

Figure 5.15: The ratio of the positron decay spectrum to the late-time fit (100-600 μs), shows a significant excess of positron counts at early times after the injection (before 60 μs).

with $a_{\mu L}$ and $\tau_{\mu L}$, respectively the muon loss amplitude and decay time. Since fit to the data started at relatively late time (30 μs and later, due to late turn-on times for some detectors), the effect of muon losses on the counting rate could be equally well (in terms of fit χ^2) described by either the gaussian form (Eqn. 5.17, with $\tau_{\mu L} \simeq 32$ μs and $a_{\mu L} \simeq 0.011$), or the exponential form (Eqn. 5.18, with $\tau_{\mu L} \simeq 22$ μs and $a_{\mu L} \simeq 0.035$).

The function given by Eqn. 5.18 is similar to the muon loss corrections used in the analyses of the CERN-II and CERN-III data (given by Eqns. 2.10 and 2.16 respectively).

5.3 Fitting Procedure

To perform fits to the data, the author wrote a `FORTRAN77` program using the standard fit software package `MINUIT`[67]. Successive calls were made to the `MINUIT` routines: `MIGRAD`, `HESSE`, `IMPROVE` and `MINOS`.

`MIGRAD` is a χ^2 minimization algorithm, using the Davidon-Fletcher-Powell variable metric technique [68]. `HESSE` is called by `MIGRAD` to recalculate the error matrices at the minimum. `IMPROVE` attempts to find a new local minimum in the vicinity of the one found by `MIGRAD`. And `MINOS` performs a better evaluation of fitting errors, taking into account possible non-linearities around the minimum.

Fit χ^2 was defined as:

$$\chi^2 = \sum_{i=1}^{n} \frac{[N_i - f(t_i)]^2}{\sigma_i^2}, \tag{5.19}$$

where N_i is the content of the ith histogram bin, σ_i is the estimated error, $f(t_i)$ is the value of the fitting function calculated at the time, t_i, corresponding to the center of the ith bin, and n is the number of bins used (typically, $n \simeq 3800$). In the first iteration, $\sigma_i = \sqrt{N_i}$ was used. In the subsequent iterations, the errors were substituted with $\sqrt{f(t_i)}$, with $f(t_i)$ from the preceding iteration. This method was found to produce an unbiased result [69]. The minimization proceeded as long as χ^2 varied by more than 10^{-4} from one iteration to the next. Convergence was usually achieved within 3 iterations with $\sigma_i = \sqrt{f(t_i)}$.

The sum of the data from 22 detectors, as well as the data from individual detectors separately, were fit to:

$$f(t) = [n(t) + p(t)] \cdot b(t) \cdot l(t), \tag{5.20}$$

where $n(t)$ is the original 5-parameter function, $p(t)$ is the pile-up function, $b(t)$ is the correction for betatron oscillations, and $l(t)$ is the muon loss correction, which are described respectively by Eqns. 5.9, 5.10, 5.16 and 5.17. The anomalous precession frequency, ω_a, was expressed in terms of its relative deviation, R, measured in parts per million, from the fixed reference frequency, $f_0 = 229.1$ kHz:

$$R\ (\text{ppm}) = \frac{2\pi f_0 - \omega_a}{2\pi f_0} \cdot 10^6, \tag{5.21}$$

$$\omega_a = 2\pi f_0 (1 - R \cdot 10^{-6}). \tag{5.22}$$

Three out of 16 parameters in Eqn. 5.20 were fixed in the fit at all times. These were the pile-up phase, $\Delta\phi_p$ = -68 mrad, and the parameters of pile-up amplification due to fast rotation: $a_p = 0.71$ and τ_p=12.7 μs. The values of these parameters were determined from fit to constructed pile-up spectrum and studies using the average energy data, as described in Section 5.2.1. Letting $\Delta\phi_p$ vary increases the error on the fit parameter R (namely, the precession frequency, ω_a) two-fold [59]. And the parameters describing the fast rotation correction to pile-up, if let vary freely, cause fit instabilities due to small size and short life time of this correction. The function given by Eqn. 5.20 will be referred to as the "13-parameter function", reflecting the number of free parameters.

The earliest start time for the fit to the sum of data from all detectors was after all detectors were gated on, approximately 30 μs after the injection. To investigate the stability of the fit parameters, fits were performed for a range of different start times, between 30 and 100 μs with a step of approximately two cyclotron periods, or 300 ns. The choice of the fit stop time of 600 μs was defined by the requirement that the data from each of the detectors have at least 10 events per histogram bin, in order to assure gaussian distribution in events in a given bin. Fitting with later stop times would not reduce the statistical error on ω_a significantly.

For the purposes of making the multi-parameter fit more stable with later start times, some parameters were allowed to vary at earlier start times only: the muon

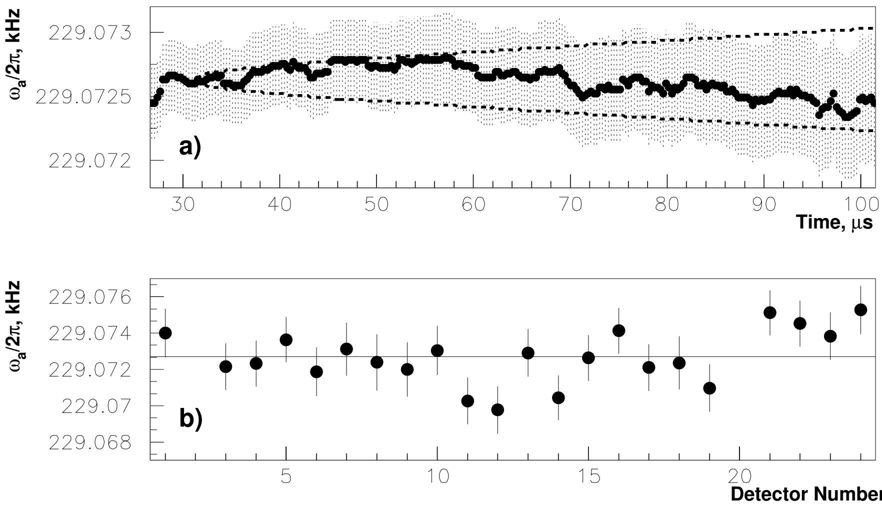

Figure 5.16: a) The fitted frequency $\omega_a/2\pi$ vs start time of the fit, from fit to the sum of the data from 22 detectors. The shaded area represents a one standard deviation statistical error band. The broken line shows the size of expected one-σ statistical fluctuations with respect to the result at 32 μs (given by Eqn. 5.24). b) Results of the fit to the spectra from individual detectors. The fit region was 32-600 μs, detectors 2 and 20 were not used in the analysis due to hardware problems.

loss amplitude, $a_{\mu L}$, and CBO decay time, τ_B, were fixed after 50 μs; the muon loss decay time, $\tau_{\mu L}$, after 70 μs; and the CBO frequency, f_B, after 80 μs.

5.4 Fit Results

Fits with the 13-parameter function (Eqn. 5.20) were performed for different energy cuts and for each detector individually. The results for the value of ω_a from fit to the summed data from all detectors, and from 22 detectors separately are shown in Fig. 5.16. The results from 22 detectors were in good agreement, with χ^2 of 28 for 21 degrees of freedom. The average of the detector results agreed well with the result from the sum of all data.

Figures 5.17, 5.18 show the time stability of other fit parameters with time, for the data selection with the energy threshold of 2 GeV. The values of the parameters from fits to the data from different detectors are plotted in Figures 5.19, 5.20.

5.4.1 Quality of Fit and Statistical Consistency

As was mentioned in Section 5.2, the 5-parameter function (Eqn. 5.9) was not sufficient to describe the 1999 data: the fit returned an unacceptable χ^2, and the results

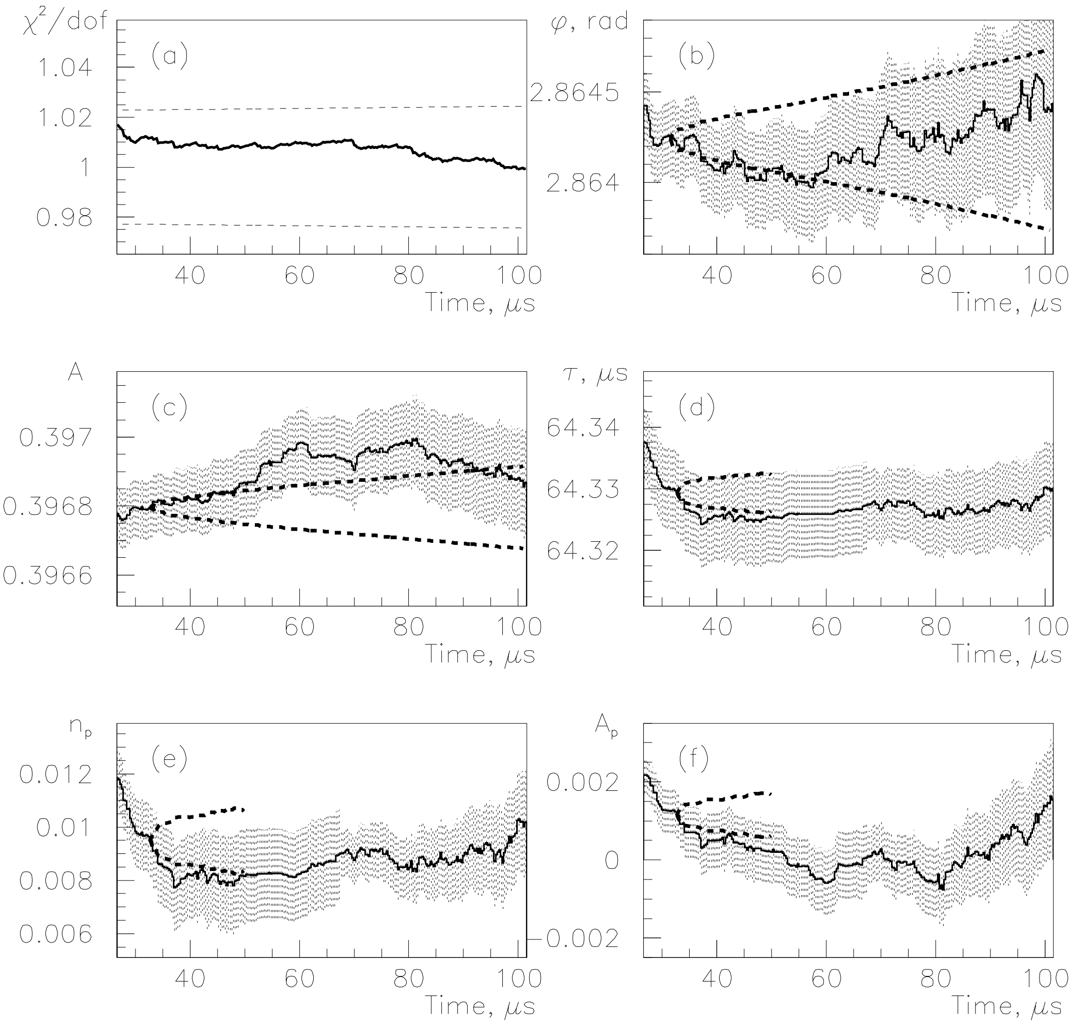

Figure 5.17: Fit results for the selection of positrons with $E > 2$ GeV: (a) χ^2 per degree of freedom vs fit start time (acceptable one-standard-deviation bands are shown as broken lines). Fit parameters are shown vs function of fit start time: (b) phase of the anomalous precession, ϕ; (c) decay asymmetry, A; (d) dilated muon lifetime, $\tau_0\gamma$; (e) pile-up fraction, n_p; and (f) pile-up asymmetry, A_p. Shaded areas represent one standard deviation statistical error bands. The broken line shows the size of expected one-σ statistical fluctuations with respect to the result at 32 μs (given by Eqn. 5.24, where applicable: since the parameters τ, n_p and A_p are correlated to the muon loss parameter a_μ, which is fixed for the fit start times after 50 μs, Eqn. 5.24 can only be applied to compare the results for the fit start times before 50 μs).

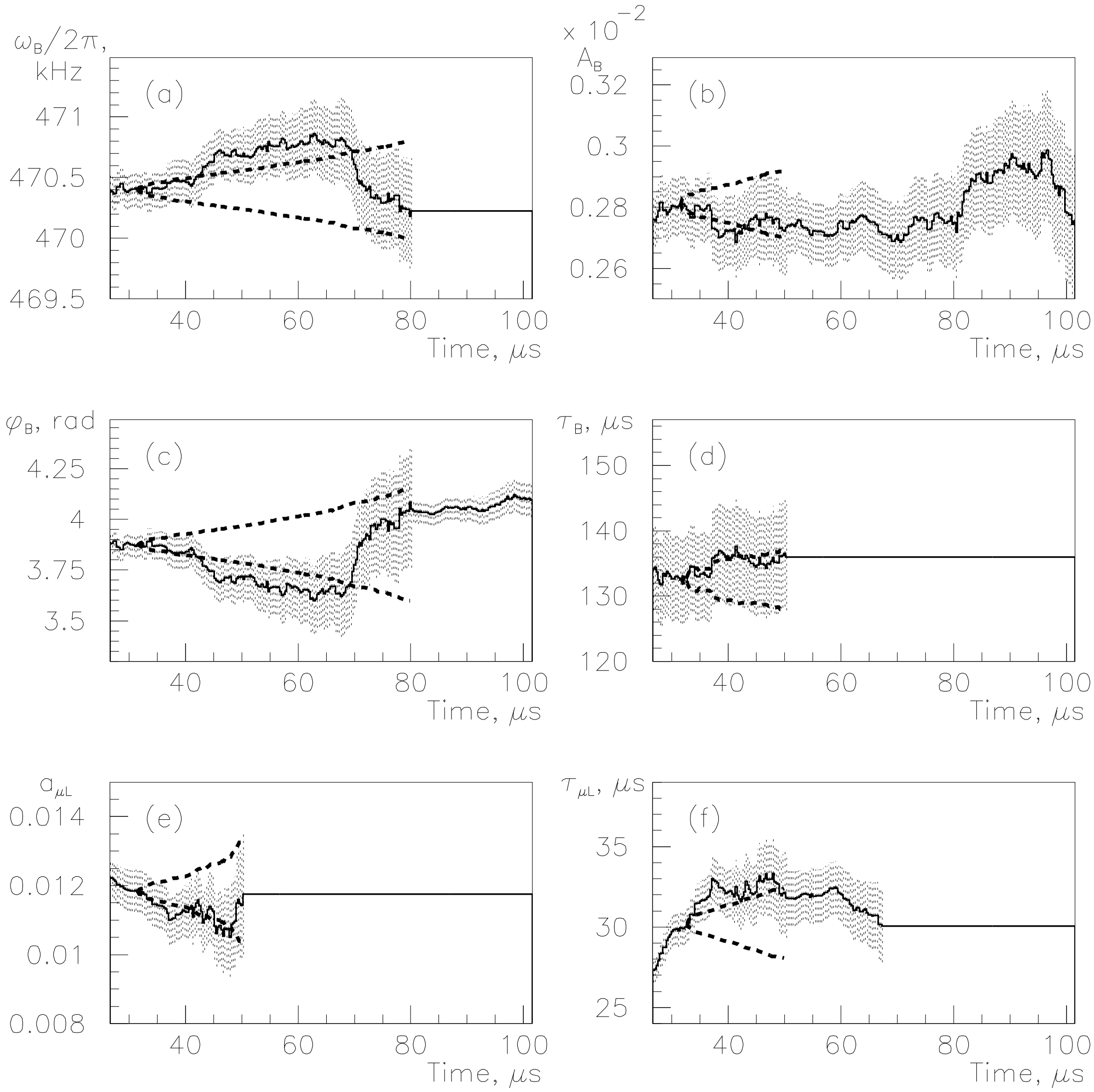

Figure 5.18: Fit parameters are shown vs fit start time for the selection of positrons with $E > 2$ GeV. Betatron oscillation parameters: (a) frequency, f_b (fixed after 80 μs), (b) amplitude, A_B; (c) phase, ϕ_B; (d) decay time; τ_B (fixed after 50 μs); and muon loss parameters: (e) amplitude, $a_{\mu L}$ (fixed after 50 μs) and (f) decay time, $\tau_{\mu L}$ (fixed after 70 μs). The broken line shows the size of expected one-σ statistical fluctuations with respect to the result at 32 μs (given by Eqn. 5.24, where applicable).

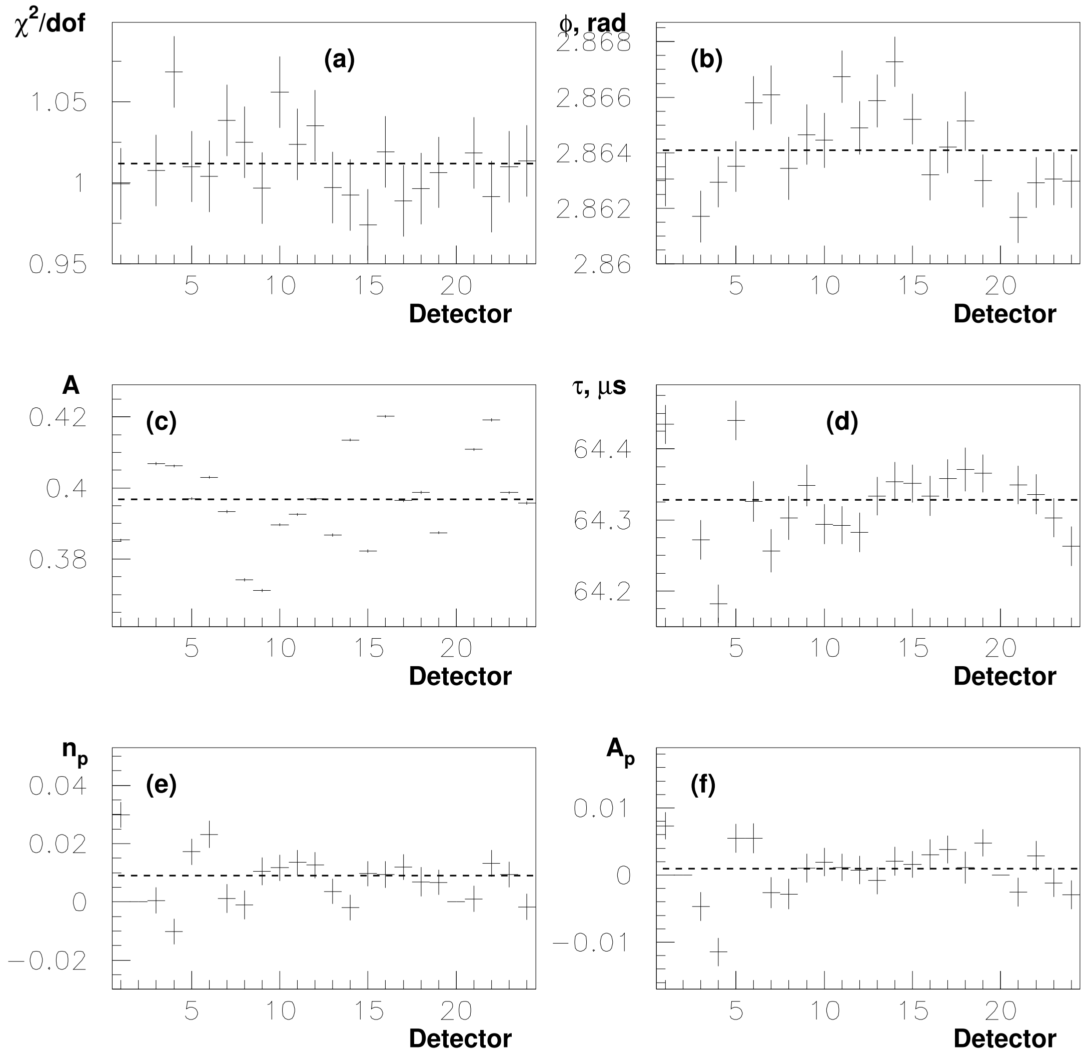

Figure 5.19: Results for the data from 22 detectors fit separately from 32 to 600 μs. Fit parameters vs detector number: (a) χ^2 per degree of freedom; (b) decay asymmetry, A; (c) dilated muon lifetime, $\tau_0\gamma$; (d) phase of the anomalous precession, ϕ; (e) pile-up fraction, n_p, and (f) asymmetry, A_p. The corresponding results for the sum of the data are shown for comparison as broken lines.

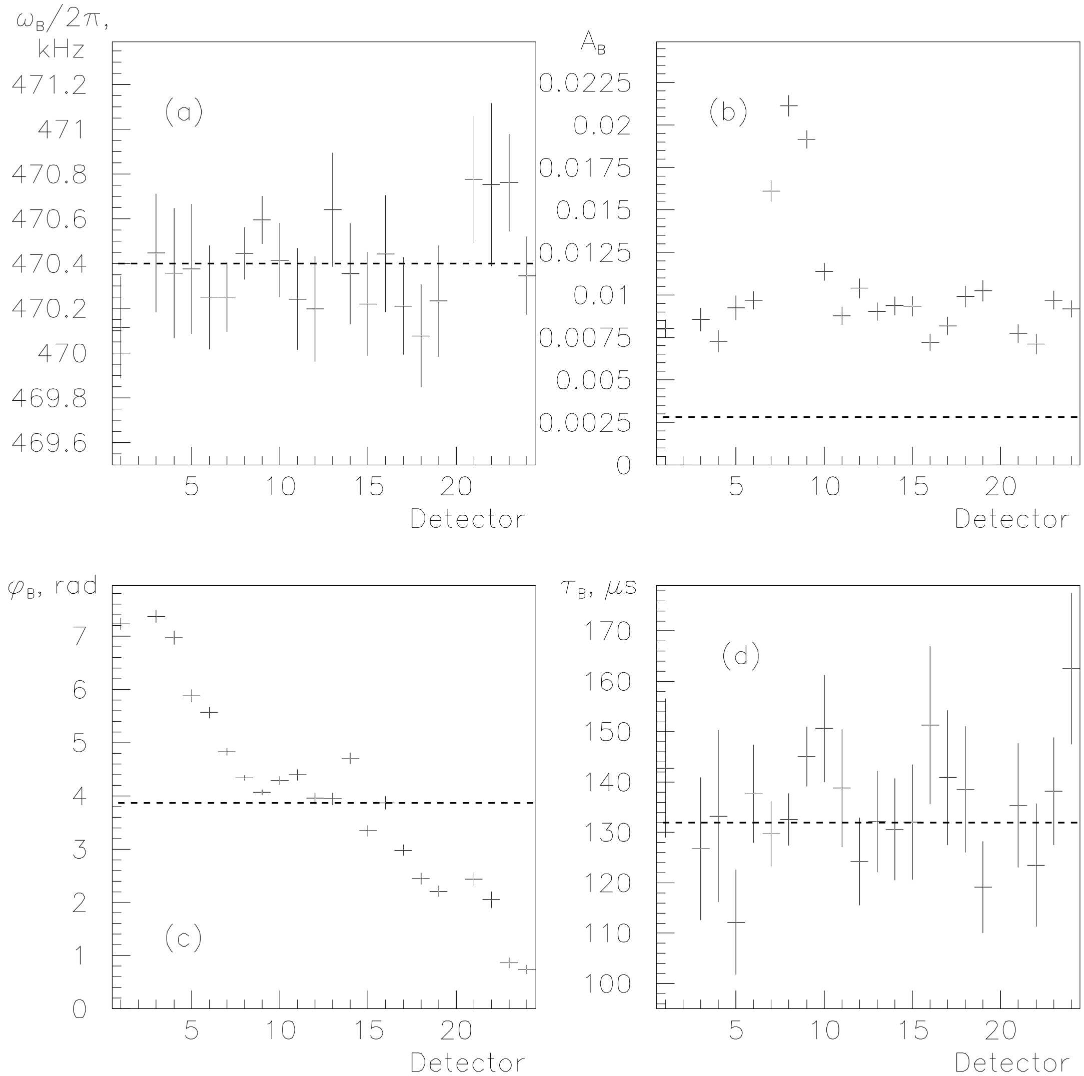

Figure 5.20: Results for the data from 22 detectors fit separately from 32 to 600 μs. Betatron oscillation parameters vs detector number: (a) frequency, f_b; (b) amplitude, A_B; (c) phase, ϕ_B; (d) decay time, τ_B. The corresponding results for the sum of the data are shown for comparison as broken lines.

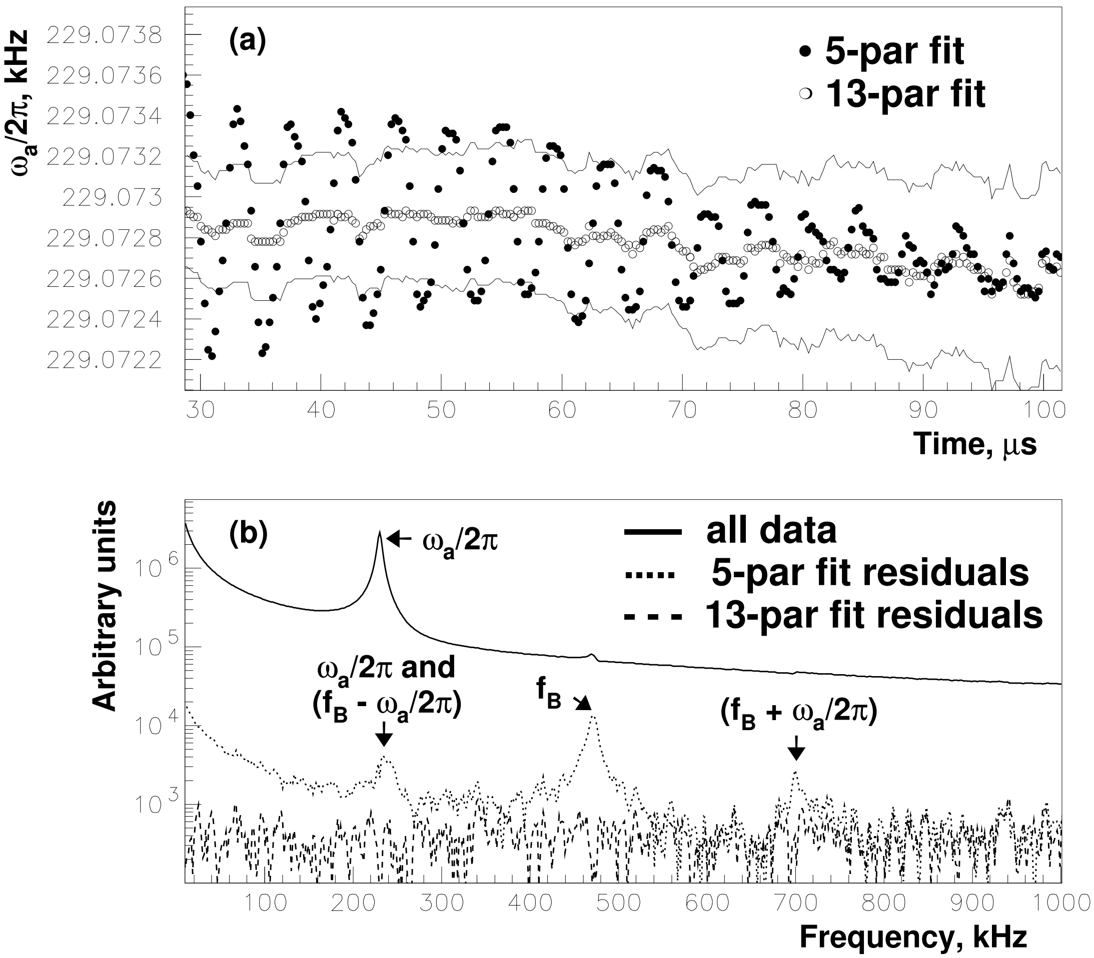

Figure 5.21: Additional fit parameters were weakly correlated with ω_a and served to eliminate the phase pulling and improve the fit χ^2: (a) fitted values of ω_a are compared for the 5- and 13-parameter functions; statistical error bands are shown for the 13-parameter fit result. (b) Fast Fourier transform of the data and fit residuals of the 5- and 13-parameter functions.

Table 5.1: χ^2 per degree of freedom from fit to the sum of data from 22 detectors, for different fit start times and forms of the fitting function. In the fitting function expression: $n(t)$ is the 5-parameter function, $p(t)$ is the pile-up function, $b(t)$ is the correction for betatron oscillations, and $l(t)$ is the muon loss correction, which are described respectively by Eqns. 5.9, 5.10, 5.16 and 5.17. Underlined are the statistically acceptable values of χ^2/DOF (see Eqn. 5.23).

Fitting function	Number of fit param.	χ^2/DOF for fit starting at 32 μs	60 μs	90 μs
$n(t)$	5	2.946	1.398	1.120
$n(t) + p(t)$	7	1.580	1.237	1.102
$[n(t) + p(t)] \cdot b(t)$	11	1.114	1.038	$\underline{1.023}$
$[n(t) + p(t)] \cdot b(t) \cdot l(t)$	13	$\underline{1.012}$	$\underline{1.009}$	$\underline{1.003}$

showed a strong dependence on the choice of the fit start time (phase pulling).

Phase pulling occurs if the background and other factors affecting the data are not sufficiently accounted for in the fitting function. Since the relative contribution from the background to the content of the bin corresponding to the fit start time varies depending on the phase of the anomalous precession at that bin, the effect on the fit results from the background depends on the fit start time. Thus, phase pulling manifests itself as a periodic oscillation in the values of fit parameters vs fit start time. The amplitude of the effect is determined by how well the function models the data [35]. Figure 5.21(a) shows phase pulling in the value of ω_a vs fit start time, observed when the 5-parameter function was used to fit to data. The phase pulling was minimized after the additional parameters had been added. Most of the new parameters are rather weakly correlated with ω_a, and, as a result, the values of ω_a, averaged over the period of phase pulling, did not change significantly.

On the other hand, extending the fit function resulted in a dramatic decrease in the fit χ^2 (see Table 5.1). When the summed data from all detectors were fit to the 13-parameter function, the χ^2 per degree of freedom was 1.012 (for fit from 32 to 600 μs with 3794 degrees of freedom) consistent with its expected value of

$$\chi^2/n_{DOF} = 1 \pm \sqrt{2/n_{DOF}} \simeq 1 \pm 0.023. \tag{5.23}$$

As illustrated in Fig. 5.21(b), Fourier analysis of the fit residuals shows, that the strong betatron frequency peak, as well as a low-frequency tail associated with the (exponentially decreasing with the time) muon losses, disappeared after the new parameters were added. No significant background (peaks in the Fourier spectrum) is present in the frequency range up to 1 MHz.

To check the data consistency throughout the run, the 1999 data set was divided into 12 subsets corresponding to different time periods, and each of these subsets was then fit to separately. The results for ω_a were found in good agreement with $\chi^2 = 12.2$ for 11 degrees of freedom, as illustrated in Fig. 5.22(a).

Besides the χ^2 criterion, a quantitative consistency check can be made using the correlated differences in the values of a fit parameter P from fits with different start times. Since for any two fit start times, $t_i < t_j$, if the same fit stop time, t_s, is used, the data set corresponding to t_j (covering the range from t_j to t_s) would be an exact subset of the one corresponding to t_i, the correlated error $\sigma_P(t_i, t_j)$, which is the expected standard deviation between the values $P(t_i)$ and $P(t_j)$, is:

$$\sigma_P(t_i, t_j) = \sqrt{\sigma_P^2(t_j) - \sigma_P^2(t_i)} \tag{5.24}$$

where $\sigma_P(t_i)$ and $\sigma_P(t_j)$ are statistical errors on the parameter P from fits started at times t_i and t_2 respectively. We then expect the distribution of the correlated differences,

$$\mathcal{D}_P(t_i, t_j) = \frac{P(t_j) - P(t_i)}{\sigma_P(t_j, t_i)}, \tag{5.25}$$

to be an unbiased gaussian with a width of 1 [70], as illustrated for ω_a in Figure 5.23.

The formula given by Eqn. 5.24 can be used as a criterion of the parameter stability with respect to the fit start time (provided the parameter cross-correlations do not change significantly from early to late start times, e.g. due to fixing parameters strongly correlated to the parameter of interest). In Figure 5.16(a) the $\sigma_{\omega_a}(t_i, t_j)$ bounds of expected statistical variation in ω_a for different fit start times, t_j between 32 and 100 μs are shown with respect to the result from the fit with the start time $t_i = 32$ μs.

Generally, the results for ω_a from fits to two data sets, one of which (Σ_j) is an exact subset of the other (Σ_i), are expected to differ by:

$$\sigma_{ij} = \sigma_i \cdot \sqrt{1 + \frac{\sigma_j^2}{\sigma_i^2} - 2\frac{A_i}{A_j}\cos(\phi_i - \phi_j)} \tag{5.26}$$

where $\sigma_{i(j)}$, $A_{i(j)}$, $\phi_{i(j)}$ are respectively the statistical error on ω_a, asymmetry and phase for the subset Σ_i (Σ_j) [71]. It is easy to see that Eqn. 5.24 is equivalent to Eqn. 5.26, for $A_i = A_j$ and $\phi_i = \phi_j$.

Eqn. 5.26 can be used to estimate acceptable variation in results of fit to selections of positrons with different energy cuts: obviously a selection with a higher cut is an exact subset of a selection with a lower cut. For the results from the cuts of 2 and 2.2 GeV, Eqn. 5.26 allows a variation of $0.54{\cdot}\sigma$, where σ is the statistical error of the former. For the cuts 2 and 2.4 GeV, the variation is $0.8{\cdot}\sigma$. These estimates were confirmed by the author in a simulation. As shown in Fig. 5.22(b) the results of fits to data sets with different energy cuts agreed within expected statistical variation.

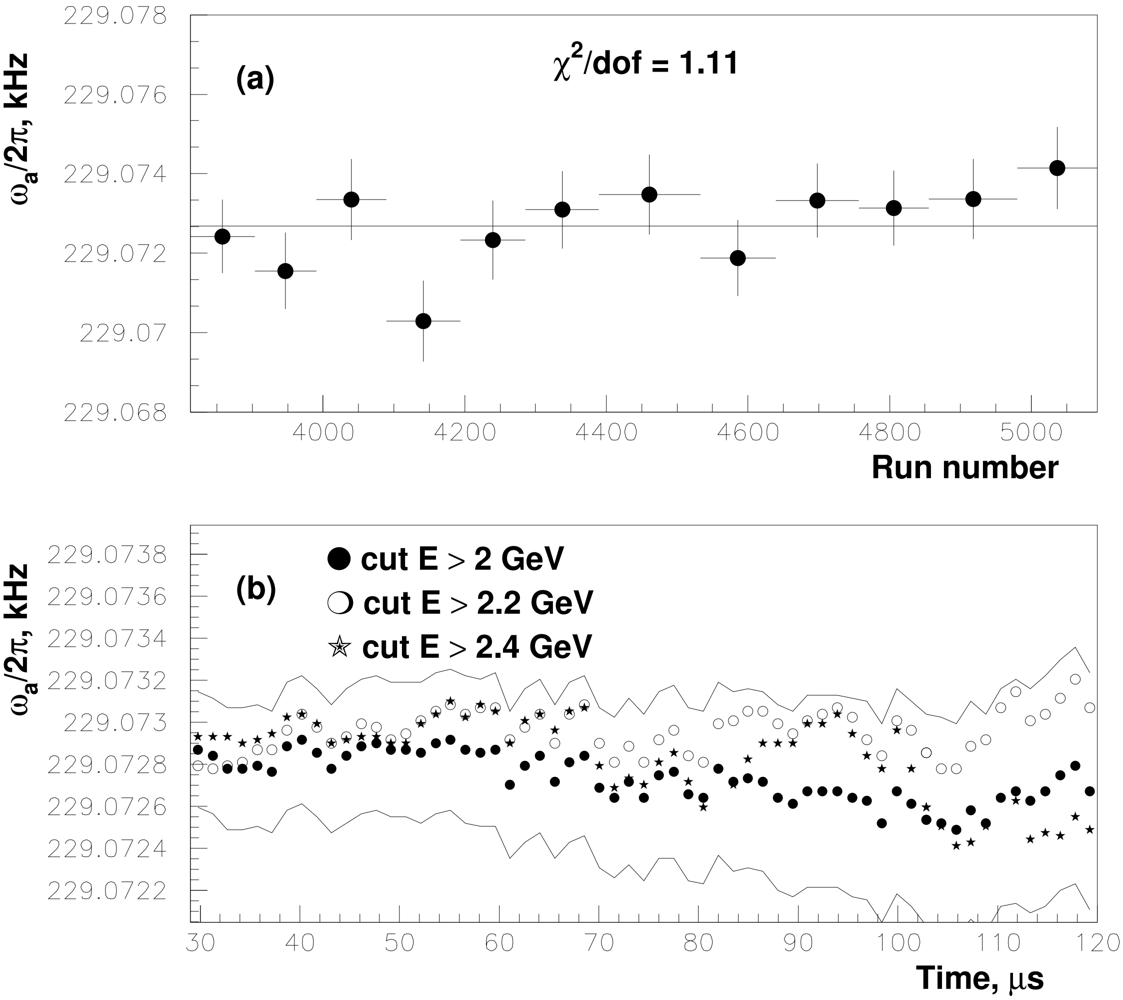

Figure 5.22: Consistency checks: (a) the values of ω_a from fit to 12 subsets of the data taken during different periods of the 1999; (b) the results from fit to data with different energy cuts (with the statistical error bands shown for the cut $E > 2$ GeV).

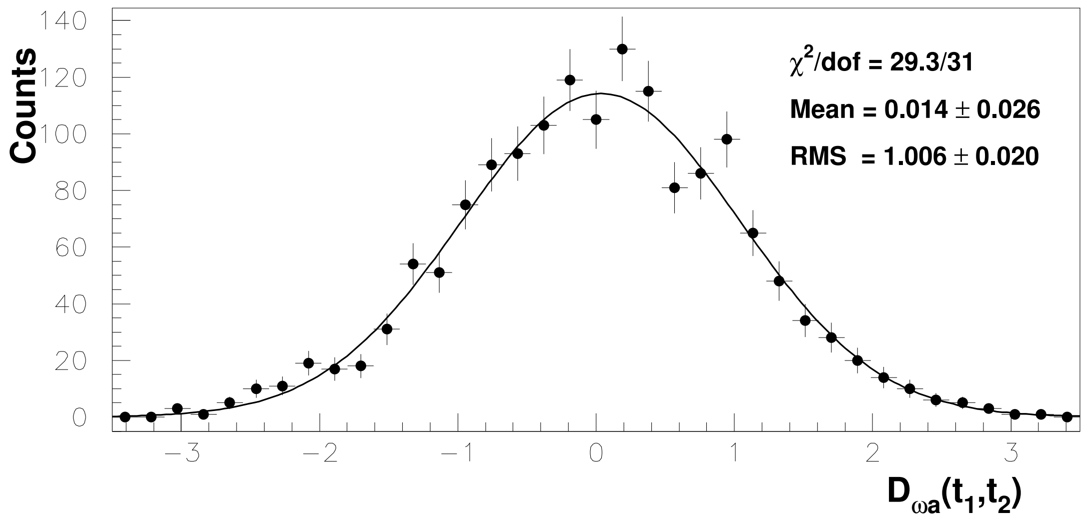

Figure 5.23: The distribution of $\mathcal{D}_{\omega_a}$, given by Eqn. 5.25, has the gaussian form with the RMS of 1.

5.4.2 Comparison of the Results of 4 Analyses

Four independent analyses of ω_a, were performed at Boston (BU), Brookhaven (BNL), the University of Illinois (UI) and the University of Minnesota (UM), using different production algorithms, data selection criteria, fitting methods and functions.

The BU and BNL analyses used `G2Off` production, while UI and UM used `G2Too`. Constructed pile-up was subtracted from the data sets used in the BNL, UI and UM analyses. The BNL and UI analyses used fitting functions similar to the 13-parameter function, with $p(t) \equiv 0$ (no pile-up). At BNL, the CBO frequency (f_B) was fixed in the fit after studies. In the UI analysis, both f_B and the muon loss decay time ($\tau_{\mu L}$) were fixed. The UM analysis used the Ratio method [72], in which a ratio is constructed from four random samples of the data. Such ratio turns out largely independent of changes on scale larger than the spin precession period ($\simeq 4.365\ \mu$s), e.g. the muon lifetime, and therefore can be fitted with fewer parameters.

The summary of the four analyses is given in Table 5.2. The results were found to agree to 0.3 ppm, well within the expected statistical variation of 0.4 ppm, due to the differences in the analyzed data sets. (These differences were caused by the use of various procedures for detector energy calibration, treatment of pile-up and energy scale changes etc.)

5.4.3 Corrections to ω_a

Since not all stored muons have momenta exactly equal to the "magic" value (see Section 3.2), the result for ω_a obtained from a fit to the data should be corrected for

Table 5.2: The results of four ω_a analyses. $R = (1 - \omega_a/2\pi f_0) \cdot 10^6$, where $f_0 =$ 229.1 kHz. The errors on R are statistical. The UI result is a weighted mean of results of fit to data from individual detectors, with different fit start times [73].

Institute	Fit start time	Number of fit param.	χ^2/DOF	R, ppm	Ref.
BU	32 μs	13	1.012 ± 0.023	119.55 ± 1.24	[60]
BNL	32 μs	10	1.005 ± 0.023	119.38 ± 1.24	[74]
UI	25-56 μs	9	1.016 ± 0.005	119.60 ± 1.23	[75]
UM	34 μs	3	0.986 ± 0.025	119.67 ± 1.28	[72]

the residual effects of the focusing electric field (see Equation 2.13).

Equation 2.13 is derived with the assumption that the muon velocity is perpendicular to the magnetic field $\vec{B}$, i.e. the muon orbits lie in a plane perpendicular to the field vector. If the velocity has a small angle relative to this plane, the particles will follow a spiral path with pitch angle ψ changing periodically between positive and negative values with vertical betatron frequency (given by Eqn. 3.3) [76]. The fitted value of ω_a should be corrected for the effects of such pitching motion.

The total correction is given by:

$$\omega_a = \omega_a^{Fit} \cdot (1 + C_E) \cdot (1 + C_P) \simeq \omega_a^{Fit} \cdot (1 + C_E + C_P), \tag{5.27}$$

$$C_E = \left\langle \beta \big(1 - \frac{1}{a_\mu \beta^2 \gamma^2}\big) \frac{E_r}{B} \right\rangle \simeq 2n(1-n) \frac{\langle x_e^2 \rangle}{\rho^2}, \tag{5.28}$$

$$C_P = \frac{1}{2} \langle \beta^2 \psi^2 \rangle \simeq \frac{n}{2} \frac{\langle y^2 \rangle}{\rho^2}, \tag{5.29}$$

where ω_a^{Fit} is the value obtained from fit to data, C_E and C_P are respectively the corrections for the effects of the electric field and the betatron pitching motion, $\beta = v_\mu/c$, $\gamma = 1/\sqrt{1-\beta^2}$, E_r is the radial component of the electric field, n is the field index (see Eqn. 3.1), x_e is the displacement of the equilibrium orbit from the center of the storage ring aperture, y is the instantaneous vertical position of the particle above the median plane, and $\rho = 7.112$ m is the radius of curvature of the ring at the center of the aperture [76, 77]. Obviously, $C_E = 0$ for the "magic" $\gamma = \sqrt{1 + 1/a_\mu}$.

The values of $\langle x_e^2 \rangle$ and $\langle y^2 \rangle$ are obtained from simulation and from the studies of the stored muon distribution. For the 1999 result the E-field correction was $C_E =$ 0.52 ppm, the pitch correction was $C_P = 0.29$ ppm, and the systematic error on C_P and C_E combined was 0.08 ppm [78].

Combining the results of the independent analyses [79], and including the correction for the electric field and the muon pitching motion, the anomalous precession

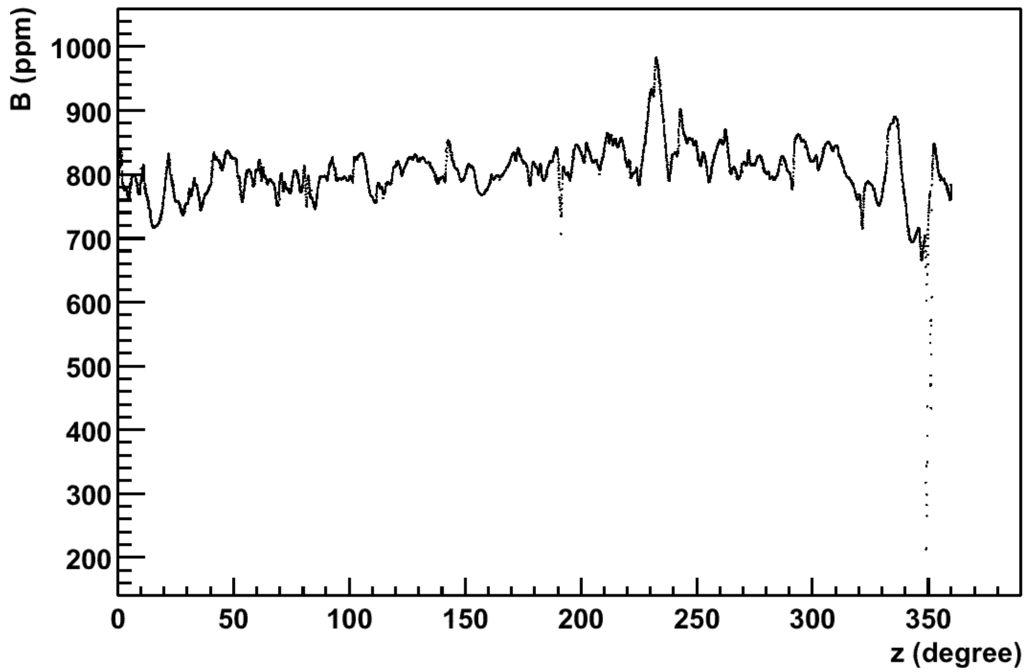

Figure 5.24: The magnetic field measured with the trolley center probe vs azimuth for one of the trolley measurements. The dip at 350° is due to the inflector fringe field [80].

frequency was found to be:

$$\omega_a/2\pi = 229\ 072.8 \pm 0.3\ \text{Hz} \quad (1.3\ \text{ppm}), \tag{5.30}$$

where the statistical error of 1.25 ppm and the systematic error of 0.3 ppm are added in quadrature. The systematic error of the ω_a measurement will be discussed in the next chapter.

5.5 Magnetic Field Analysis

The average magnetic field seen by the muons was calculated in software by tracking a sample of muons through a measured field map taken in 1998 and by averaging the field values these muons encounter. (Although there were small changes in the field in 1999 compared to 1998, the muon dynamics was not affected significantly.) The resulting average magnetic field agrees within 0.05 ppm with the field value taken at the beam center and averaged over azimuth.

The equilibrium muon distribution was obtained from the analysis of the fast rotation data. It was found that the equilibrium center of the muon distribution was

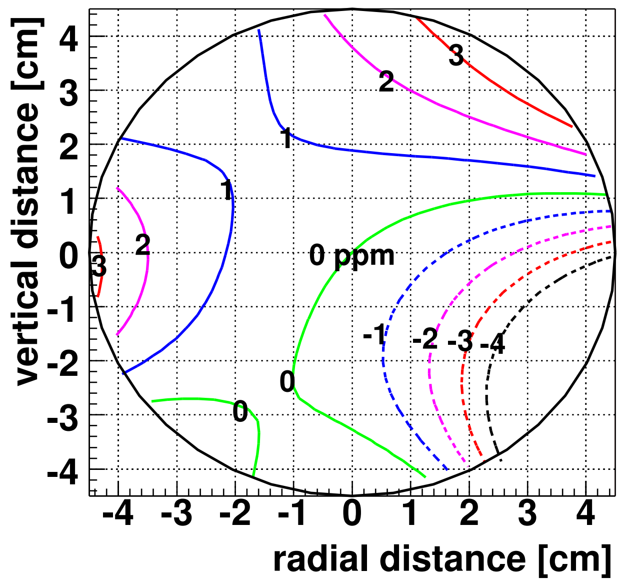

Figure 5.25: A 2-dimensional multipole expansion of the field averaged over azimuth from one of the trolley measurements. One ppm contours are shown with respect to a central average field $B_0 = 1.451\ 266$ T. The circle indicates the muon beam storage region [1].

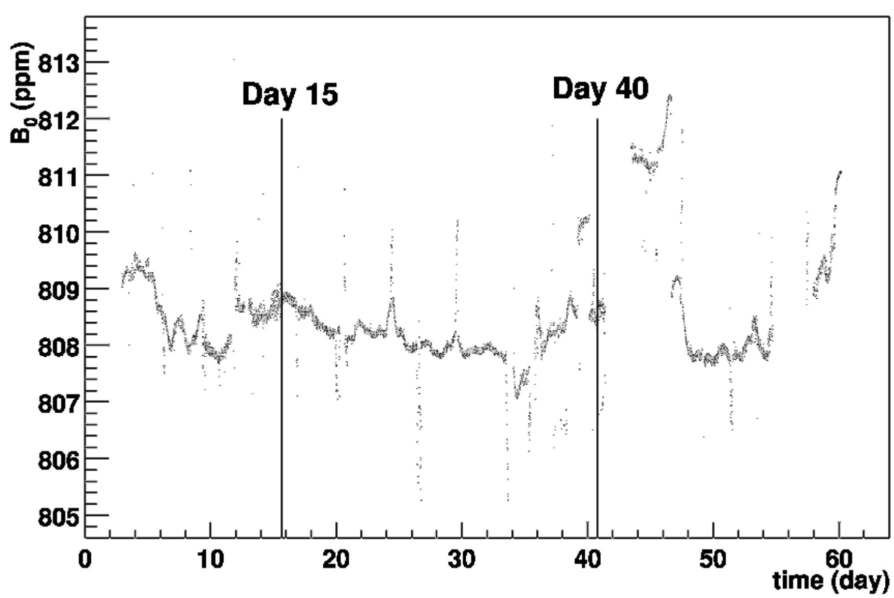

Figure 5.26: The B field averaged over 10 minutes vs time in days. The data-taking took place between days 15 and 40 [80].

3.7 mm outwards from the center of the storage region (with an error of 1mm).

The results of two largely independent analyses of the magnetic field, each using different sets of about 150 fixed NMR probes, agreed to within 0.03 ppm [1, 80].

The final value of the proton NMR frequency for the 1999 data was

$$\omega_p/2\pi = 61\ 791\ 256 \pm 25\ \ \text{Hz} \qquad (0.4\text{ppm}), \tag{5.31}$$

where the error of the ω_p measurement is systematic (it will be discussed in the next chapter).

Chapter 6

Systematic Uncertainties for the 1999 Analysis

A range of studies was carried out to understand the systematic uncertainty in ω_a associated with the presence of background in the data, pile-up, muon losses, betatron oscillation and other observed effects, as well as the possible effects of the fitting method and strategy.

In this chapter, the systematic errors will be discussed for the fit parameter R (see Eqns. 5.21, 5.22), with the relative systematic error ΔR (ppm) equivalent to $(\Delta\omega_a)/\omega_a$.

Some errors were found to be minimized by starting the fit at the "zero-crossings" of the data[1], the points corresponding to $\cos(\omega_a t + \phi) = 0$ in Eqn. 5.9, where the $(g-2)$-wiggle crosses the median exponential decay line, as shown in Figure 6.1. Therefore, the final result was quoted for the fit starting at 32 μs after the injection, the first zero-crossing for which the data from all detectors were available.

6.1 Errors Due to Pile-up

The largest systematic uncertainty in the ω_a measurement came from uncertainty in the value of the phase of pile-up (which was fixed in the fit). There is a strong correlation between $\Delta\phi_p$ and R (or ω_a), and letting the former vary as a free parameter leads to a two-fold increase in the statistical error.

6.1.1 Pile-up Phase

The sensitivity of the values of the fit parameter R to the choice of the pile-up phase was estimated by fitting to the $(g-2)$ data with $\Delta\phi_p$ fixed at different values between $-\pi/2$ and $\pi/2$ rad, for various fit start time. The results for the start time of 32 μs

[1] E.g. the errors due to the changes in the energy scale (discussed in Section 6.3), muon losses (Section 6.5.1), for which the zero-crossings of the data coincide with the minima of phase pulling.

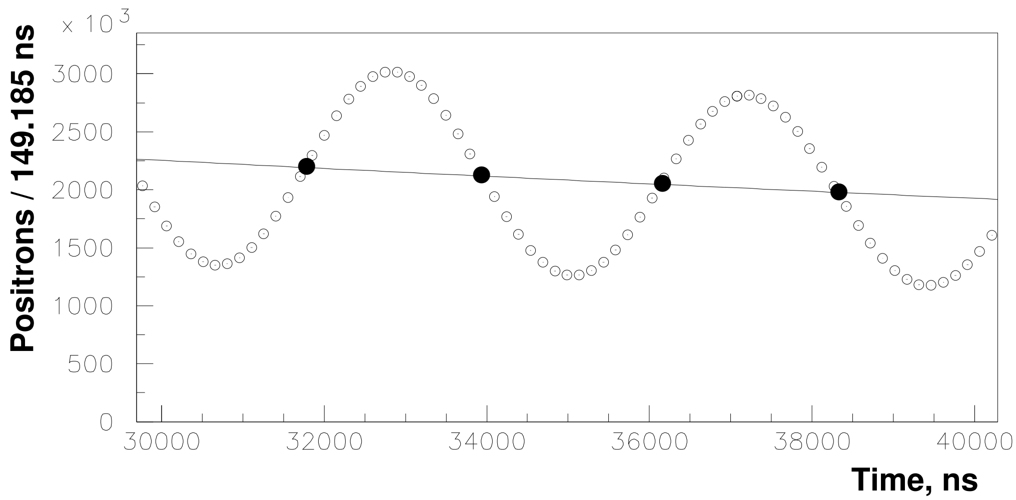

Figure 6.1: Zero-crossings of the decay positron data: the data are shown as empty circles, overlayed with fit to an exponential function; zero-crossings are shown as filled circles.

are shown in Figure 6.2: it was found that for small values of $\Delta\phi_p$, the result for R showed an almost linear dependence on the value of the pile-up phase. A change of 10 mrad in the fixed pile-up phase produced a 0.039 ppm change in R.

The value of the pile-up phase for the data selection with the energy cut of 2 GeV was determined from a fit to a constructed pile-up spectrum: $\Delta\phi_p = -68 \pm 31$ mrad. The precision with which $\Delta\phi_p$ could be determined was limited by the statistics. The uncertainty of 31 mrad in $\Delta\phi_p$ translates into a 0.12 ppm systematic effect in R (for a fit starting at 32 μs after the injection), if the value of $\Delta\phi_p$ from the studies of constructed pile-up is used.

6.1.2 Low-energy Pile-up

The low-energy pile-up pulses (with amplitudes below 10 WFD counts) cannot be reconstructed using the pulse-finding algorithm. Such "invisible" pulses could affect the determination of the reconstructed pulse parameters, resulting in an increase in the reconstructed amplitude or the pedestal value[2] determined from the fit to the average pulse shape during the data production. A study of the effects of low-energy pile-up, using simulated data, showed that it would result in an early-to-late time variation of the decay phase and asymmetry [81]. The decay asymmetry was found to be more sensitive to the presence of low-energy pulses than the phase. Subsequently the observed variation in the values of asymmetry from the fit to the $(g-2)$ spectrum

[2] In this case the reconstructed pulse amplitude would actually decrease.

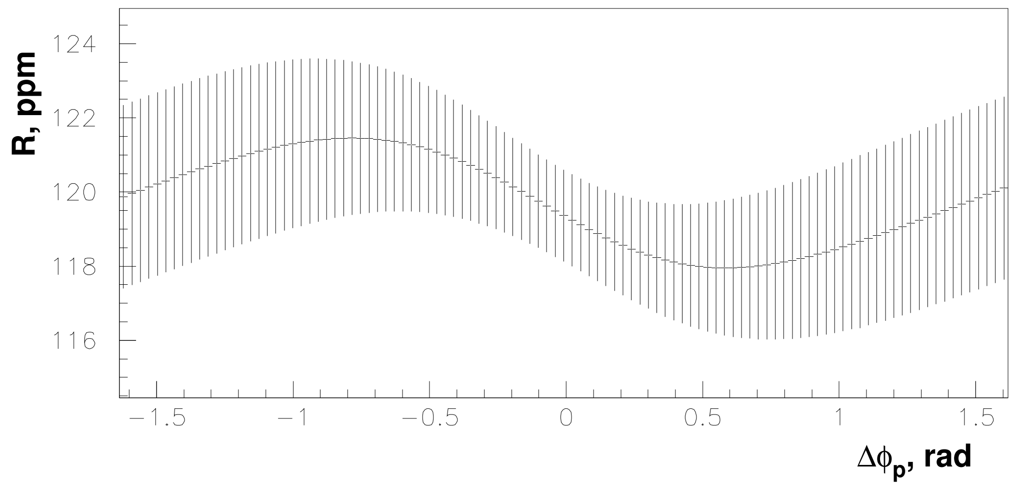

Figure 6.2: Change in the fitted value of R caused by changing the difference between the g-2 and pile-up phases (fixed parameter $\Delta\phi_p$), for the data selection with the energy cut of 2 GeV, fit from 32 and 600 μs. The values of R are shown with statistical errors from fit.

for different fit start times served as a sensitive measure of the systematic effect on ω_a due to low-energy pile-up, which was estimated to be smaller than 0.08 ppm.

Adding in quadratures the uncertainties from the pile-up phase and from the contribution of low-energy pile-up gives the overall uncertainty in ω_a of 0.14 ppm[3].

6.2 AGS Background

As was described in Section 5.1.1, a cut using the signal from the tØ counter, was applied to reduce the level of contamination of the data from the AGS periodic background, flashlets. Still the flashlets were present, mostly in the data from the detectors close to the injection point, 3 through 6. The flashlet peaks were observed in the Fourier transform spectrum of the fit residuals (Figure 6.3): a strong peak was detected at the frequency 2.228 MHz, or six times the AGS frequency, $f_{AGS} = 371$ kHz, as the flashlets arrived at the storage ring with each of the 6 bunches in an AGS cycle. The flashlets were not distributed evenly among the AGS bunches though, as most of them came typically with the first bunch [82, 83], therefore a smaller peak at the AGS frequency was observed as well.

The flashlets were studied using the data from dedicated "flashlet spills", for which the quadrupoles were turned off, therefore no muons stored in the ring. In the absence

[3] The average for 4 independent ω_a analyses was 0.13 ppm.

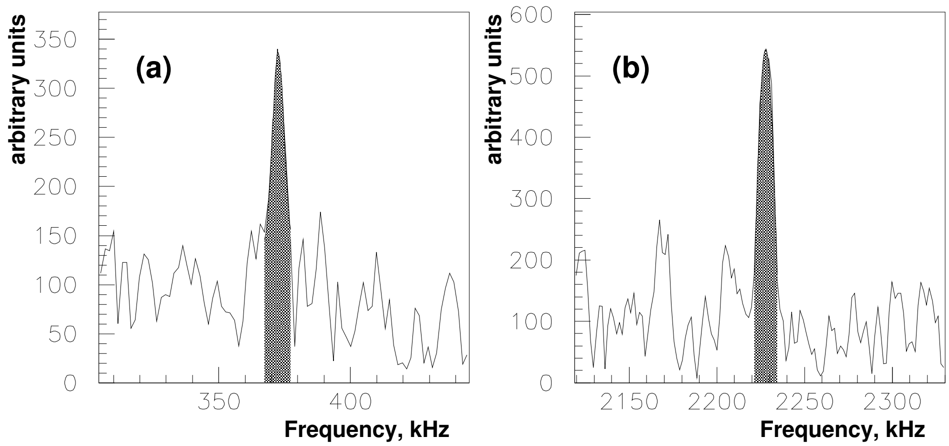

Figure 6.3: Flashlet peaks in the fast Fourier transform spectrum of the 13-parameter fit residuals (data from detector 4) are seen at (a) the AGS frequency, $f_{AGS} \simeq 371$ kHz; and (b) $f = 6 \cdot f_{AGS} \simeq 2228$ kHz.

of the pulses from muon decay positrons, the flashlets could be easily identified. For the 1999 data set, the flashlet contamination, defined as the ratio of the number of flashlets to the total number of pulses in the data, was estimated to be 126 ppm.

The flashlet time distribution may be approximated as a sum of two spectra:

$$f_{Fl}(t) = N_1(t) \cdot \sum_{i=1}^{60} \delta(t - \frac{i + \phi_1/2\pi}{371 \text{ kHz}}) + N_2(t) \cdot \sum_{i=1}^{360} \delta(t - \frac{i + \phi_2/2\pi}{2.228 \text{ MHz}}) \qquad (6.1)$$

where $N_1(t)$, $N_2(t)$ are functions describing the time-dependence of the flashlet distribution, i is a positive integer, and ϕ_1 and ϕ_2 are phases of the flashlet arrival with respect to the injection time. A parabolic envelope form was used to approximate the time distribution of flashlets, observed in the dedicated spills:

$$N_1(t) = N_{Fl_1} \cdot \frac{c_0 + c_1 t + c_2 t^2}{a}, \qquad (6.2)$$

$$N_2(t) = N_{Fl_2} \cdot \frac{c_0 + c_1 t + c_2 t^2}{6a}, \qquad (6.3)$$

where $N_{Fl} = N_{Fl_1} + N_{Fl_2}$ is the total number of flashlets in the simulated data, and the coefficients are: $c_0 = 14.257$, $c_1 = 1.695 \cdot 10^{-3}$, $c_2 = 5.352 \cdot 10^{-4}$, and $a = 560.387$.

The effects of the flashlet presence on the fit results for the value of R were investigated by fitting to data sets, "contaminated" by simulated flashlet spectra (which were generated using Eqs. 6.1, 6.2, 6.3).

It was found that the more uneven was the flashlet distribution across the spills,

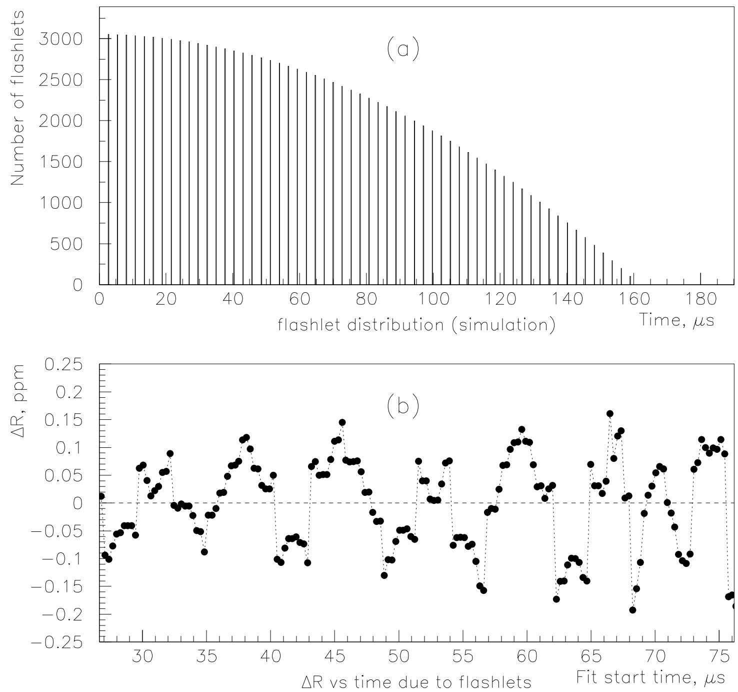

Figure 6.4: Results of a flashlet simulation ("worst case", flashlets arriving with the AGS frequency of $f = 371$ kHz): (a) flashlet spectrum generated with the AGS frequency (126 ppm contamination level); (b) shift in the fitted value of R due to flashlet contamination as a function of fit start time.

the greater was the effect of flashlet contamination on the fit results. The extreme example of the uneven distribution would be if all flashlets arrived with the same spill, say the first spill in an AGS cycle (equivalent to $N_{Fl_2} = 0$, $N_{Fl} = N_{Fl_1}$ in Equations 6.2, 6.3). The results for this "worst case" are shown in Figure 6.4.

The uncertainty in ω_a due to the presence of flashlets at the level of 126 ppm was conservatively estimated to be less than 0.12 ppb[4].

6.3 Errors Due to Changes in the Energy Scale

The energy scale changes (ESC), if not corrected for, lead to phase pulling and bias in the fit results. The use of the energy scale correction (as described in Section 5.1.3) greatly improves the fit parameter stability with respect to the start time of fit, as illustrated in Figure 6.5.

[4]The average for 4 ω_a analyses was 0.1 ppm

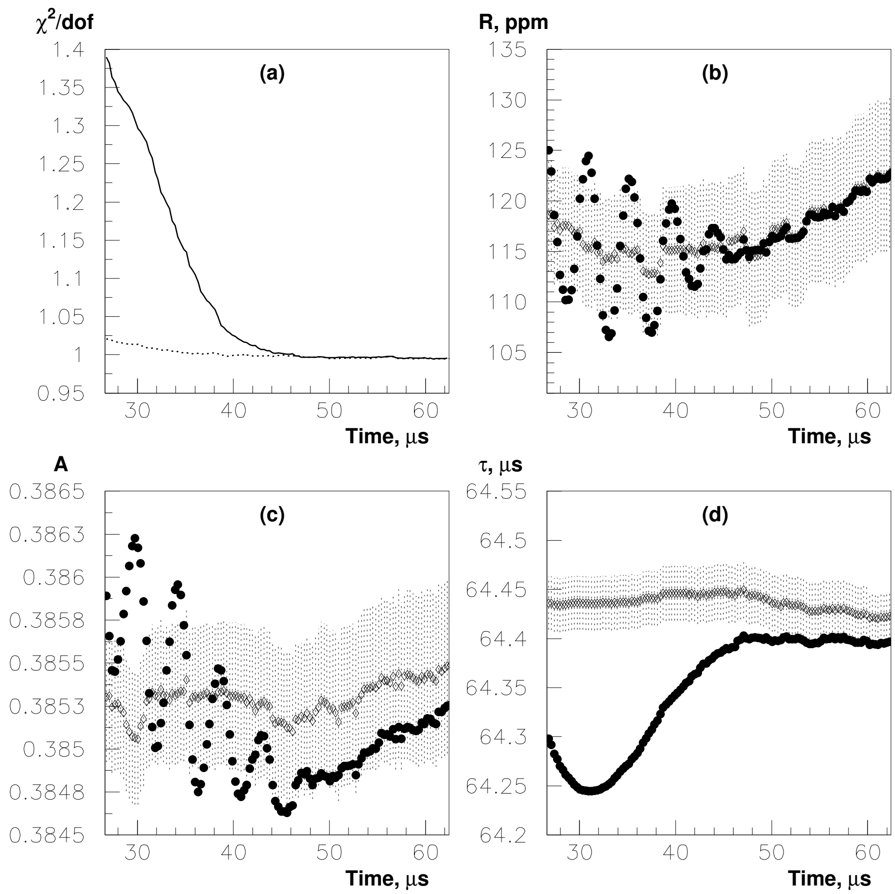

Figure 6.5: Results of fit to the data from detector 1 are compared: (a) fit χ^2 per degree of freedom vs fit start time, shown before (solid line) and after (dots) the ESC correction was applied; (b) the fit parameter R, (c) decay asymmetry, (d) dilated muon lifetime vs fit start time, before (filled circles) and after (diamonds) the correction, shaded area shows fit errors for the ESC-corrected result.

An estimate of the effect of the residual energy scale change, due to the limited efficiency of the ESC correction, was done by comparing the values of fit parameters between fits to two data sets, one of which was created using a fixed energy threshold for the event selection, and the other using a variable threshold ("ESC-corrected" data set). It was found that even a significant change in ESC, of as much as 0.3-0.7%, observed in the data from detectors 1 and 4, had little effect (< 50 ppb) on the fitted value of R at the zero-crossings.

A similar result was obtained in a simulation, in which an artificial variation of the energy scale was introduced at the selection stage for the data coming from an ESC-stable detector, and the resulting effect on the fit results was then observed.

For the sum of the data from all detectors, this residual effect from ESC was smaller than for most individual detectors, due to mutual cancellation. For the 1999 data set the amplitude of ESC was estimated to be under 0.1%, which resulted in the systematic error on ω_a of less than 0.1 ppm overall, and less than 10 ppb for a fit starting at a zero-crossing (e.g. 32 μs).

6.4 Randomization and Binning Errors

Beam bunching at early times after the injection (fast rotation) was known to bias the fit results. The effect of fast rotation was minimized by choosing the bin width equal to the cyclotron period of 149.185 ns, and uniformly randomizing the injection time for each data spill over one bin width. Ten statistically equivalent randomized data sets were created using different random seeds, and fit to separately. The fit results were then averaged for these 10 data sets.

The estimate of the error due to randomization of the start time of spills, was made from the spread of the fitted values of ω_a for selections with different random seeds, and found to be less than 40 ppb.

The choice of the bin width by itself could influence the fit result by introducing a time shift, since the histogram bin content represents the integrated value of the distribution over the bin width, and not the value of the distribution at the center of the bin, used in the calculation of the fit χ^2 [35].

The error due to the choice of the bin width was investigated by fitting histograms with different binning, but containing the same selection of the experimental data. For this study, 10 histograms with bin widths between 148.8 and 149.7 ns (with a 0.1 ns step) were fit to the 13-parameter function given by Eqn. 5.20. Only one seed was used in randomizing the injection time. The systematic effect on R was found to be less than 0.08 ppm, for the fit start time of 32 μs.

As pointed out in Ref. [84], incautious binning may produce artificial, not physically existing, oscillations in the positron time spectrum. Such oscillations may cause a bias in the fitted value of ω_a. To minimize this effect, it was recommended to use the bin width of $\Delta t = T_c \cdot (\frac{2l+1}{4})$, where T_c is the cyclotron period, and l is an integer. For $l = 2$ ($\Delta t = 1.25 \cdot T_c$), the difference in the values of R with respect to the "traditional" binning ($\Delta t = T_c = 149.185$ ns, used for all other histograms in this analysis) was found to be less than 0.1 ppm for all start times, consistent with the result of the above-mentioned study for 10 different bin widths close to T_c.

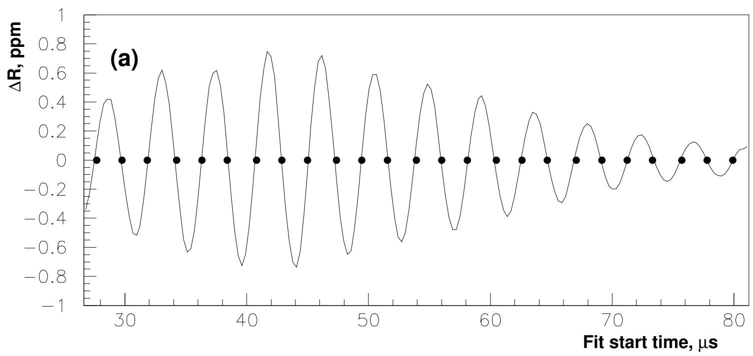

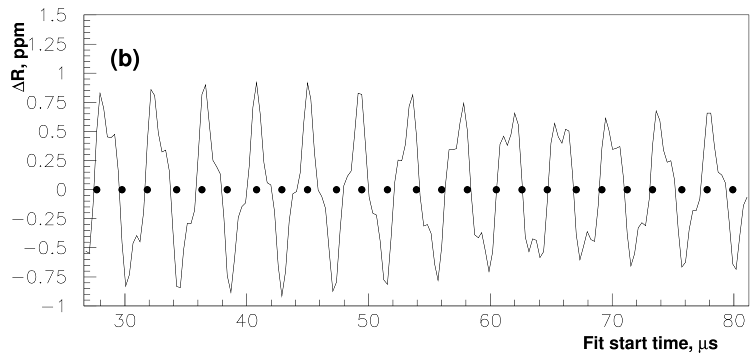

Figure 6.6: Phase pulling on the fit parameter R observed in the results of fit to data when (a) the correction for muon losses, or (b) the CBO correction are *not* included in the fitting function at all. Phase pulling due to muon losses is minimized for fits starting at the zero-crossings of the data, shown as filled circles.

6.5 Errors Due to Fitting Method and Strategy

The possible errors due to the uncertainties in the knowledge of the precise functional form of the decay spectrum, and due to peculiarities of the fit strategy, were also taken into account.

6.5.1 Fit Function Inefficiencies

As shown in Figure 6.6, not accounting for the CBO and muon loss terms in the fitting function results in a strong phase pulling on R. Only after these terms were included, did the fit χ^2 become reasonable (see Table 5.1), and the values of fit parameters become statistically independent of the fit start time.

Muon Losses

As was stated in Section 5.2.3, different forms of the fit function, exponential and gaussian, could be used to describe the muon losses. Both forms help reduce the χ^2, but do not remove the phase pulling on R completely (with the amplitude of the residual phase pulling under 50 ppb). The difference between the two results was used as a measure of the efficiency of fitting to the muon losses. The effect of the use of a non-ideal function to describe the muon losses was conservatively estimated at 0.1 ppm overall, and less than 0.01 ppm for fits starting at zero-crossings.

Even if the functional form described the data well, with an acceptable χ^2, an additional systematic error could arise since the lost muons might have different average spin direction compared to the stored muons. This error was estimated to be less than 0.1 ppm [85].

CBO

A similar comparison between the results obtained by using different forms of the CBO function gave an estimate of the error due to the inefficiency of fit to the CBO packet of the order of 40 ppb for the sum of the data from all detectors. The alternative functional forms of the CBO packet included using an exponential ($f_b(t) = e^{-t/\tau_B}$, rather than a gaussian $f_b(t) = e^{-[t/\tau_B]^2}$ as in Equation 5.16) function to describe the amplitude decay, and packets with the maximum at a time other than the injection time (i.e. $f_b(t) = e^{-[(t-t_0)/\tau_B]^2}$, with $t_0 \neq 0$).

The systematic effect from higher harmonics of betatron oscillations both in the vertical and in the horizontal directions was estimated in a simulation, and was found to be less than 0.03 ppm [74].

For the 1999 result, the total systematic effect of CBO was estimated at 0.05 ppm (average for 4 independent ω_a analyses)[5].

6.5.2 Fixing Fit Parameters

The value of the pile-up phase, parameters of the pile-up enhancement due to fast rotation, and some other parameters were fixed in the fit for various start times. The effects of fixing $\Delta\phi_p$ were discussed in Subsection 6.1.1.

To investigate the effect of fixing the values of the CBO decay time and frequency (τ_B and f_B) and the parameters describing the muon losses ($a_{\mu L}$ and $\tau_{\mu L}$), a comparison was done between the fitted values of R obtained using two different fit strategies:

[5] After the analysis was complete, an indication arose from preliminary studies of the data taken during the 2000 run, that the systematic effect from the presence of the modulation in the data with the "side-band" frequencies, $(\omega_B \pm \omega_a)$, should be taken into account as well. Additional systematic studies were conducted with a fit function including the side-band terms, which showed that the error due to CBO was probably underestimated by as much as a factor of 2. Since the uncertainty due to CBO is only one of a number of sources of systematic error in ω_a, the increase in the overall error would be insignificant.

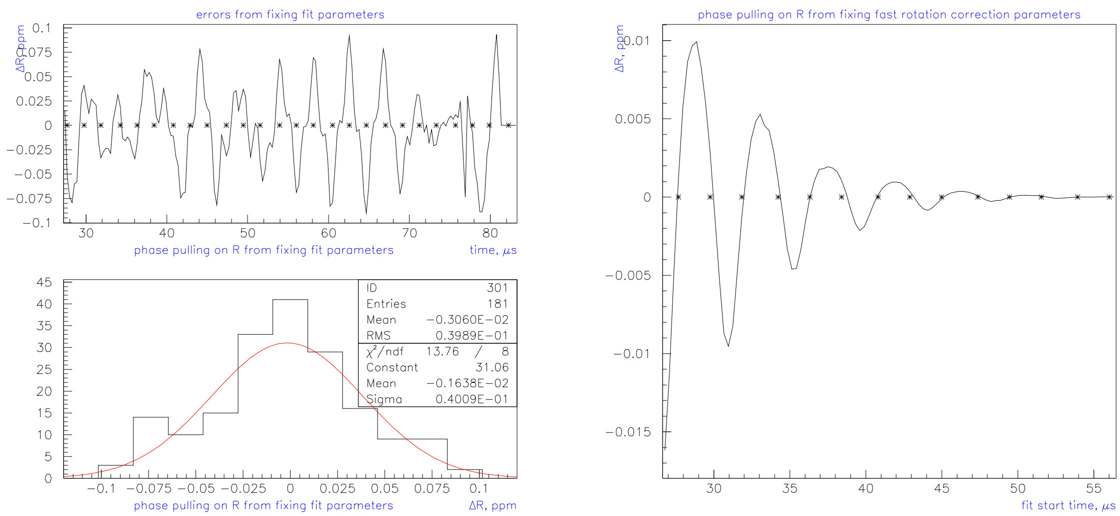

(a) (b)

Figure 6.7: Phase pulling on R: (a) due to fixing the parameters τ_B, f_B, $a_{\mu L}$ and $\tau_{\mu L}$ (top: ΔR vs fit start time, bottom: distribution of ΔR); and (b) due to fixing the parameters of the fast rotation correction to pile-up. Crosses denote the zero-crossings of the data.

one with the above mentioned 4 parameters fixed for all fit start times, and the other with these parameters free. The sensitivity of R to these parameters was found to be of the order of 40 ppb on the average[6] (see Figure 6.7(a)).

Changing the values of the parameters describing pile-up inflation due to fast-rotation resulted in a weak phase pulling with an amplitude of about 10 ppb (at 30 μs) for the values of a_p and τ_p increased or decreased by two standard deviations with respect to the central values estimated from the average energy studies (see Section 5.2.1). The value of R was almost unaffected for fits started at the zero-crossings of g-2 precession (see Figure 6.7(b)).

6.6 Other Errors

The timing shifts were studied using the laser calibration system, and were found to be less than 20 ps over the first 200 μs after the injection[7], which translated into 0.1 ppm uncertainty in the ω_a measurement.

[6]This error is only applicable to the results from fit with start time after 50 μs, when some of the fit parameters are fixed.

[7]Recent results from laser calibration studies suggest that such shifts are of the order of 3 ps over 200 μs [86].

Table 6.1: Systematic errors for the ω_a analysis [1].

Source of errors	Size (ppm)
Pile-Up	0.13
AGS background ("flashlets")	0.10
Lost muons	0.10
Timing shifts	0.10
E field and vertical betatron oscillation	0.08
Binning and fitting procedure	0.07
Coherent betatron oscillation	0.05
Beam debunching / randomization	0.04
Energy scale changes	0.02
Total systematic error on ω_a	0.3

Other sources considered included spin resonances, clock synchronization, stop time of the fit: each estimated as smaller than 0.01 ppm.

The leading sources of the systematic error on ω_a for the combined result of the 4 analyses (see Eqn. 5.30) are listed in Table 6.1.

6.7 Systematics of the ω_p Measurement

The total systematic error associated with the measurement of the magnetic field for the 1999 run was 0.4 ppm. The sources of this systematic error are listed in Table 6.2.

The uncertainty in the calibration of the NMR trolley probes (0.20 ppm) comes from the position uncertainties of the trolley probes with respect to the standard probe at the calibration point, and from the B-field inhomogeneity [80].

As illustrated in Figure 5.24, the magnetic field varies by about 500 ppm over the inflector region due to non-ideal fringe field shielding, and the NMR probes fail to work in the high magnetic field gradient associated with this variation: this results in a 0.2 ppm uncertainty in the measurement of $\langle\omega_p\rangle$, since the field is averaged over azimuth.

Tracking the field with fixed NMR probes is affected by the probe calibration limitations, as well as the daily temperature variations. This introduced an error of 0.15 ppm.

The azimuthally averaged magnetic field varies by about 7 ppm peak to peak across the storage region aperture (see Figure 5.25). Given this, the uncertainty in the calculated muon distribution results in a systematic error for the $\langle B\rangle$ measurement of 0.12 ppm.

Other errors were caused by the uncertainties in the trolley position inside the

Table 6.2: Systematic errors for the ω_p analysis [1].

Source of errors	Size (ppm)
Absolute calibration of standard probe	0.05
Calibration of trolley probe	0.20
Trolley measurement of B_0	0.10
Interpolation with fixed probes	0.15
Inflector fringe field	0.20
Uncertainty from muon distribution	0.12
Other	0.15
Total systematic error on ω_p	0.4

ring during the measurement, power supply instabilities, kicker eddy currents etc.

The errors of the ω_a and ω_p measurements for the 1999 run, added in quadratures produced the total systematic error on a_μ of 0.5 ppm. The statistical error was 1.25 ppm.

Chapter 7

Conclusions

Combining the results for ω_a and ω_p, given respectively by Eqns. 5.30 and 5.31, brings the new experimental value:

$$a_\mu(\mathrm{BNL}, 1999) = \frac{\omega_a/\omega_p}{\lambda - \omega_a/\omega_p} = 11\ 659\ 202(16) \times 10^{-10}\ (1.35\ \mathrm{ppm}), \tag{7.1}$$

where $\lambda = \mu_\mu/\mu_p = 3.183\ 345\ 39(10)$ [54] is the ratio of muon to proton magnetic moments.

As illustrated in Figure 7.1, the new result is in good agreement with previous measurements (with $\chi^2/\mathrm{DOF} = 2.8/4$). The difference between the new experimental average, $a_\mu^{exp} = 11\ 659\ 203(15)\ \times 10^{-10}$, and the theoretical prediction, given in Table 1.1, is

$$a_\mu^{exp} - a_\mu^{SM} = 43(16) \times 10^{-10}, \tag{7.2}$$

where the uncertainties are added in quadrature. The 2.6$\cdot\sigma$ discrepancy in Eqn. 7.2, which may suggest the presence of physics beyond the Standard Model, has stimulated great interest in the particle theory community[1].

A recent report by Knecht *et al.* [20] and a recalculation by Hayakawa and Kinoshita [21] indicated that the sign of the contribution to a_μ from hadronic light-on-light scattering (given by Equation 1.18) might be positive rather than negative, in which case the discrepancy between the theory and the experiment would shrink to about 1.5$\cdot\sigma$.

The techniques and methods developed for the studies of the 1999 data set will prove extremely valuable in the further analyses of the $(g-2)$ data. During our run in 2000, approximately 4.7 billion high-energy decay positrons ($E > 2$ GeV, after 32 μs) were collected, almost 5 times as many as before. The analysis of these data has begun. In addition to increased statistical power, the systematic errors on both $\langle B \rangle$ and ω_a measurements are expected to decrease. The magnetic field uniformity has improved significantly after a new inflector was installed. AGS background and muon

[1] A list of preprints may be obtained from the WWW:
`http://phyppro1.phy.bnl.gov/g2muon/new_theory.html` .

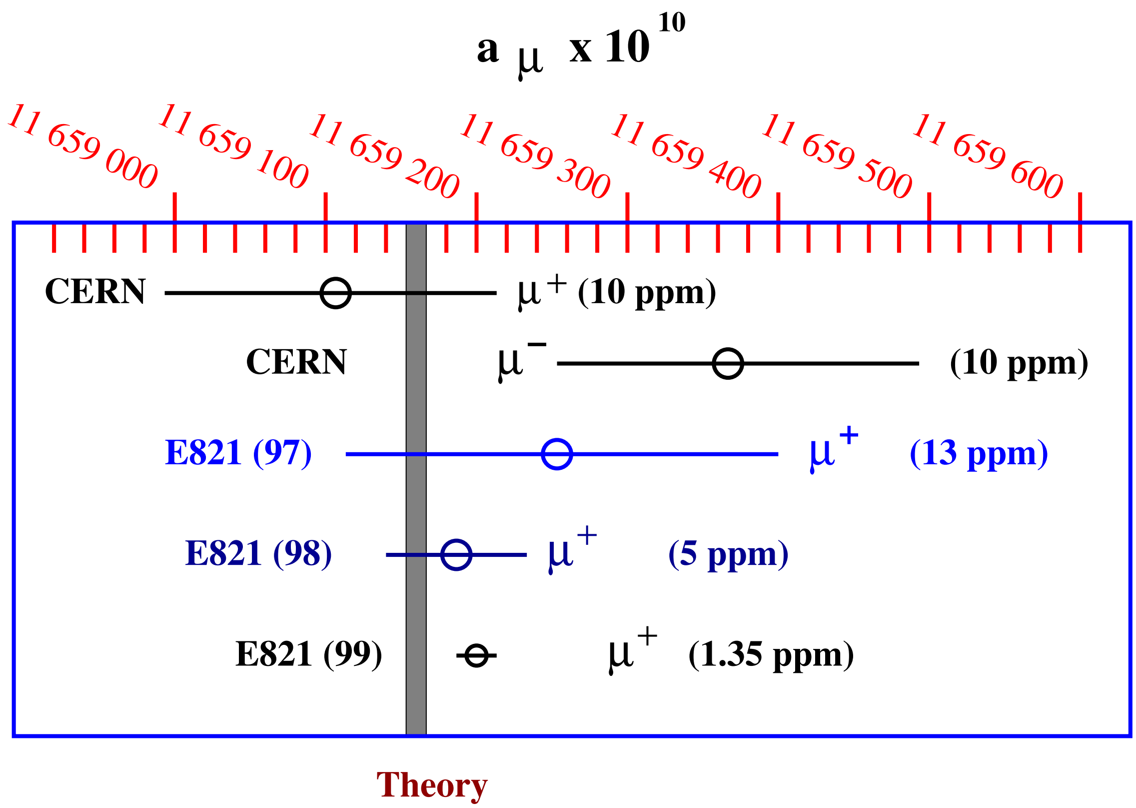

Figure 7.1: Five measurements of the muon anomalous magnetic moment shown in comparison with the one-standard-deviation region allowed by the standard theory (shaded area).

losses were substantially lower than in 1999 due to improvements made in the beam line and storage technique respectively.

In February-April 2001 we collected data with negative muons. The data from this run will bring the statistical error on a_{μ^-} to the level comparable to that reached for a_{μ^+}. Measuring the magnetic anomaly for both the positive and the negative muon will provide a sensitive test of CPT-invariance.

At the same time we expect a reduction in the uncertainty in the theoretical prediction for a_μ, after new experimental results are included in the calculation of the hadronic contribution.

The future results from the BNL $(g-2)$ experiment will be of even more interest and importance than the one described in this dissertation, and may prove crucial in the quest for understanding of the fundamental particle interactions.

List of Abbreviations

Comp. Jour. ... Computer Journal
Int. Conf. ... International Conference
Eur. Phys. J. ... European Physical Journal
Nucl. Phys. ... Nuclear Physics
Nucl. Instrum. Meth. ... Nuclear Instruments and Methods in Physics Research
Part. Accel. Conf. ... Particle Accelerator Conference
Phys. Lett. ... Physics Letters
Phys. Rep. ... Physics Reports
Phys. Rev. ... Physical Review
Phys. Rev. Lett. ... Physical Review Letters
Proc. Suppl. ... Proceeding Supplements
Rev. Mod. Phys. ... Reviews of Modern Physics
Rep. Prog. Phys. ... Report on Progress in Physics
Univ. ... University

Bibliography

[1] H.N. Brown *et al. Phys. Rev. Lett.*, **86**:2227, 2001.

[2] J.E Nafe, E.B. Nelson and I.I. Rabi. *Phys. Rev.*, **71**:914, 1947.

[3] D.E. Nagl *et al. Phys. Rev.*, **72**:971, 1947.

[4] P. Kusch and F.M. Foley. *Phys. Rev.*, **72**:1256, 1947. *Phys. Rev.*, **74**:250, 1948.

[5] J.S. Schwinger. *Phys. Rev.*, **73**:416, 1948 and *Phys. Rev.*, **75**:898, 1949.

[6] P.J. Mohr and B.N. Taylor. *Rev. Mod. Phys.*, **72**:351, 2000.

[7] T. Kinoshita and W.J. Marciano in *Quantum Electrodynamics,* edited by T. Kinoshita. World Scientific, Singapore, 1990, p.419.

[8] V.W. Hughes and T. Kinoshita. *Rev. Mod. Phys.*, **71**:S133, 1999.

[9] A. Czarnecki and W.J. Marciano. *Nucl. Phys. (Proc. Suppl.)*, **B 76**:245, 1999.

[10] T. Kinoshita. *Rep. Prog. Phys.*, **59**:1459, 1996.

[11] R.S Van Dyck Jr., P.B Schwinberg, and H.G. Dehmelt. *Phys. Rev. Lett.*, **59**:26, 1987.

[12] J. Bailey *et al. Nucl. Phys.*, **B 150**:1, 1979.

[13] R. Alemany *et al. Eur. Phys. J.*, **C 2**:123, 1998.

[14] D. Commins and P. Bucksbaum. *Weak Interactions of Leptons and Quarks.* Cambridge Univ. Press, 1983, p. 168.

[15] M. Davier and A. Höcker. *Phys. Lett.*, **B 435**:427, 1998.

[16] M. Davier. *Nucl. Phys. (Proc. Suppl.)*, **B 76**:327, 1999.

[17] R.R. Akhmetshin *et al.* Preprint BINP 99-10, hep-ex/9904027 (1999).
R.R. Akhmetshin *et al.* *Phys. Lett.*, **B 475**:190, 2000.
S. Anderson *et al.* *Phys. Rev.*, **D 61**:112002, 2000.
J.Z. Bai *et al.* *Phys. Rev. Lett.*, **84**:594, 2000.
Z.G. Zhao. *Int. J. Mod. Phys.*, **A 15**:3739, 2000.

[18] A. Czarnecki and W.J. Marciano. *Phys. Rev.*, **D 64**:013014, 2001.

[19] B. Krause. *Phys. Lett.*, **B 390**:392, 1997.

[20] M. Knecht and A. Nyffeler. Preprint hep-ph/0111058 (2001).
M. Knecht *et al.* Preprint hep-ph/0111059 (2001).

[21] M. Hayakawa and T. Kinoshita. Preprint hep-ph/0112102 (2001).

[22] A. Czarnecki, B. Krause and W.J. Marciano. *Phys. Rev. Lett.*, **76**:3267, 1996.

[23] W.B. Marciano in *Particle Theory and Phenomenology,* edited by K. Lassila *et al.* World Scientific, Singapore, 1996, p. 22.

[24] H.A. Bethe. *Phys. Rev.*, **72**:339, 1947.
G. Breit. *Phys. Rev.*, **72**:984, 1947.

[25] W.E. Lamb and R.C. Retherford. *Phys. Rev.*, **72**:241, 1947.

[26] N.H. Louisell, R.W. Pidd and H.R. Crane. *Phys. Rev.*, **94**:7, 1954.

[27] A. Rich, J.C. Wesley. *Rev. Mod. Phys.*, **44**:250, 1972

[28] R.L. Garvin, L.M. Lederman and M. Weinrich. *Phys. Rev.*, **105**:1415, 1957.

[29] G. Charpak *et al.* *Nuovo Cimento*, **37**:1241, 1965.

[30] J. Bailey *et al.* *Phys. Lett.*, **B 28**:287, 1968.

[31] J. Bailey *et al.* *Nuovo Cimento*, **A 9**:369, 1972.

[32] M. Gourdin and E. de Rafael. *Nucl. Phys.*, **B 10**:667, 1969

[33] M. Tanaka and Y.Y. Lee. IEEE Part. Accel. Conf., 1993.
W.W. MacKay *et al.* 5th European Part. Accel. Conf., 1996.
M. Blaskiewicz *et al.* IEEE Part. Accel. Conf., 1996.

[34] S.P. Redin. *A New Precision Measurement of the Muon (g-2) Value.* Ph.D. dissertation. Yale University, 1999.

[35] J.M. Kindem. *The Anomalous Magnetic Moment of the Positive Muon.* Ph.D. dissertation. Univ. of Minnesota, 1998.

[36] W. Morse, private communication.

[37] F. Krienen *et al.* *Nucl. Instrum. Meth.*, **A 283**:5, 1989.
A. Yamamoto *et al.* Proceedings of the 15th Int. Conf. on Magnet Technology, Science Press Beijing, 246 (1998).

[38] G.D. Danby *et al.* *Nucl. Instrum. Meth.*, **A 457**:151, 2001.

[39] R. Prigl *et al.* *Nucl. Instrum. Meth.*, **A 374**:118, 1996.

[40] X. Fei *et al.* *Nucl. Instrum. Meth.*, **A 394**:3499, 1997.

[41] F. Combley and E. Picasso. *Phys. Rep.*, **C 14**:1, 1974.

[42] V.W. Hughes. *The Muon Anomalous Magnetic Moment.* $(g-2)$ internal note 372, 2000, unpublished.

[43] S. Sedykh *et al.* *Nucl. Instrum. Meth.*, **A 455**:346, 2000.

[44] J. Ouyang *et al.* *Nucl. Instrum. Meth.*, **A 374**:215, 1996.

[45] P. Cushman *et al.* *Nucl. Instrum. Meth.*, **A 378**:116, 1996.

[46] R. Carey. *How Does the WFD Work?* $(g-2)$ internal note 301, 1998, unpublished.

[47] I. Kronkvist *et al.* , *UNIX-based Data Acquisition System for* $(g-2)_\mu$. $(g-2)$ internal write-up, 1999, unpublished.

[48] I. Logashenko. *FIT Pulse Finding Algorithm.* $(g-2)$ internal note 334, 1999, unpublished.

[49] I. Logashenko. *Shapes of WFD Pulses and the FIT Pulse Finding Algorithm.* $(g-2)$ internal note 369, 2000, unpublished.

[50] I. Logashenko. *G2OFF-based Production of 1999 Data.* $(g-2)$ internal note 378, 2000, unpublished.

[51] *Physics Analysis Workstation (PAW).* CERN Program Library Long Writeup Q121. CERN, Geneva, Switzerland, 1993.

[52] S.M. Fisher and P. Palazzi. *ADAMO: Entity-Relationship Programming System.* CERN, Geneva, Switzerland, 1994.

[53] R.M. Carey *et al.* *Phys. Rev. Lett.*, **82**:1632, 1999.

[54] W. Liu *et al.* *Phys. Rev. Lett.*, **82**:711, 1999. W. Liu *et al.* *Phys. Rev. Lett.*, **82**:711, 1999.

[55] H.N. Brown *et al. Phys. Rev.*, **D 62**:091101, 2000.

[56] C. Özben. *1998 ω_a Analysis of* $(g-2)$. $(g-2)$ internal note 347, 1999, unpublished.

[57] R. Carey and J. Miller. *The Impact of Gain and Frequency Shifts on the g-2 Frequency Measurement.* $(g-2)$ internal note 165, 1993, unpublished.

[58] G. Marsaglia, A. Zaman and W.-W Tsang. *Stat. Prob. Lett*, **9**:35, 1990.

[59] G. Onderwater and J. Pretz. *Pile-up.* $(g-2)$ internal note 363, 2000, unpublished.

[60] A. Trofimov. *ω_a Analysis of the 1999 Data.* $(g-2)$ internal note 388, 2001, unpublished.

[61] R. Carey and J. Miller. *The Effect of the Fast Rotation Structure on the Level of Pile-up.* $(g-2)$ internal note 344, 1999, unpublished.

[62] C.S. Özben and Y.K. Semertzidis. *Eliminating Pileup from the g-2 Data.* $(g-2)$ internal note 365, 2000, unpublished.

[63] J. Pretz. *Reducing the Statistical Error on the g-2 Frequency Using a Weighting Procedure.* $(g-2)$ internal note 326, 1998, unpublished.

[64] W.H. Press *et al. Numerical recipes in C.* Cambridge Univ. Press, 1992, p.504.

[65] Y.F. Orlov. *About the Influence of Coherent Radial Oscillations.* $(g-2)$ internal note 359, 2000, unpublished.
Y.F. Orlov. *Perturbation of the Observed (g-2) Signal by Coherent Betatron Oscillation.* $(g-2)$ internal note 341, 1999, unpublished.

[66] R. Carey. *Monitoring Muon Losses in the 1999 and 2000 Data with 3-fold Coincidences.* $(g-2)$ internal note 382, 2000, unpublished.

[67] *MINUIT: Function Minimization and Error Analysis.* CERN Program Library Long Writeup D506, CERN Geneva, Switzerland, 1994.

[68] W.C Davidon. *Variable metric method for minimization.* Argonne National Laboratory, ANL-5990 Rev., University of Chicago, 1959.
R. Fletcher and M.J.D. Powell. *Comp. Jour.*, **6**:163, 1963.

[69] J. Pretz. *Summary of the 1998 ω_a Analysis.* $(g-2)$ internal note 353, 1999, unpublished.

[70] D. Kawall. *Statistical and Systematic Errors in Fitting ω_a.* $(g-2)$ internal note 322, 1998, unpublished.

[71] S. Redin *Statistical Equations for Set-subset Problem.* $(g-2)$ internal note 387, 2001, unpublished.

[72] L. Duong. *A Precise Measurement of the Anomalous Magnetic Moment of the Muon.* Ph.D. dissertation. Univ. of Minnesota, 2001.

[73] G. Onderwater. Preprint hep-ex/0105036 (2001).

[74] C. Özben. *1999 ω_a Analysis of g-2.* $(g-2)$ internal note 385, 2001, unpublished.

[75] G. Onderwater. *Analysis of the 1999 Muon Spin Precession Data.* $(g-2)$ internal note 390, 2001, unpublished.

[76] F. Farley and E. Picasso in *Quantum Electrodynamics,* edited by T. Kinoshita. World Scientific, Singapore, 1990, p.493.

[77] E821 Collaboration. *BNL AGS E821 Design Report.* BNL, 1995, pp. 55-57.

[78] F. Farley. *Electric Field and Pitch Corrections for 99 Runs.* $(g-2)$ internal note 370, 2000, unpublished.

[79] O. Rind and E. Sichtermann. *On Combining the Results for ω_a.* $(g-2)$ internal note 380, 2001, unpublished.

[80] G. Danby *et al. Analysis of the Magnetic Field for 1999.* $(g-2)$ internal note 368, 2000, unpublished.

[81] W. Morse. *The Low Pulse Height Pile-Down Effect.* $(g-2)$ internal note 373, 2000, unpublished.

[82] S. Redin. *AGS Flashlet Background.* $(g-2)$ internal note 342, 1999, unpublished.

[83] V. Druzhinin and G. Fedotovich. *Study of the AGS Flashlet Background for 2000 run.* $(g-2)$ internal note 375, 2000, unpublished.

[84] Y.F. Orlov. *Some Rules for Binning.* $(g-2)$ internal note 336, 1999, unpublished.

[85] W. Morse. *Lost Muon Systematic Error in the 99 Run.* $(g-2)$ internal note 371, 2000, unpublished.

[86] R. Carey, private communication.